Ollscoil na hÉireann - The National University of Ireland

A study of Internal Transport Barriers in the ASDEX Upgrade tokamak

Éilis D. Quigley

Roinn na Fisice
Coláiste na hOllscoile, Corcaigh

Department of Physics
University College Cork

Supervisor: Dr. Patrick J. Mc Carthy

Thesis submitted for the Degree of Doctor of Philosophy to the
National University of Ireland

~ 2006 ~

Abstract

One of the most challenging problems facing the fusion research community today is improving the confinement of energy and fuel within the magnetically confined plasma. The confinement of the plasma is degraded by anomalous transport which is thought to be caused by instabilities in the plasma. Under certain conditions a plasma can develop a region of reduced transport, and hence high confinement, in the plasma core. This region is known as an internal transport barrier (ITB). In recent years ITBs have become a subject of great interest among fusion researchers. This is due to their potential, firstly for providing a solution for plasma confinement and secondly, for improving the theoretical understanding of plasma turbulence and transport.

In this thesis an extensive study of the ITBs in the ASDEX Upgrade tokamak is presented. The behavior of ITB plasmas is examined both experimentally and analytically, so that all clues as to the underlying theory can be appreciated. A description of the ion temperature gradient (ITG) instability is given. The behavior of the ITB is examined and this is compared with the evolution of the safety factor (q) profile. The q profile is recovered using the CLISTE equilibrium code.

The effect of possible turbulence suppression mechanisms on ITB formation and sustainment is examined experimentally. These include the density gradient, the $E \times B$ flow shear and the Shafranov shift. These effects are also studied analytically using the gyro-kinetic linear stability code, GS2, along with the effect of various plasma shaping parameters. The dependency of the ITG growth rate on these parameters is examined.

Also in this thesis ITB discharges are examined using the GLF23 model in the ASTRA transport simulation code. The ability of the model to predict ITB behavior is investigated as are the mechanisms which lead to ITB formation and sustainment.

Acknowledgments

This work was supervised by Drs.P.J.McCarthy and A.G.Peeters and I would like to acknowledge their support, guidance, patience and hard work which made this thesis possible. For this I am eternally grateful to them both. This research was carried out as part of the Plasma Physics Group at UCC and also as part of the plasma Transport Theory Group at the Max-Planck-Institut für Plasmaphysik (IPP), Garching, Germany. It was supported by a research agreement between IPP and UCC, and by EURATOM.

I would like to give my particular thanks to the many colleagues that helped me over the years. To Drs.J.Hobirk and D.Merkel for their guidance with the MSE diagnostic data and its inclusion in the CLISTE calculations. A special thanks to Dr.G.Tardini for always being available to help me with the ASTRA code. I would also like to extend thanks to Dr.M.Apostoliceanu for the initial calculations using the GS2 code. For his help in the method for calculation the toroidal velocity of the main deuterium ions, I am indebted to Dr.D.Nishijima. Thanks also to Dr.G.Pereverzev and Mr.P.Martin for administering the ASTRA and CLISTE codes, respectively. I would also like to thank the members of the ASDEX Upgrade team who made the experimental runs possible and all those responsible for the development and maintenance of the various codes used for the purposes of this work. To the friends I have made at IPP and UCC over the years, thanks for all the support, friendship and all the fun times.

To my family, my mother, Nina, my father, Jim, and my sisters, Sarah and Emira, all the encouragement and love you gave me made me into the woman I have become. To my little nephew, Cillian, for all the laughs. Last but definitely not least, to Jonathan, for being there for me and believing in me all these years and especially recently. I promise to be just as supportive of you in, hopefully, the not too distant future. My love and thanks to you all.

Contents

Chapter 1

Introduction

1.1 Why nuclear fusion?

Currently, most of the worlds electricity demand is satisfied by fossil fuels, that is by oil, natural gas and coal. Burning these fuels causes CO_2 to be emitted and contributes to the greenhouse effect.[1, 2] Also, at the present levels of consumption, conventional oil and gas resources will last for a couple more generations at most. However, demand is set to rise as the worlds population grows and access to electricity in developing countries increases.[3] This means that other energy sources will be needed very soon to fill the gap when fossil fuel resources have been exhausted. Many possibilities are being investigated, these include, renewable energy technologies, nuclear fission and nuclear fusion. It is envisaged that the energy demands will be filled by a mixture of these different sources.

The renewable energy technologies, namely solar, tidal, wave, wind, biomass, geothermal and hydro have been greatly researched in recent years. Many are already fully developed and contribute substantially to energy production. However, they depend on geographical positioning, are variable in nature and can be effected by sudden local climatic changes.[4] Hence, although they are a very desirable energy source, it is likely that another energy source which can fill the gaps will be needed to complement

renewable energy sources. The main candidate which can meet this demand and is available for the longterm is nuclear power.

Nuclear fission energy production has already been in use for many years and the problems involved have been well publicized. This has contributed to a general public concern about nuclear technologies, which unfortunately seems to sometimes include nuclear fusion.

The fission process produces dangerous by-products and hazardous waste. A large amount of the waste is radioactive and is difficult to dispose of without contaminating the environment. One of the by-products is plutonium, which is produced in some reactors, this can be used in the production of nuclear arms. Also, there is the risk of a reactor going into meltdown, such as what happened with Chernobyl, or a terrorist attack. Both of which could cause an immediate loss of many lives and also widespread, longterm environmental damage. These problems are quite disconcerting, nevertheless, unless another possible primary energy source becomes available, it is likely that nuclear fission will emerge as the next primary energy source.

Nuclear fusion could be the alternative, since it is a potentially unlimited energy source. It also lacks most of the safety concerns and hazardous waste associated with fission. Unlike with fission, no primary radioactive waste is produced. However, there is a small amount of contamination of the vacuum vessel which would have to be disposed of. Although with proper choice of material this can be minimized as much as possible, the lifetime of the contamination is in any case relatively short lived. Due to the very low densities of reactants involved in nuclear fusion, the triggering of a chain reaction that could lead to meltdown is impossible. The following sections discuss the nuclear fusion process and the plasma physics involved and are based on [5, 6, 7].

1.2 Nuclear Fusion: the basics

The energy from nuclear fission is produced by splitting heavy nuclei, such as uranium. In 1929, Robert Atkinson and Friedrich Houtermans first proposed that energy could also be produced by fusing two light nuclei to form a heavier nuclei where the rest mass of the reactants exceeds that of the reaction products. They hypothesized that this could be the process powering the stars. The process yields an energy, E, which is predicted by Einsteins relation, $E = \Delta mc^2$, where Δm is the mass difference and c is the speed of light in vacuo.

There are numerous possible fusion reactions involving different reactants, a list of the most promising from the point of view of a potential energy source, are:

$$ {}^2_1D + {}^3_1T \longrightarrow {}^4_2He + {}^1_0n + 17.6MeV \tag{1.1a} $$

$$ {}^2_1D + {}^2_1D \longrightarrow {}^4_2He + 23.0MeV \tag{1.1b} $$

$$ {}^2_1D + {}^2_1D \longrightarrow {}^3_2He + {}^1_0n + 3.25MeV \tag{1.1c} $$

$$ {}^2_1D + {}^2_1D \longrightarrow {}^3_1T + {}^1_1H + 4MeV \tag{1.1d} $$

The most accessible exothermic nuclear fusion reaction involves the hydrogen isotopes deuterium and tritium, given in equation (1.1a), where the net kinetic energy carried off by the reaction products (17.6 MeV) corresponds to a loss in rest mass of 0.188 proton masses. This means that one kg of this fuel would generate $10^8 kWh$ of energy, which would provide the requirements of a $1GW$ (electrical) power station for a day.

In order to produce the fusion of the nuclei of deuterium and tritium the mutual electrostatic repulsion due to their positive charge must firstly be overcome, because of this the cross-section for fusion is small at low energies. Luckily, the cross-section is energy dependent and it reaches a maximum at 100 KeV, see figure 1.1. Thus, it is necessary to increase the average kinetic energy of the reacting nuclei and because the required reactions occur in the high energy tail of the Maxwellian distribution of heated

particles, a temperature of 10 KeV is sufficient. At such temperatures the fuel has become an electrically neutral fully ionized plasma. This method of producing fusion is called thermonuclear fusion.

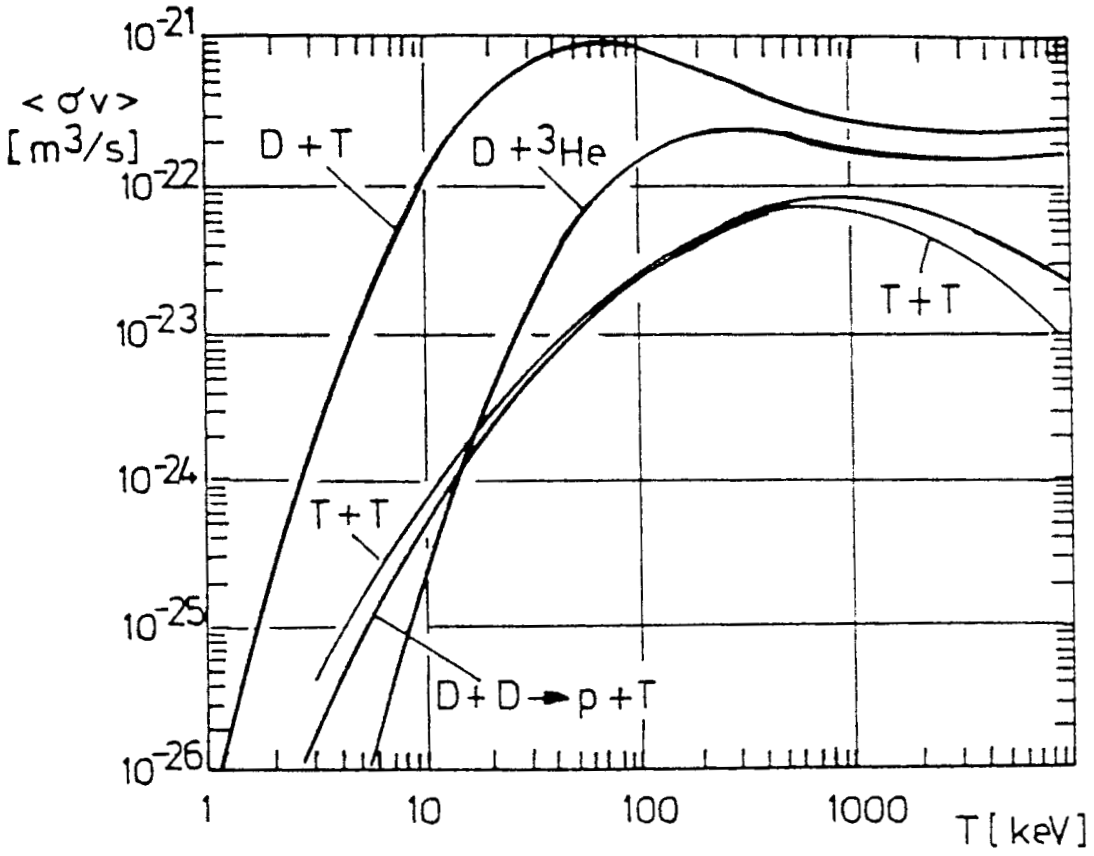

Figure 1.1: Fusion cross-section for D-T, D-D, D-He and T-T reactions versus temperature (KeV).

1.3 Plasma confinement by magnetic fields

Good confinement of energy is necessary so that the high temperatures required for sustained thermonuclear fusion reactions are achieved. In magnetic confinement devices a strong magnetic field is used for this purpose. The Lorentz force connected with the

magnetic field prevents the particles from moving over large distances perpendicular to the magnetic field. Instead the particles gyrate around the field lines with a gyro-radius given by $r_g = mv_\perp/qB$ where m is the particle mass, $v_\perp$ is the speed perpendicular to the field line, q is the particle charge and B is the magnetic field magnitude. For typical parameters the gyro-radius is several millimeters in length for the ions and even smaller for the electrons. Since the devices have a diameter of several meters, good confinement perpendicular to the magnetic field is obtained in this way. Of course the Lorentz forces does not prevent the particles from moving along the magnetic field. Hence, to prevent a rapid loss of energy through this motion the magnetic field is shaped in the form of a donut with the magnetic field lines going around in the toroidal direction without ever touching the material wall. The magnetic field is produced by currents in coils linking the plasma which has a $1/R$ dependence, R is the major radius and is measured from the axis of symmetry. Due to this dependence the gyrating particles have unequal gyroradii in opposite halves of their orbits. This causes electrons and ions to drift to the top and bottom of the torus, respectively, setting up an electrostatic field. Due to this field, E, the particles begin to drift outwards in the $E \times B$ direction. These drifts are called the ∇B and the $E \times B$ drifts respectively, they are described in more detail in section 1.4.3.

The $E \times B$ drift is very damaging for the plasma confinement, however, it is minimized by an induced poloidal magnetic field. The combination of the poloidal and toroidal magnetic fields mean that the field lines are twisted so that they follow helical paths around the torus, see figure 1.2. A line of force at A with the coordinates (ρ, θ) starting in the right-hand cross-section of figure 1.2 arrives at the left-hand side at the point A'. The angle θ around the minor axis has been changed by an amount $\Delta\theta$. The average poloidal angular displacement, $\bar{\Delta}\theta$, per toroidal turn of the field line is called the rotational transform, ι. The helicity of the field lines is very important for the stability of the plasma and is measured by the safety factor or q-factor which is given by

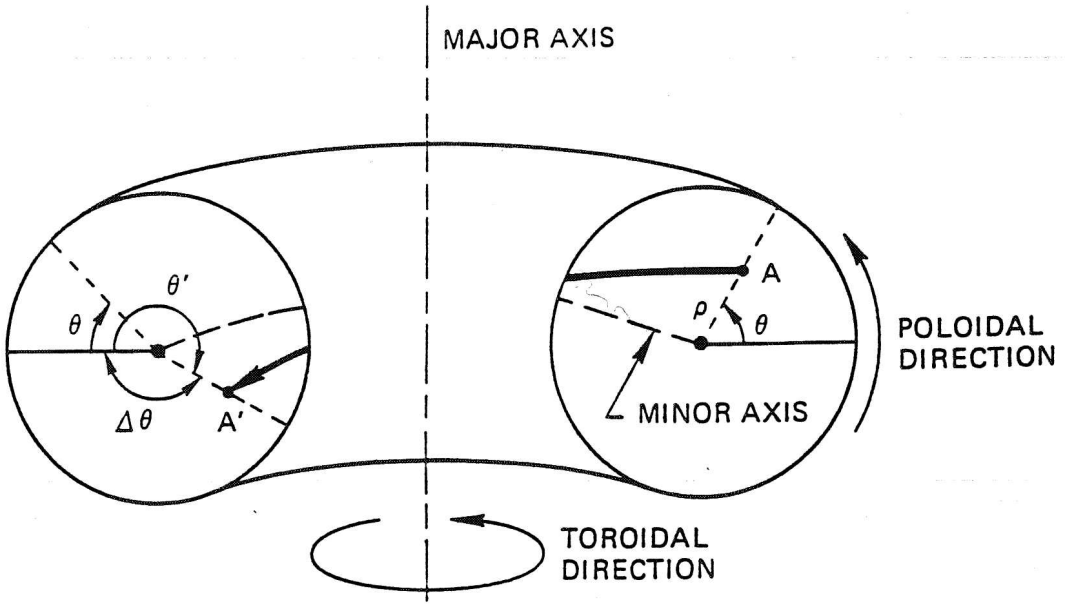

Figure 1.2: The toroidal field with rotational transform. A line of force A-A' changes its azimuthal angle θ around the minor axis as it winds around the major axis.

$$q(r) = \frac{1}{\iota} = \frac{2\pi}{\Delta\theta}. \tag{1.2}$$

The q-factor can also be defined as the number of toroidal windings, m, of the field lines divided by the number of poloidal windings, n,

$$q(r) = \frac{m}{n}. \tag{1.3}$$

The complete magnetic field produces an infinite set of nested toroidal magnetic surfaces. The direction of the magnetic field changes from surface to surface. This shear of the magnetic field is called the magnetic shear, $\hat{s}$, and it is related to the q-factor. A simplified

but very useful approximation can be given for the case of a large aspect ratio tokamak with a circular cross-section

$$\hat{s} = \frac{r}{q}\frac{dq}{dr}, \tag{1.4}$$

where r is the minor radius of the plasma.

Currently, there are two types of magnetic confinement fusion devices being investigated: the Stellarator and the Tokamak. In the former device the magnetic field is completely determined by the field coils outside the plasma, eliminating the current and hence a source of free energy in the plasma. The Stellarator does not have some of the more dangerous instabilities which occur in Tokamaks and is intrinsically steady state. The device is, however, much more complicated to build. Currently, the Tokamak concept is the most developed one. It was realized for the first time by L. Artsimovich in 1952. The name comes from the Russian acronym TOroidalnaya KAmera MAgnitnymi Katushkami, which means "toroidal chamber with magnetic coils". In this device the toroidal field component is the dominant one and the poloidal component is created mainly by a transformer induced toroidal current in the plasma, with a varying contribution from the non inductive current drive. The next step fusion device is to be an experimental tokamak reactor, called the International Thermonuclear Experimental Reactor or ITER. Due to the substantial cost of building such a prototype reactor it will be built as part of an international collaboration with the cost divided between the countries involved. Work is due to begin shortly at the proposed site in Cadarache, France, and will take approximately 10 years to complete, see figure 1.3 for an illustration of this device.

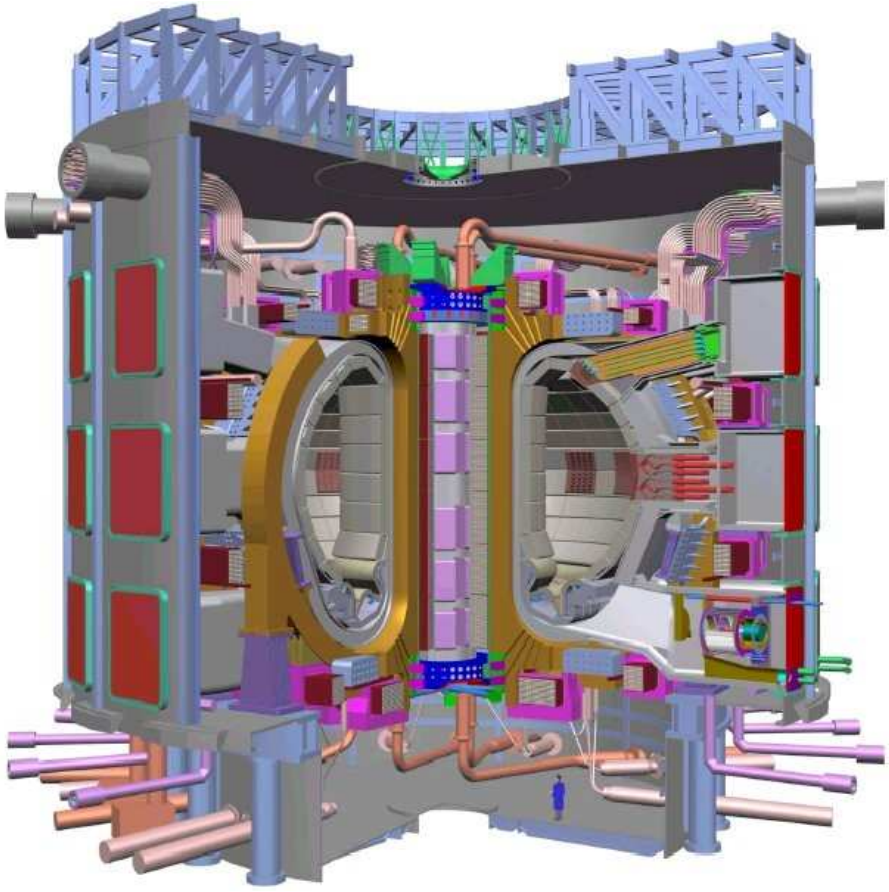

Figure 1.3: A cut away model of the planned ITER tokamak.

1.4 Transport in tokamaks

A fusion device is said to have reached ignition when the heating power from the thermonuclear reactions exceeds that of the thermal energy losses. These losses are due to the radiative loss through bremsstrahlung and diffusive energy loss, through heat conduction and particle convection. In order for the output power to be sufficiently large, the charged α-particles need to be magnetically confined for at least as long as it takes them to deposit their kinetic energy by thermalizing with the bulk plasma. When the plasma has ignited the external heating, used initially to raise the temperature to the level where fusion can occur, can be switched off.

The rate of energy loss, P_L, is characterized by an energy confinement time, τ_E, defined by the relation

$$P_L = \frac{W}{\tau_E} \tag{1.5}$$

where $W = 3n\bar{T}V$ is the total energy in the plasma, n is the density, T is the temperature, V is the volume and the bar represents the average value. Thus, the confinement plays a very important role in nuclear fusion. It will essentially determine the size and therefore the cost of the device. It is therefore important to understand its basic mechanisms.

1.4.1 Particle orbits

As mentioned before the particles in a uniform magnetic field gyrate around the magnetic field direction with a fixed radius, this is called the Larmor radius and is given by

$$\rho_j = \sqrt{2}\frac{m_j v_{T_j}}{|e_j|B} \tag{1.6}$$

where m_j and e_j are the particle, of species j, mass and charge respectively, B is the magnetic field and this is for a particle with mean thermal energy in the plane perpendicular to the magnetic field, such that $v_{T_j} = \frac{1}{\sqrt{2}}v_\perp$. Due to the larger mass of an ion, the Larmor radius of the ions is larger than that of the electrons.

1.4.2 Particle motion along B

In a homogeneous magnetic field the particle motion along the field lines is force free. However, in a tokamak the magnetic field is inhomogeneous and this causes an acceleration of the particles along the magnetic field. If the magnetic field strength has a gradient parallel to **B**, because the particle has a velocity perpendicular to **B**, there is a

force on the particle parallel to the magnetic field at the center of its gyro-orbit. This force is in the direction of weaker magnetic field. Thus, if the particle is traveling from a region of low **B** to a region of high **B** the force on the particle will cause it to slow down. If the magnetic field reaches a critical value, B_{ref}, the particles are reflected by this force. This effect is called the mirror effect and can lead to particles being trapped in the region of low magnetic field, (which is on the outer section of the torus). Due to particle drifts, discussed in the next paragraph, they take a characteristic banana orbit. The banana orbit is thus called because the orbit has the shape of a banana in the poloidal projection plane. A component of the electric field parallel to **B** also causes the particles to accelerate.

1.4.3 Particle drifts

There are four different types of guiding center drifts, each due to a different electromagnetic effect. As shown in section 1.6 these drifts can cause microinstabilities which lead to a serious degradation in confinement. The drifts are the $E \times B$ drift, the ∇B drift, curvature drifts and the polarization drift, each of these is described below.

1. The $E \times B$ drift

If there is an electric field component perpendicular to the magnetic field the particles drift perpendicular to the magnetic field, see figure 1.4. This is called the $E \times B$ drift, and the drift velocity is given by

$$v_d = \frac{E \times B}{B^2} \tag{1.7}$$

Note that the ions and electrons drift in the same direction and also have the same magnitude.

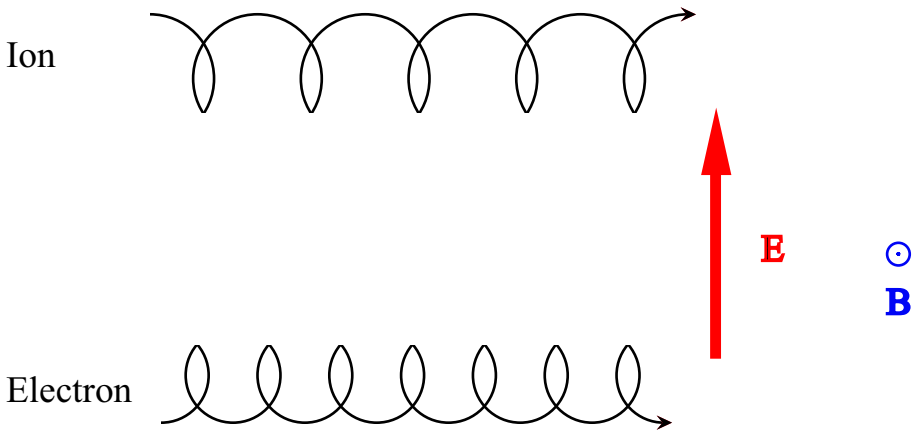

Figure 1.4: $\mathbf{E} \times \mathbf{B}$ *drift of the ions and electrons.*

2. The ∇B drift

In the presence of magnetic field strength gradient transverse to $\mathbf{B}$, a particle drift perpendicular to both $\mathbf{B}$ and ∇B will result. If for example the situation where ∇B is perpendicular to $\mathbf{B}$ is taken, one can see that the particle will experience different magnetic fields on its gyration orbit. Hence, the Larmor radius will be smaller in the region of higher B and larger where the field is smaller (as equation (1.6) predicts). Thus, the gyro-orbit is not exactly closed, the guiding center is displaced perpendicular to both $\mathbf{B}$ and ∇B. Figure 1.5 shows this drift schematically, note that the electrons and ions drift in opposite directions because the gyration motion around $\mathbf{B}$ is anticlockwise for ions and clockwise for electrons. In this case the drift velocity is given by:

$$v_d = \frac{1}{2}\rho_j \frac{\mathbf{B} \times \nabla B}{B^2} v_\perp \tag{1.8}$$

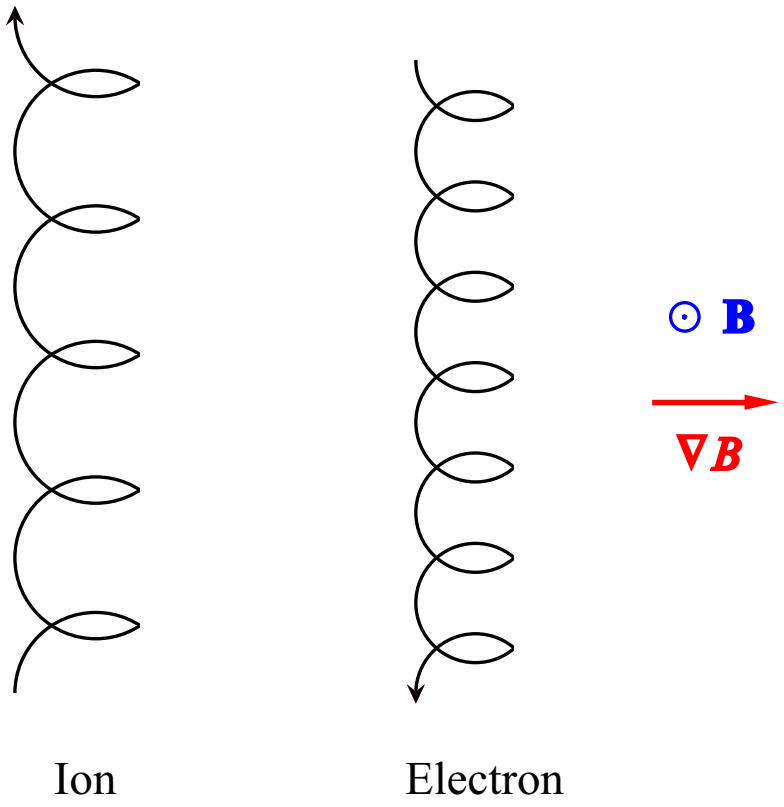

Figure 1.5: The gradient of B perpendicular to **B** *gives ion and electron drifts in opposite directions.*

3. The curvature drift

In a tokamak, and other toroidal fusion devices, the magnetic field lines are curved. This curvature also leads to a particle drift, due to the centrifugal force experienced by the particles. The curvature drift is given by

$$v_d = \frac{v_\parallel^2}{\omega_{c_j} R} \tag{1.9}$$

where $v_\parallel$ is the parallel velocity, $\omega_{c_j} = e_j B/m_j$ is the cyclotron frequency and R is the radius of curvature. Since ω_{c_j} takes the sign of the particle charge, the electrons and

ions have opposing drifts, the drift direction of the ions is that of $i_c \times \mathbf{B}$, where i_c is the unit vector outwards along the radius of curvature, see figure 1.6. Also, since the drift is proportional to the mass of the particle, the drift of the electrons is much smaller than that of the ions.

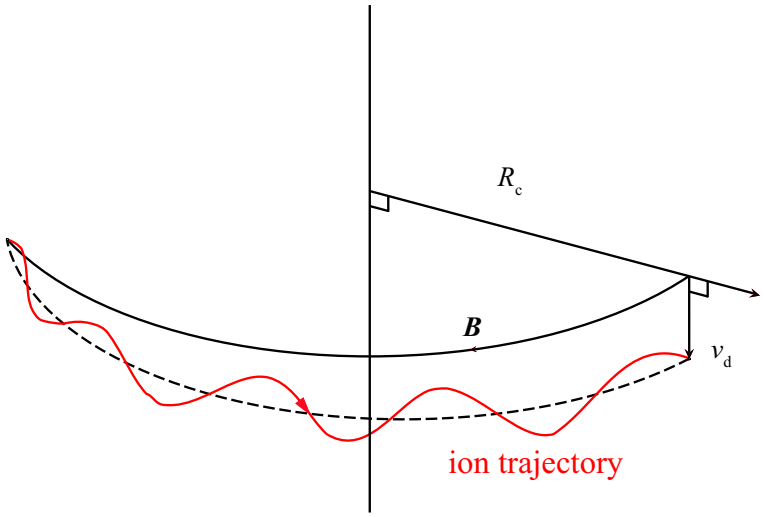

Figure 1.6: The ion drift due to the curvature of the magnetic field. The electrons drift in the opposite direction.

4. The polarization drift

A polarization drift is set up when the electric field perpendicular to the magnetic field is time dependent. The ion drift is in the same direction as $d\mathbf{E}/dt$ and in the opposite direction for the electrons. This gives rise to a polarization current.

1.4.4 Anomalous transport

In a tokamak plasma the collisional transport of particles and energy is called neoclassical transport.[8] Unfortunately, in practice the experimental confinement times are much shorter than the neoclassical prediction. This is due to transport that is not accounted for in the theory and is called anomalous transport. It is thought that this "extra" transport is caused by turbulence due to instabilities in the plasma, which allows energy and particles to escape more quickly. This could take place through perturbations which cause either disruptions of the nested magnetic field structure or transport across the magnetic field, or both. This can either be small around the same size as the Larmor radius, called microinstabilities (e.g. the ion temperature gradient (ITG) mode) or large global modes called Magnetohydrodynamic (MHD) instabilities. To understand anomalous transport remains one of the most important challenges to theoretical tokamak physics.

1.5 The internal transport barrier (ITB)

The original operating mode of a tokamak, with a short confinement time and anomalous transport dominating, is called the L-mode. Under certain conditions, with increased heating power there is a transition into another mode, the H-mode, which has better confinement properties and is associated with an region of improved confinement at the plasma edge. In this region the density and temperature profiles are much steeper than in the rest of the plasma, this translates into much lower values of the transport coefficients for both the particles and heat. Another improved confinement regime occurs when there is a region of improved confinement in the plasma core, i.e. an internal transport barrier (ITB). Here, the ion thermal diffusivity is reduced to neoclassical levels in a narrow region of the plasma forming a "barrier" which confines thermal energy to the central region of the plasma.

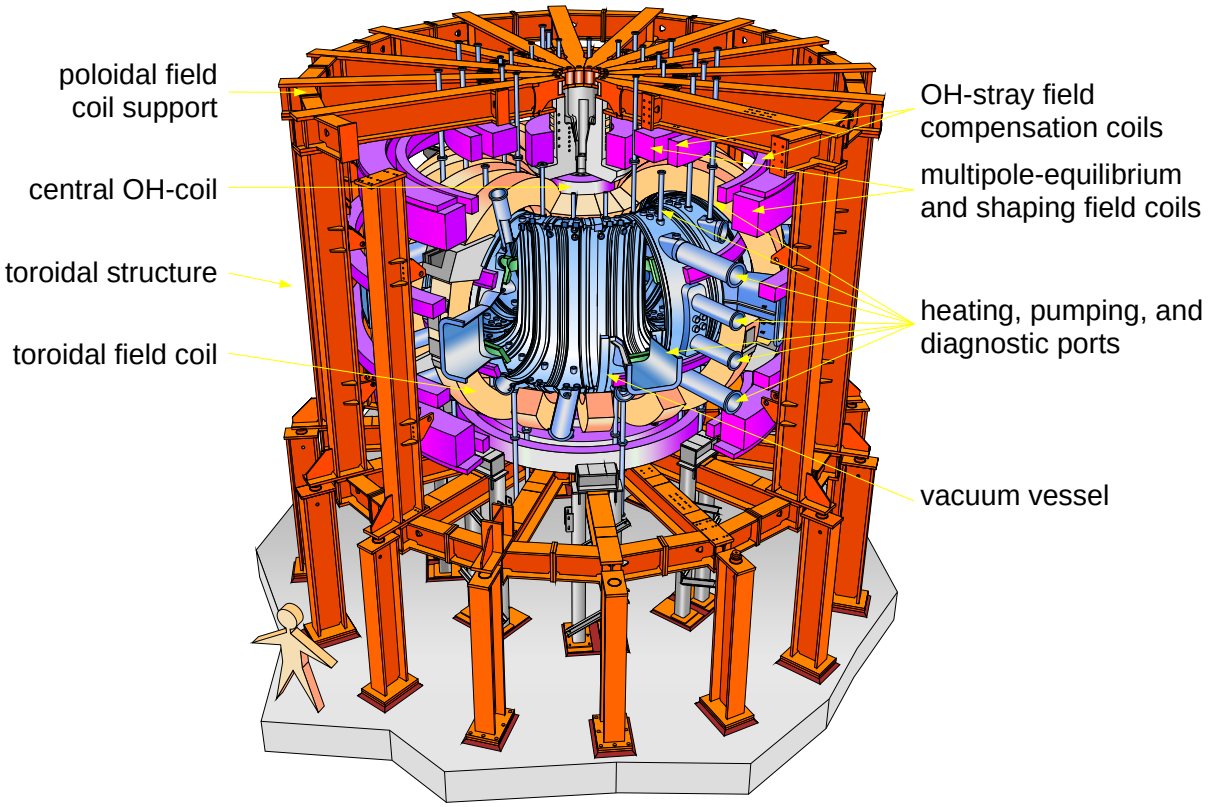

Figure 1.7: A diagram of the ASDEX Upgrade tokamak.

The non-linear dynamics at work during ITB formation or sustainment are not well understood. ITBs on ASDEX Upgrade, see figure 1.7, are produced by applying neutral beam injection (NBI) in the current ramp up phase. This produces a hollow current density and a non-monotonic q profile. While a detailed study into the power threshold for ITB formation has thus far not been undertaken at ASDEX Upgrade, it should be noted that ITBs are not seen to form in discharges with less than 5MW NBI in the ramp up phase. With only neutral beam heating ITBs are seen mainly in the ion temperature channel, and generally not in the electron temperature or density channels. All ITB discharges found and examined in this thesis have negative magnetic shear or a very flat q profile.

It is generally expected that the ion temperature gradient (ITG) driven turbulence

is the dominant in ITB plasmas, and also in H-mode plasmas. A simple picture of the toroidal ITG instability is given in section 1.6. The generally accepted model [9, 10] describing confinement improvement during a transport barrier event is that low or negative magnetic shear acts as a facilitator for $E \times B$ shear which suppresses turbulence. Negative or low magnetic shear allows stabilization of high n MHD modes and $q > 1$ everywhere stabilizes the sawtooth instabilities. The addition of heating power and, possibly, angular momentum input, in the absence of these instabilities, allows pressure and toroidal rotation gradients to build, thus a sheared electric field is generated which reduces anomalous transport locally, and allows the steep pressure gradient to persist. A local transport bifurcation can occur based on the $E \times B$ shear de-correlation of turbulence. This model has the universality to explain turbulence reduction and confinement improvement and is in qualitative agreement with various experiments[11, 12, 13, 14, 15, 16, 17, 18].

The internal transport barrier has two possible uses for fusion research. Firstly, it can be harnessed experimentally to improve confinement, and secondly it can be used as a vehicle for improving the understanding of the processes involved in anomalous transport and turbulence suppression. It is generally important to be able to control ITB formation not just for improving confinement but also, and possibly more importantly, there may be situations where ITB formation would be undesirable, for example in ITER. One possible way to avoid an ITB would be to delay the NBI heating until the current density profile is monotonic.

There is a great necessity to test the various theoretical models of turbulence suppression against experimental results and ITBs provide the ideal testing ground to facilitate this. This thesis attempts to clarify the understanding of ITBs and highlight the implications for transport and turbulence theory.

1.6 A simplified description of the toroidal ITG driven instability

In the following sections the ion temperature gradient (ITG) instability and its stabilizing mechanisms are discussed, the theory presented here is based on [19]. The ITG instability is expected to be the instability that governs ion heat transport in tokamak plasmas. Normally the ion temperature gradient is observed to have a fixed value close to $R/L_{Ti} = 6$. That is, in plasmas without transport barriers, the gradient does not exceed the critical one by a large amount since above this gradient the ITG instability is activated and transport increases rapidly. In ITB discharges the ion temperature gradient is far above the critical one, in the region of the ITB and one would expect that transport in this region should be very large. However, over this region the heat transport, is seen experimentally to be reduced to nearly neoclassical levels, this indicates that there must be a mechanism by which the ITG mode is stabilized. The toroidal ITG mode is mainly connected to the particle drifts perpendicular to the magnetic field. The parallel dynamics can be neglected in the lowest order calculation of the dispersion relation. This will allow the growth rate of the modes to be reasonably calculated. The dynamics of the mode are due to the combination of the curvature and ∇B ion drifts ($\mathbf{v}_d$) on the one hand and the $\mathbf{E} \times \mathbf{B}$ drift ($\mathbf{v}_E$) on the other. Assuming that there is only a toroidal magnetic field and a low β tokamak plasma, the curvature and ∇B drifts can be combined into

$$\mathbf{v}_d = -\frac{v_\parallel^2 + v_\perp^2/2}{\omega_c R}\mathbf{e}_y, \tag{1.10}$$

where ω_c is the cyclotron frequency and $\mathbf{e}_y$ is a unit vector in the vertical direction see figure 1.8. While the $\mathbf{E} \times \mathbf{B}$ drift is given by

$$\mathbf{v}_E = \frac{\mathbf{E} \times \mathbf{B}}{B^2} = -\frac{\nabla\phi \times \mathbf{B}}{B^2} = \frac{\hat{\mathbf{b}} \times \nabla\phi}{B}. \tag{1.11}$$

An approximated description of the frequency and growth rate of the mode can be

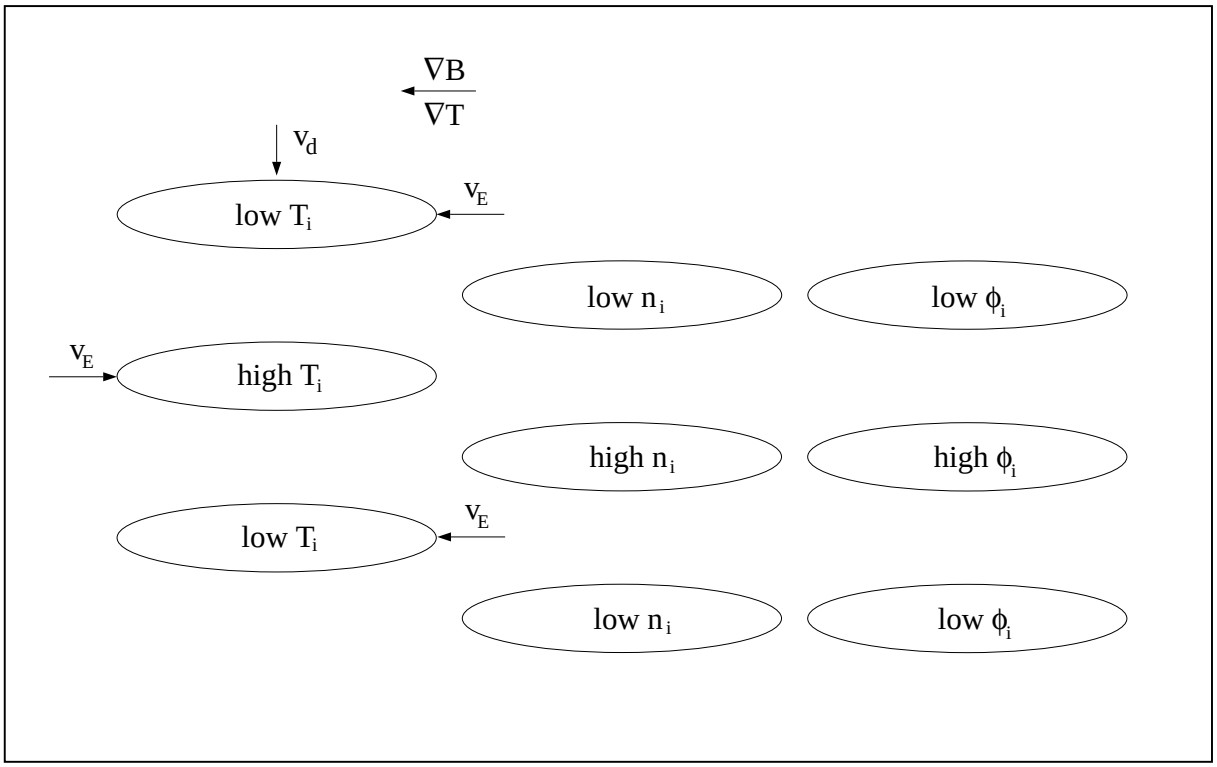

Figure 1.8: Contours of perturbed T_i, n_i and ϕ_i

obtained in slab geometry [20]. Consider a temperature perturbation on the low field side of the tokamak as shown in figure 1.8. The poloidal ion drift, due to both the ∇B and the magnetic field curvature, is proportional to T_i and is directed downwards. The drift then leads to a compression of the ion density, with increased density below the hot spots and above the cold spots. The constraint of quasi-neutrality means that there is an equal, and in phase, electron density perturbation. This electron density perturbation in turn causes a pressure perturbation which leads to a force along the field lines. The electron pressure is balanced by an electric field. Thus, the density perturbation has a direct proportional relation to the perturbed electrostatic potential ϕ, see figure 1.8. This is known as the adiabatic electron response. The electric field induces a radial $\mathbf{E} \times \mathbf{B}$ drift, which carries plasma from higher B into the hotter region and from lower B into the colder region. Thus, on the low field side, where ∇T_i is parallel to ∇B, this serves to reinforce the perturbation and a feedback loop is created.

Conversely on the high field side, where ∇T_i is reversed, hot plasma is carried into the cold region and cold plasma is carried into the hot region, and the perturbation is effectively suppressed.

1.6.1 The equations that describe the ITG mode

In this section a simple dispersion relation is derived which in later sections is used to describe important physical effects on the mode. With the simple picture, which was illustrated in the last section, in mind one can set about deriving the equations which describe the dynamics of the ITG mode. The gyro-kinetic equation, neglecting parallel ion motion (i.e. setting $k_\parallel = 0$), is:

$$\frac{\partial f}{\partial t} + (\mathbf{v}_d + \mathbf{v}_E) \cdot \nabla f - \frac{e}{m v_\parallel} \mathbf{v}_d \cdot \nabla \langle \phi \rangle \frac{\partial f}{\partial v_\parallel} = 0, \tag{1.12}$$

where $\mathbf{v}_E = \hat{\mathbf{b}} \times \nabla \langle \phi \rangle / B = -ik \langle \phi \rangle \mathbf{e}_R / B$ is the $\mathbf{E} \times \mathbf{B}$ velocity, ϕ is the perturbed electrostatic potential and $\langle \phi \rangle$ means the gyro-averaged ϕ. The simplifications made are: $\mathbf{B} = B\mathbf{e}_z$ and $\nabla_\parallel f = 0$.

All perturbed quantities are assumed to be of the form

$$\tilde{g}(x,t) = \tilde{g} exp[i\mathbf{k}_y \cdot \mathbf{x} - i\omega t],$$

such that $\nabla \tilde{g} = ik\tilde{g}\mathbf{e}_y$ and $\partial \tilde{g}/\partial t = -i\omega \tilde{g}$.

Linearizion of the governing equations is achieved by writing each factor in the equations as a sum of its equilibrium value and the small perturbation, i.e. $g = g_0 + \tilde{g}$. Thus, one can write equation (1.12) in linearized form

$$\frac{\partial f}{\partial t} + \mathbf{v}_d \cdot \nabla f = -\mathbf{v}_E \cdot \nabla F_M + \frac{e}{m v_\parallel} \mathbf{v}_d \cdot \nabla \langle \phi \rangle \frac{\partial F_M}{\partial v_\parallel}, \tag{1.13}$$

where F_M is the background distribution function which is assumed to be a Maxwellian.

$$F_M = \frac{n}{\pi^{3/2} v_{th}^3} exp\left[-\frac{v^2}{v_{th}^2}\right].$$

With,

$$\nabla_r F_M = \left[\frac{\nabla n}{n} + \left(\frac{v^2}{v_{th}^2} - \frac{3}{2}\right)\frac{\nabla T}{T}\right], \qquad \frac{\partial F_M}{\partial v_\parallel} = -\frac{2v_\parallel}{v_{th}^2} F_M, \tag{1.14}$$

and using the definition of the gradient lengths, $1/L_N \equiv -\nabla n/n$ and $1/L_T \equiv -\nabla T/T$, equation (1.13) becomes

$$-i\omega f - ik\frac{v_\parallel^2 + v_\perp^2/2}{\omega_c R} f = -ik\frac{\langle\phi\rangle}{BR} F_M \left[\frac{R}{L_N} + \left(\frac{v^2}{v_{th}^2} - \frac{3}{2}\right)\frac{R}{L_T} - 2\frac{v_\parallel^2 + v_\perp^2/2}{v_{th}^2}\right]. \tag{1.15}$$

Now one can derive the evolution equations for velocity space moments of equation (1.15). The first moment gives the density and the second even moment gives the pressure, i.e.:

$$n = \int d^3\mathbf{v} f$$
$$p_\parallel = \int d^3\mathbf{v} m v_\parallel^2 f$$
$$p_\perp = \frac{1}{2}\int d^3\mathbf{v} m v_\perp^2 f$$
$$p = \frac{1}{3}\int d^3\mathbf{v} m (v_\parallel^2 + v_\perp^2) f.$$

It is assumed that the ion temperature is isotropic, i.e. $T_\parallel = p_\parallel/n = T_\perp = p_\perp/n$, such that $1/2(p_\parallel + 2p_\perp) = 3/2nT$, and the moments of the terms of equation (1.15) are as

follows:

$$\int d^3\mathbf{v} i\omega f = i\omega\tilde{n}$$
$$\int d^3\mathbf{v} \frac{1}{2}mv^2 i\omega f = \frac{3}{2}i\omega\widetilde{nT} = \frac{3}{2}i\omega\tilde{n}T_0 + \frac{3}{2}i\omega\tilde{T}n_0$$
$$\int d^3\mathbf{v} ik\frac{v_\parallel^2 + v_\perp^2/2}{\omega_c R} f = \frac{2ik}{eBR}\widetilde{(nT)} = \frac{2ik}{eBR}\left[n_0\tilde{T} + \tilde{n}T_0\right]$$
$$\int d^3\mathbf{v} \frac{1}{2}mv^2 ik\frac{v_\parallel^2 + v_\perp^2/2}{\omega_c R} f = \frac{ikT_0}{eBR}\left[5\tilde{n}T_0 + 10n_0\tilde{T}\right]$$
$$\int d^3\mathbf{v} \frac{R}{L_N} F_M = n_0\frac{R}{L_N}$$
$$\int d^3\mathbf{v} \frac{1}{2}mv^2 \frac{R}{L_N} F_M = \frac{3}{2}\frac{R}{L_N}T_0 n_0$$
$$\int d^3\mathbf{v} \left(\frac{v^2}{v_{th}^2} - \frac{3}{2}\right) F_M = 0$$
$$\int d^3\mathbf{v} \frac{1}{2}mv^2 \left(\frac{v^2}{v_{th}^2} - \frac{3}{2}\right) F_M = \frac{3}{2}$$
$$\int d^3\mathbf{v} \quad 2\frac{v_\parallel^2 + v_\perp^2/2}{v_{th}^2} F_M = 2n_0$$
$$\int d^3\mathbf{v} mv^2 \frac{v_\parallel^2 + v_\perp^2/2}{v_{th}^2} F_M = 5T_0 n_0.$$

Hence, the density and temperature equations become:

$$\omega\tilde{n} + \frac{2k}{eBR}\left[n_0\tilde{T} + \tilde{n}T_0\right] = kn_0\frac{\langle\phi\rangle}{BR}\left[\frac{R}{L_N} - 2\right], \tag{1.16}$$

$$\frac{3}{2}\omega\tilde{n}T_0 + \frac{3}{2}\omega\tilde{T}n_0 + \frac{kT_0}{eBR}\left[5\tilde{n}T_0 + 10n_0\tilde{T}\right] = kn_0T_0\frac{\langle\phi\rangle}{BR}\left[\frac{3}{2}\frac{R}{L_N} + \frac{3}{2}\frac{R}{L_T} - 5\right]. \tag{1.17}$$

Substituting the density equation into the temperature equation for $\omega\tilde{n}$ one finds:

$$\omega n_0\tilde{T} + \frac{kT_0}{eBR}\left[\frac{4}{3}\tilde{n}T_0 + \frac{14}{3}n_0\tilde{T}\right] = kn_0T_0\frac{\langle\phi\rangle}{BR}\left[\frac{R}{L_T} - \frac{4}{3}\right]. \tag{1.18}$$

Then, using quasi-neutrality and the adiabatic electron response

$$n_i = n_e = n_0\frac{e\phi}{T_e}, \tag{1.19}$$

and normalizing the equations using;

$$\omega_D = -\frac{kT}{eBR}, \tilde{n} \rightarrow \frac{n}{n_0}, \tilde{T} \rightarrow \frac{T}{T_0}, \phi \rightarrow \frac{e\phi}{T_0}, \omega \rightarrow \frac{\omega}{\omega_D}.$$

Equations (1.16), (1.18) and (1.19) form a closed system with three equations and three unknowns n, T and ϕ. Thus, finally one arrives at the equations which describe the behavior of the ITG mode.

$$\omega n - 2(n+T) = -\left[\frac{R}{L_N} - 2\right]\langle\phi\rangle \tag{1.20a}$$

$$\omega T - \frac{4}{3}n - \frac{14}{3}T = -\left[\frac{R}{L_T} - \frac{4}{3}\right]\langle\phi\rangle \tag{1.20b}$$

$$n = \frac{\phi}{\tau} \tag{1.20c}$$

Here, τ is the ion to electron temperature ratio, T_i/T_e. Thus, finally one arrives at the equations which describe the behavior of the ITG mode. In the rest of this section the different effects of the individual terms of equations (1.20a) and (1.20b) will be discussed.

1.6.2 The threshold of the ITG mode

The equations (1.20) a, b and c contain more physics than the simple picture discussed in section 1.6. In this simple picture the temperature perturbation generates a density perturbation, this is described by the reduced equation

$$\omega n - 2T = 0, \tag{1.21}$$

i.e. the drift of the density perturbation ($2n$ in equation (1.20a)) as well as the effect of the electric field on the density evolution (right hand side of equation (1.20a)) are neglected. The obtained density perturbation in the simple model then leads to a potential perturbation through the adiabatic electron response given by

$$\phi = \tau n_0 \tag{1.22}$$

in agreement with equation (1.20c).

In the simple model this potential perturbation then drives the temperature perturbation,

$$\omega T = -\frac{R}{L_T}\phi. \tag{1.23}$$

Again comparing this equation with equation (1.20b) one sees that the drift of the temperature perturbation ($14T/3$), the generation of a temperature perturbation by the density perturbation ($4n/3$) as well as the change in energy due to the drift in the potential ($v_d\dot{\nabla}\langle\phi\rangle \longrightarrow 4/3\langle\phi\rangle$ on the right hand side) are neglected. The simple description leads to a purely growing mode given by

$$\omega = \left(-\tau\frac{R}{L_T}\right)^{\frac{1}{2}}, \tag{1.24}$$

with the growth rate depending on the ion temperature gradient as well as the electron to ion temperature ratio. The terms neglected in the simple picture will, however, lead to qualitative differences when included. One of these differences is the threshold in the ion temperature gradient below which the mode is stable. To illustrate this in the equations one must return to the more complete picture described by equations (1.20), again letting $R/L_N = 2$ and neglecting the finite Larmor radius effects. Substituting (1.20c) into (1.20b) one finds:

$$\left(\omega - \frac{14}{3}\right)T = -\left[\frac{R}{L_T} - \frac{4}{3} - \frac{4}{3\tau}\right]\phi. \tag{1.25}$$

Now, one can conceptualize the first component of the threshold by leaving aside the 14/3 term for the moment from equation (1.25) (this term is due to the drift). In this way it becomes evident that the temperature gradient must overcome a threshold in order for the mode to grow. So, one has a first approximation of the normalized critical gradient length:

$$\frac{R}{L_{Tcrit}} = \frac{4}{3} + \frac{4}{3\tau}.$$

Here the first term comes from the particle drift in the potential which accelerates (or decelerates) the ions, i.e. an energy or temperature perturbation is excited opposite to the original temperature perturbation. The second term comes from the particle drift itself, $\mathbf{v_d}$, which causes the density perturbation to generate a temperature perturbation such that the initial perturbation is reduced.

If one now re-includes the 14/3 term into the calculations one finds a correction to the normalized critical gradient length. This correction can be evaluated by:

$$(\omega - 2)n - 2T = 0, \tag{1.26a}$$

$$\left(\omega - \frac{14}{3}\right) T - \frac{4}{3}n = -\left[\frac{R}{L_T} - \frac{4}{3}\right] \phi. = -C\phi \tag{1.26b}$$

Substituting equations (1.26a) and (1.26b) yields:

$$\omega^2 - \frac{20}{3}\omega + \frac{28}{3} + 2\tau C = 0. \tag{1.27}$$

This third term is also related to the particle drift, $\mathbf{v_d}$. Due to the energy dependence of the drift, the velocity of propagation of the density and temperature perturbations is different. This difference in velocity can change the phase relation between density and temperature perturbations, which is stabilizing for the mode and raises the threshold in R/L_T. The threshold for C can be calculated to be

$$C = \frac{8}{9\tau}, \tag{1.28}$$

thus, the equation for the normalized critical temperature gradient length becomes

$$\frac{R}{L_{Tcrit}} = \frac{4}{3} + \frac{4}{3\tau} + \frac{8}{9\tau}. \tag{1.29}$$

Thus, no one physical effect determines the threshold.

The calculation presented above has been simplified. By considering equations (1.20) once more it can be seen that a more detailed analysis would uncover a dependence of

the R/L_{Tcrit} on R/L_N. This dependence is analyzed for a number of ITB discharges in section 4.2 and is found to be more or less linear, with higher values of R/L_N giving a higher threshold for R/L_T such that the density gradient can be stabilizing for the ITG mode. It can been seen from equation (1.29) that the threshold is also dependent on τ. The ratio of ion to electron temperature is stabilizing for ITG modes, simply because for a given density perturbation the potential perturbation scales linearly with the electron temperature. To illustrate an example of a typical value for R/L_{Tcrit} consider again the case where $R/L_N = 2$ and take $\tau = 1$, which would be the case before an ITB event, then the threshold in the temperature gradient length is:

$$\frac{R}{L_{Tcrit}} = 3.6 \tag{1.30}$$

This would be considered the minimum value for R/L_{Tcrit} see figure 4.4 in section 4.2. It is not far from the observed ITG threshold in H-mode discharges which is between 5 and 7.

1.6.3 The ITG and the density gradient

As mentioned above the density gradient is stabilizing for the mode and its effects will be formulated in this section. Taking the density equation (1.20a), and using $< \phi >= \phi$ and $\omega = \omega_R + i\gamma$, one can rearrange to get:

$$\frac{\phi}{\tau} = n = \frac{\left(\omega_R - 2 - 2\tau + \frac{R}{L_N}\tau\right) - i\gamma}{\left(\omega_R - 2 - 2\tau + \frac{R}{L_N}\tau\right)^2 + \gamma^2} 2T \tag{1.31}$$

The simple picture has shown that ϕ and T must be out of phase. Thus, the drive for the mode will be largest when the imaginary part has a maximum. This will be when the real part has a minimum at

$$\omega_R = 2 + 2\tau - \frac{R}{L_N}\tau. \tag{1.32}$$

Equation 1.32 shows that at the maximum growth rate of the mode the frequency would decrease with increasing density gradient. In fact, a high density gradient would cause the mode to rotate in the electron diamagnetic direction instead of the ion diamagnetic direction. If the same exercise were repeated for the ion heat balance equation, equation (1.20b) one would find a maximum drive at frequencies in the ion diamagnetic direction. Of course, the mode will have one frequency which can be thought to be a compromise between the two. Therefore the density gradient is stabilizing for an ITG mode. This is indeed observed when the more complete calculations of the growth rate are undertaken.

1.6.4 Geometry dependencies

The effect of magnetic shear on the ITG stability comes in through the field alignment of the mode. Due to the fast transport along the magnetic field the perturbations in density and temperature have a tendency to be constant along the field lines (They cannot be perfectly constant since the mode is ballooned and the perturbations are much smaller on the inboard compared with the outboard side). However, the pitch of the field lines, which is measured by the magnetic shear $\hat{s} = (r/q)dq/dr$ (see section 1.3), is a function of the radius of the flux surface. This means that an eddy structure on the low field side (of which a poloidal projection is shown in figure 1.9) is deformed when followed along the field lines. A rough idea of the deformation can be obtained through a field line mapping, see figure 1.9 b and c. The effect of the shear is two fold. Firstly, in case of strong positive or negative magnetic shear the eddies become stretched, this reduces the characteristic scale length and enhances the effect of the finite Larmor radius. The effect of the finite Larmor radius is stabilizing for the mode. Thus both positive and negative magnetic shear are stabilizing and that the maximum growth rate for the mode would be at $\hat{s} \approx 0$.

Secondly, the shearing of the field lines will cause the eddies to be tilted. Since the ITG

mode is caused by the compression of the density due to the drift, positive shear leads to the drive for the mode being maintained, whereas negative shear leads to a reduction of the drive, see figure 1.9. This second effect of the shear is destabilizing for positive shear and stabilizing for negative shear. Overall combining the two effects, positive shear is weakly stabilizing and negative shear is strongly stabilizing. The maximum growth rate position is displaced from $\hat{s} \approx 0$ to $\hat{s} \approx 0.5$.

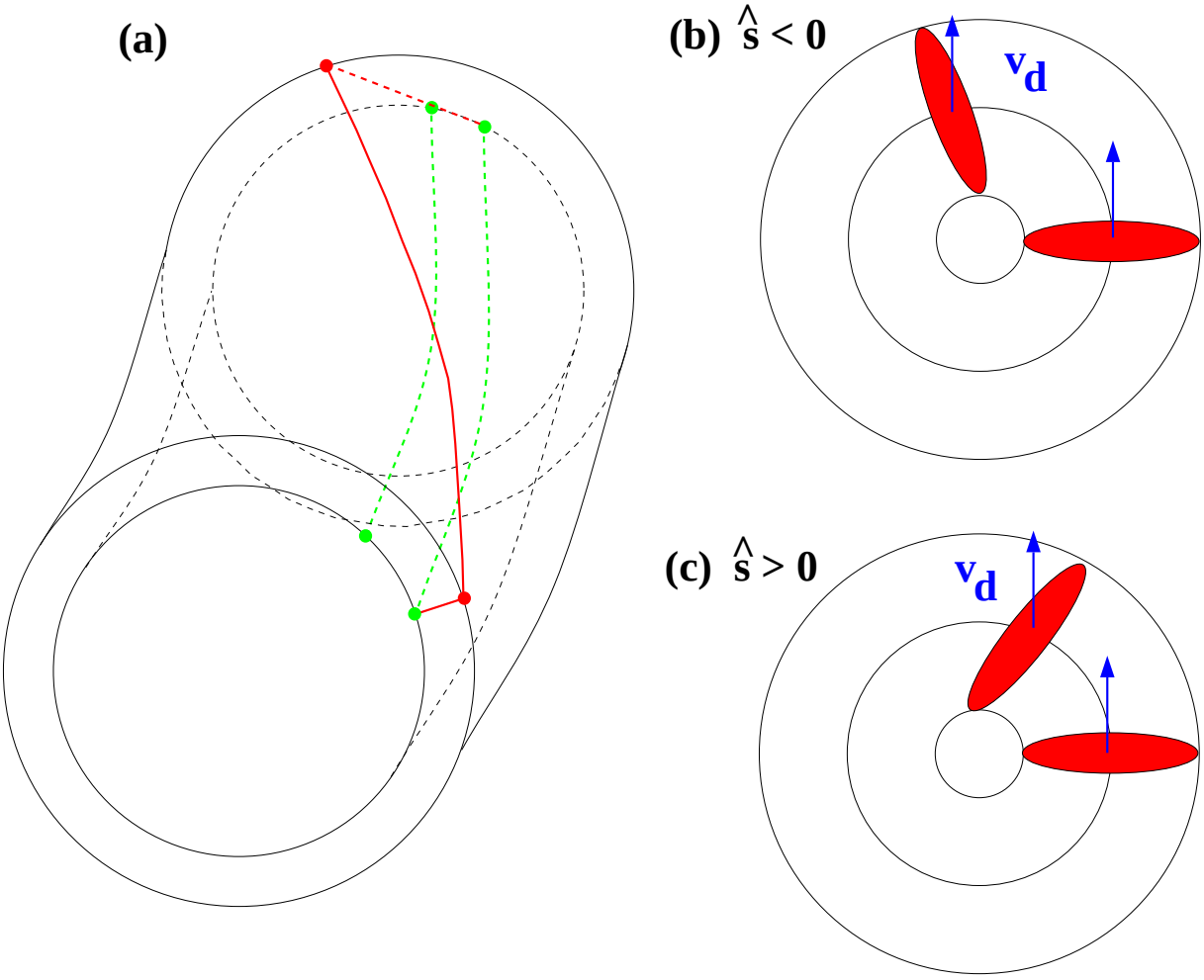

Figure 1.9: The effect of magnetic shear on eddy tilting. (a) Toroidal view of the magnetic field lines. (b) and (c) show a poloidal view of the effect of negative and positive shear, respectively, on the eddies.

The geometry effects also enter through the safety factor and through the Shafranov

shift. Avoiding certain q values in the plasma prevents MHD instabilities associated with these q values from entering the plasma. For instance, the sawtooth instability, which is associated with the $q = 1$ surface. The Shafranov shift (sometimes called the α-effect) is the deviation of the magnetic axis from its equilibrium position, always towards the low field side. It can be shown that this has the effect of reducing the local magnetic shear on the low field side while enhancing it on the high field side[21, 22]. Since the mode is located on the low field side it feels the effect of $\hat{s} = \hat{s}_{global} - \alpha$. In the case of ITB discharges, which are generally produced with a reversed q profile, including the Shafranov shift in the calculations will cause the mode to feel the effect of a lower, probably more negative, shear. This then would have a very stabilizing effect on the mode.

1.6.5 The $E \times B$ shear

Due to the presence of a radial electric field there is a $E \times B$ flow shear. The $E \times B$ flow shear is stabilizing for the ITG mode. In linear theory this mechanism is similar to the first effect of the magnetic shear, see figure 1.10. The tilting and the increase in the finite Larmor radius effects will lead to a stabilization of the mode.[23]

Non-linear theory predicts that the eddies also have an effect on each other. This effect happens only to neighboring eddies and the degree of influence depends on the length of time they spend in the vicinity of each other. However, the $E \times B$ flow shear causes the eddies to move past each other, the larger the flow shear the faster they move and the smaller the effect on each other.

The generally accepted condition for turbulence suppression due to $E \times B$ shear is when the shearing rate, $\omega_{E\times B}$, is of the order of or greater than the maximum linear growth rate, γ_{max}, $\omega_{E\times B} \geq \gamma_{max}$ [24]. $\omega_{E\times B}$ was calculated for these discharges using the

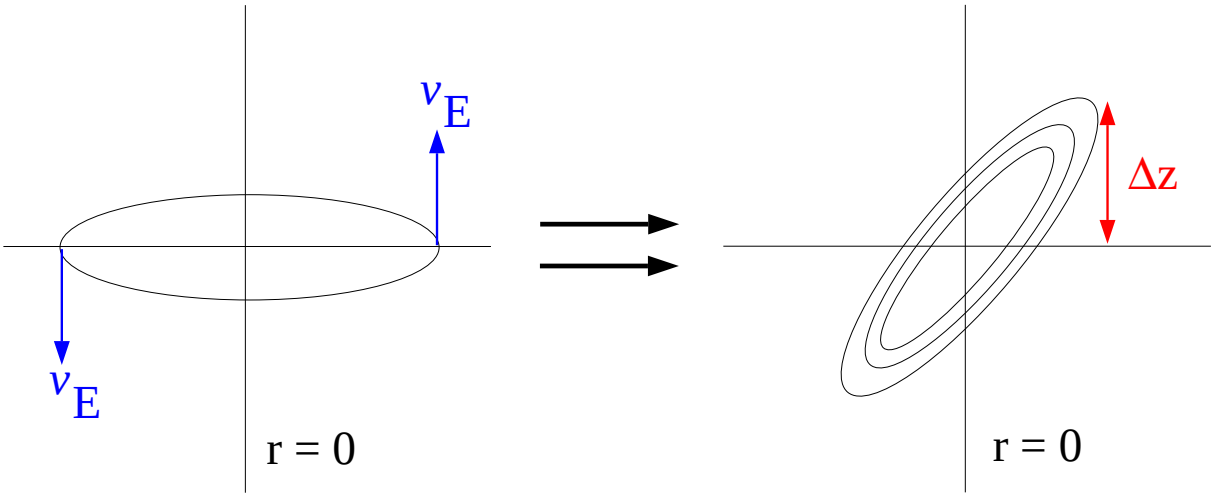

Figure 1.10: The linear picture: tilting of the eddy by $E \times B$ shear.

equation[25]

$$\omega_{E\times B} = \frac{(RB_p)^2}{B}\frac{\partial}{\partial\psi}\left[\frac{E_r}{RB_p}\right]$$

where R is the major radius, B_p is the poloidal magnetic field, B is the total magnetic field and E_r is the radial electric field given by the radial force balance

$$E_r = \frac{\nabla p_i}{Z_i e n_i} - v_{\theta,i}B_\phi + v_{\phi,i}B_\theta.$$

Here, $Z_i e$ is the charge and $v_{\theta,i}$ the poloidal velocity of the ions and p_i and n_i are the ion pressure and density respectively. Unfortunately, this criterion is not exact and it has been found that there can be up to a factor of 2.5 deviation from it[11][26].

1.7 Outline of this thesis

In recent years the fusion community has become attracted to internal transport barriers as a possible solution to the problem of confinement in tokamak plasmas. However, before this work was undertaken, a complete study of ITBs in ASDEX-Upgrade had not been carried out. In this thesis an exhaustive investigation of internal transport barrier dynamics in ASDEX-Upgrade is given.

The behavior of ITBs is intricately studied both experimentally and analytically, so that all clues as to the underlying theory can be appreciated. It is widely considered that during an ITB, anomalous transport is reduced in the region of the barrier. As mentioned before the area of anomalous transport is not well understood, however, there are a number of theoretical models which attempt to explain it. Hence, this work includes a comparison of the predictions of theoretical models with experimental results of ITB discharges. This allows a better understanding of ITBs and turbulent transport, and also acts as a check for the theoretical models.

In chapter 2 plasma equilibrium is introduced, as is the CLISTE interpretive equilibrium code. This code is used to recover the q-profile and associated error bars for ITB discharges, examples of these are given in this chapter.

A study of the ITB behavior over the duration of the discharge is presented in chapter 3. This is compared with the evolution of the q-profile in order to ascertain the effect of the safety factor on the ITB.

In chapter 4 the various possible turbulence stabilizing mechanisms, which have been suggested by theory, are examined experimentally. These include the density gradient, the $E \times B$ flow shear and the Shafranov shift.

In chapter 5 a derivation of the Shafranov shift is given. Also, the effect of various plasma shaping parameters on mode stability are studied analytically using the gyro-kinetic linear stability code, GS2.

The results of the ASTRA transport simulation of ITB discharges, using the GLF23 model, are presented in chapter 6. The ability of the model to predict the ITB behavior is investigated as are the mechanisms for ITB formation and sustainment.

Chapter 2

Equilibrium

As discussed in chapter 1 the plasma is confined by a magnetic field (**B**). The principal magnetic field is the toroidal field B_ϕ see figure 2.1(a). In order to have equilibrium, with the plasma pressure balanced by the Lorentz force, a poloidal magnetic field B_θ is needed.

B_ϕ is produced by the currents in the toroidal coils surrounding the plasma. B_θ is produced by the toroidal current in the plasma, as well as by the currents in the external coils which shape and position the plasma. The combination of B_ϕ and B_θ gives rise to an infinite set of nested toroidal magnetic surfaces. Thus, the magnetic field lines have a helical trajectory around the torus, see figure 2.1(b). In the following section plasma equilibrium is described and the Grad-Shafranov equation is derived, the derivation is based on chapter 1 in [27].

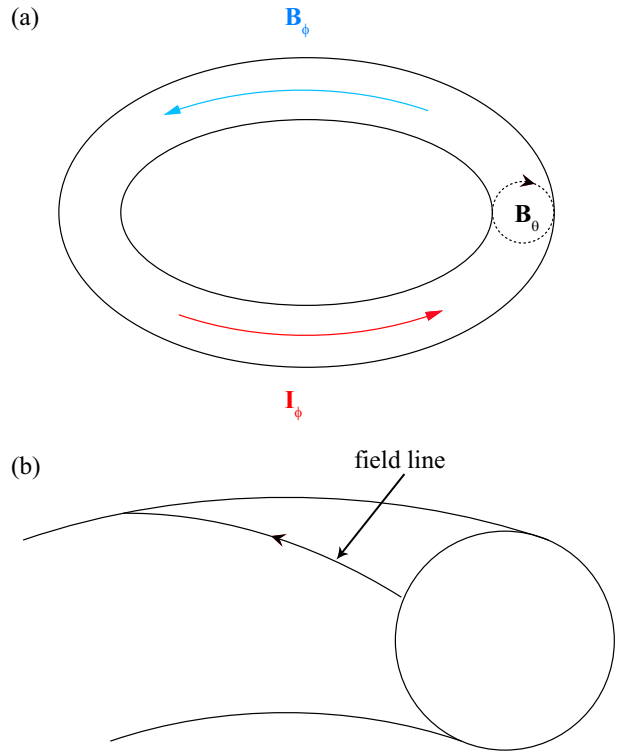

Figure 2.1: (a) The toroidal magnetic field B_ϕ, and the poloidal magnetic field B_θ due to the toroidal current I_ϕ. (b) The combination of B_ϕ and B_θ causes the field lines to twist around the plasma.

2.1 The Grad-Shafranov equation

The simplest useful mathematical model of fusion plasmas are the ideal magnetohydrodynamic (MHD) equations [28, 29, 30]. These consist of Euler equations for fluid motion coupled with Maxwell's equations for the evolution of magnetic fields (ignoring

the displacement current):

$$
\begin{aligned}
&\frac{\partial \rho}{\partial t} + \nabla \cdot (\rho \mathbf{v}) = 0, \\
&\rho \frac{\partial \mathbf{v}}{\partial t} + \rho(\mathbf{v} \cdot \nabla)\mathbf{v} + \nabla p - \mathbf{J} \times \mathbf{B} = 0, \\
&\frac{\partial p}{\partial t} + \mathbf{v} \cdot \nabla p + \frac{5}{3} p \nabla \cdot \mathbf{v} = 0, \\
&\frac{\partial \mathbf{B}}{\partial t} + \nabla \times \mathbf{E} = 0, \\
&\mu_0 \mathbf{J} = \nabla \times \mathbf{B}, \\
&\mathbf{E} + \mathbf{v} \times \mathbf{B} = 0, \\
&\nabla \cdot \mathbf{B} = 0.
\end{aligned}
\tag{2.1}
$$

Here, ρ is the mass density, $\mathbf{v}$ the flow velocity, p the pressure, $\mathbf{J}$ the current density, $\mathbf{B}$ the magnetic field, $\mathbf{E}$ the electric field, and μ_0 the vacuum magnetic permeability. SI units are employed. The first three equations describe mass, momentum, and energy conservation for an ideal fluid having an adiabatic index $\gamma = 5/3$. The next four equations are Maxwell's equations for an ideally conducting medium with the displacement current neglected. This system of equations provides a single-fluid description of macroscopic plasma behavior.

The ideal MHD model neglects many effects that are important in tokamak physics in one context or another. There is no heat conduction, particle diffusion, resistivity, or viscosity in the model. There is no displacement current or space charge, and also all particle kinetic effects are ignored. Therefore, other mathematical models are employed in order to represent either diffusive processes on the longer timescales, or a variety of waves and instabilities on short timescales. The ideal MHD model occupies a middle ground, in that the long-term plasma evolution proceeds by slow transport through a sequence of ideal MHD stable equilibria, whereas microscopic theory is needed in order to supply the transport coefficients.

In steady-state (slowly evolving) plasmas, one can set $\mathbf{v} = 0$ and $\partial/\partial t = 0$ in the system

of equations (2.1) to get

$$\nabla \cdot \mathbf{B} = 0, \tag{2.2}$$

$$\mathbf{J} \times \mathbf{B} = \mu_0{}^{-1}(\nabla \times \mathbf{B}) \times \mathbf{B} = \nabla p. \tag{2.3}$$

The basic condition for equilibrium is that the force on the plasma be zero at all points in the plasma. This means that the Lorentz force, $\mathbf{J} \times \mathbf{B}$, will balance the force due to the plasma pressure, p,

$$\mathbf{J} \times \mathbf{B} = \nabla p, \tag{2.4}$$

where $\mathbf{J}$ is the current density. This equation is referred to as the equilibrium equation. From equation (2.4) it follows that $\mathbf{B} \cdot \nabla p = 0$. There is no pressure along the magnetic field lines and the magnetic surfaces are also surfaces of constant pressure. In addition equation (2.4) gives $\mathbf{J} \cdot \nabla p = 0$, so the current lines also lie in the magnetic surfaces.

For a given toroidal magnetic surface consider the *cut surfaces* which span across the whole of the toroid, S_{pol}, and across a cross-section of the toroid, S_{tor}, as shown in figure 2.2. Through any cross-section of the toroid, S_{tor}, the *toroidal flux* is

$$\psi_{tor} = \int_{S_{tor}} \mathbf{B} \cdot d\mathbf{S}$$

while through any cut surface spanning the hole in the toroid, S_{pol} the *poloidal flux* is

$$\psi_{pol} = \int_{S_{pol}} \mathbf{B} \cdot d\mathbf{S}.$$

Using $\nabla \cdot \mathbf{B} = 0$ and Gauss' theorem, it can be shown that the flux is the same for all surfaces spanning the same contour. Furthermore, there is no flux through the toroidal magnetic surface since $\mathbf{B}$ is everywhere tangent to it. Therefore, the flux is the same through any topologically equivalent contour (C_{tor} or C_{pol}) on the flux surface. It follows that both ψ_{tor} and ψ_{pol} are surface quantities. A *surface quantity* is any variable that is uniform over a magnetic surface.

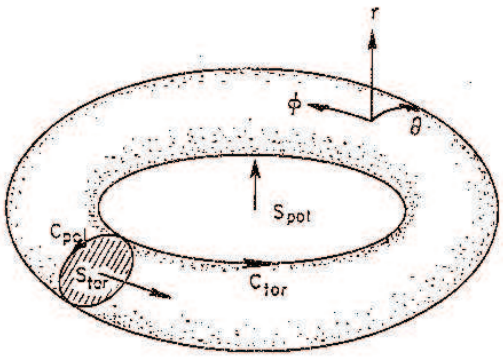

Figure 2.2: Toroidal flux surface showing cut surfaces and contours.

Axisymmetric equilibrium. In the case of axisymmetry ($\frac{\partial}{\partial\phi} = 0$) in cylindrical coordinates (R, ϕ,Z), the conditions for a stationary equilibrium, equation (2.3), reduces to a scalar partial differential equation. Firstly, one can write the total magnetic field as $\mathbf{B} = \mathbf{B}_{tor} + \mathbf{B}_{pol}$ where $\mathbf{B}_{tor} = (0, B_\phi, 0)$ and $\mathbf{B}_{pol} = (B_R, 0, B_Z)$. Note all three components are functions of R, Z only. Writing $\mathbf{B}_{pol} = \nabla \times \mathbf{A}$ one has (zeroing $\partial/\partial\phi$ terms)

$$\mathbf{B}_{pol} = \left(-\frac{\partial A_\phi}{\partial Z},\ \frac{\partial A_R}{\partial Z} - \frac{\partial A_Z}{\partial R},\ \frac{1}{R}\frac{\partial (R\,A_\phi)}{\partial R} \right).$$

The only constraint on A_R and A_Z is that the ϕ component of $\mathbf{B}_{pol}$ vanish. Hence one can set $A_R = A_Z = 0$ and then $\mathbf{B} = \nabla \times (A_\phi \hat{\phi}) + B_\phi \hat{\phi}$. To express A_ϕ in terms of the poloidal flux enclosed by a magnetic surface, one uses Stokes' theorem to get (the contour C_{pol} is chosen to be a circle of radius R)

$$\begin{aligned} \psi_{pol} &= \int_{S_{pol}} \mathbf{B} \cdot d\mathbf{S} \\ &= \int_{S_{pol}} \left(\nabla \times (A_\phi \hat{\phi}) \right) \cdot d\mathbf{S} + \int_{S_{pol}} B_\phi \hat{\phi} \cdot d\mathbf{S} \\ &= \oint_{C_{pol}} A_\phi \hat{\phi} \cdot d\mathbf{l} \ + \ 0 \\ &= 2\pi R A_\phi. \end{aligned} \tag{2.5}$$

Defining a stream function $\psi \equiv \psi_{pol}/2\pi$ one now has (note $\nabla\phi = \hat{\phi}/R$)

$$\mathbf{B} = \nabla \times (\psi \nabla\phi) + B_\phi \hat{\phi}, \tag{2.6a}$$

$$= \nabla\psi \times \nabla\phi + B_\phi \hat{\phi}, \tag{2.6b}$$

$$= -\frac{1}{R}\frac{\partial\psi}{\partial Z}\hat{\mathbf{R}} + \frac{1}{R}\frac{\partial\psi}{\partial R}\hat{\mathbf{Z}} + B_\phi\hat{\phi}. \tag{2.6c}$$

Since $\psi \propto \psi_{pol}$ it is a surface quantity, and it may be used to label the flux surfaces. Hence any surface quantity can also be regarded as a *flux function.* Using equation (2.6), the current density $\mathbf{J} = {\mu_0}^{-1}\nabla \times \mathbf{B}$ can be expressed in the form

$$\mu_0\mathbf{J} = \nabla \times \mathbf{B}_{pol} + \nabla \times \mathbf{B}_{tor} \tag{2.7a}$$

$$= \left(-\frac{1}{R}\frac{\partial^2\psi}{\partial Z^2} - \frac{\partial}{\partial R}\left[\frac{1}{R}\frac{\partial\psi}{\partial R}\right]\right)\hat{\phi} + \nabla \times (B_\phi R\nabla\phi) \tag{2.7b}$$

$$= -\frac{1}{R}\Delta^*\psi\,\hat{\phi} + \nabla(RB_\phi) \times \nabla\phi, \tag{2.7c}$$

where Δ^* is a special operator defined by

$$\Delta^*\psi \equiv R\frac{\partial}{\partial R}\frac{1}{R}\frac{\partial\psi}{\partial R} + \frac{\partial^2\psi}{\partial Z^2}, \tag{2.8}$$

the choice of the later symbol is due to its similarity to the Laplacian in cylindrical coordinates.

From $\mathbf{B}\cdot\nabla p = \mathbf{B}\cdot\mathbf{J}\times\mathbf{B} = 0$ it follows that the pressure is a surface quantity:

$$p = p(\psi)$$

Substitution of equations (2.6b) and (2.7c) into the force balance equation $\nabla p = \mathbf{J}\times\mathbf{B}$ yields (note in the following cross product expansion $\nabla(RB_\phi)\cdot\hat{\phi} = 0$ by axisymmetry)

$$\begin{aligned}\mu_0 p'(\psi)\nabla\psi &= \left(-\frac{1}{R}\Delta^*\psi\,\hat{\phi} + \nabla(RB_\phi)\times\nabla\phi\right)\times\left(\nabla\psi\times\nabla\phi + B_\phi\hat{\phi}\right)\\ &= -\frac{1}{R^2}\Delta^*\psi\,\nabla\psi \;-\; \frac{B_\phi}{R}\nabla(RB_\phi).\end{aligned} \tag{2.9}$$

For this equation to hold everywhere, one must have $\nabla(RB_\phi) \parallel \nabla\psi$. Thus RB_ϕ must be a surface quantity, say $F(\psi)$.

Since $\mathbf{J} \cdot \nabla p = 0$, current density field lines must also lie on magnetic surfaces. Hence the poloidal current,

$$I_{pol} = \int_{S_{pol}} \mathbf{J} \cdot d\mathbf{S}$$

is also a flux function. Substituting for $\mathbf{J}$ from equation (2.7a) yields

$$\begin{aligned} \mu_0 I_{pol} &= \int_{S_{pol}} \nabla \times \mathbf{B} \cdot d\mathbf{S} \\ &= \int_{S_{pol}} -\frac{1}{R}\Delta^*\psi\,\hat{\phi} \cdot d\mathbf{S} + \int_{S_{pol}} (\nabla \times (B_\phi R \nabla\phi)) \cdot d\mathbf{S} \\ &= \ 0 \ + \oint_{C_{pol}} B_\phi \hat{\phi} \cdot d\mathbf{l} \\ &= 2\pi R B_\phi. \end{aligned} \tag{2.10}$$

Thus $RB_\phi \equiv F(\psi) = \mu_0 I_{pol}/2\pi$ is proportional to the poloidal current, and, rearranging terms in equation (2.9), one obtains

$$-\Delta^*\psi = \mu_0 R^2\, p'(\psi) + F F'(\psi), \tag{2.11}$$

in which p and F are arbitrary functions of ψ alone. Note equation (2.7c) can now be expressed as

$$\begin{aligned} \mu_0 \mathbf{J} &= -\frac{1}{R}\Delta^*\psi\,\hat{\phi} + F'(\psi)\nabla\psi \times \nabla\phi \\ &= -\frac{1}{R}\Delta^*\psi\,\hat{\phi} \ - \ \frac{F'}{R}\frac{\partial\psi}{\partial Z}\hat{\mathbf{R}} + \frac{F'}{R}\frac{\partial\psi}{\partial R}\hat{\mathbf{Z}} \\ &\equiv \ \mu_0 \mathbf{J}_{tor} \ + \ \mu_0 \mathbf{J}_{pol}, \end{aligned} \tag{2.12}$$

so that one may also write

$$-\Delta^*\psi = \mu_0 R\, J_\phi. \tag{2.13}$$

Equation (2.11), commonly known as the Grad-Shafranov equation (GSE), is a weakly non-linear elliptic PDE which is solved by specifying the functions $p = p(\psi)$ and $F = F(\psi)$, together with boundary conditions or externally imposed constraints on ψ, and then inverting $\Delta^*\psi$ to determine $\psi = \psi(R, Z)$.

2.2 The q profile and error bars

As discussed in chapter 1 the safety factor or q profile and also the magnetic shear, which is related to the space derivative of q, are of particular interest in the study of ITBs. In order to examine the effects of the q profile on ITB behavior the q profile was calculated using the CLISTE equilibrium code constrained with Motional Stark Effect (MSE) diagnostic data.

2.2.1 The CLISTE Interpretive Equilibrium Code

CLISTE [1] is an acronym for CompLete Interpretive Suite for Tokamak Equilibria.

The CLISTE code[27, 31] finds a numerical solution to the Grad-Shafranov equation, equation (2.11) [32, 33], for a given set of poloidal field coil currents and limiter structures by varying the free parameters in the parameterization of the $p'(\psi)$ and $FF'(\psi)$ source profiles which define the toroidal current density profile j_ϕ so as to obtain a best fit in the least squares sense to a set of experimental measurements. These measurements can include external magnetic data, MSE data, kinetic data, q-profile information from SXR measurements, etc., and the free parameters are varied such that the penalty or *cost function*, i.e. the squared modulus of the vector of (weighted) differences between the set of experimental measurements and those predicted by the equilibrium solution, is minimized.

2.2.2 The Mirnov diagnostic

The Mirnov diagnostic measures the magnetic field at several positions inside the vacuum vessel through the use of a number of magnetic coils. In principle with enough measurements of the magnetic field at the boundary of the plasma one can reconstruct the magnetic field inside the plasma as well. This is, however, not a well posed problem. Small errors in the magnetic field at the surface translate into large errors in the deter-

[1] *klish-teh*, Gaelic for clever

mination of the magnetic field inside the plasma. This means that the magnetic coils determine the magnetic field well only in the outer part of the plasma, i.e. at approximately $0.65 \leq \rho_{tor} \leq 1$. In the interior additional diagnostic information is required. This information is provided by the MSE diagnostic described in the next section.

2.2.3 The MSE diagnostic

High energy (70-140KeV) neutral Hydrogen or Deuterium beams are used to heat the plasma and they present a very powerful diagnostic tool to probe the inner regions of the plasma. It is possible to measure the local value of the magnetic field by exploiting the motional linear Stark effect. The beam neutrals experience a large Lorentz electric field given by , $E_L = V_{beam} \times B$, which leads to a significant Stark splitting of the emission lines. Viewing these lines at any angle other than 90° will show them to be Doppler shifted. The polarization pattern of the Stark spectrum is a direct measure of the local magnetic field direction. This allows the magnetic field to be accurately determined and consequently, current density related parameters can be recovered using CLISTE. With idealized MSE geometry the MSE diagnostic measures an accurate local measurement of the magnetic pitch angle γ, where:

$$\tan\gamma = \frac{B_\theta}{B_\phi}, \tag{2.14}$$

and, B_θ and B_ϕ are the magnitudes of the local poloidal and toroidal magnetic fields respectively. However, due to the non-ideal viewing geometry of the MSE diagnostic the γ that the diagnostic measures is actually a function of the components of B_θ, B_ϕ and the radial electric field

$$\tan\gamma = \frac{A_1 B_r + A_2 B_\phi + A_3 B_z + A_4 E_r + A_5 E_z}{A_6 B_r + A_7 B_\phi + A_8 B_z + A_9 E_r}, \tag{2.15}$$

where B_r and B_z are the cylindrical components of B_θ, A_i are the calibration geometrical

constants and E_r and E_z are components of the radial electric field.

The spatial resolution of the MSE diagnostic is 6cm at the plasma center, around 2cm at $\rho_{pol} = 0.3$ and around 9cm at the edge of the plasma. The AUG MSE diagnostic has a sampling rate of 1kHz but has only a 300Hz anti-aliasing filter. Also, taking into account the fact that the diagnostic signal is averaged over 3 time points means that the time resolution is reduced to 3ms. The combination of the spatial and time resolution leads to a maximum experimental error in γ of $\pm 0.2^{\circ}$ for the AUG MSE diagnostic. However, due to some limitations of the diagnostic the error on the innermost channel is much larger. Therefore, this channel has been left out of the calculations as it was considered that fitting it would be detrimental to the overall fit to the data.

The use of MSE data allows the determination of the internal magnetic field and from this, parameters related to the current density can be recovered. The q profile and hence the magnetic shear are related to the current density. A simplified but very useful approximation can be given for the case of a large aspect ratio tokamak with a circular cross-section

$$q(r) = \frac{2\pi r^2 B_\phi}{\mu_0 I(r) R}, \tag{2.16}$$

where r is the minor radius of the flux surface, R is the major radius, $I(r)$ is the current inside r, and the toroidal magnetic field is essentially a constant. The magnetic shear, $\hat{s}$ is related to the q profile (for the case of this simplified geometry) by

$$\hat{s} = \frac{r}{q}\frac{dq}{dr}. \tag{2.17}$$

In a normal H-mode discharge the q profile is monotonically increasing from the center of the plasma to the edge. However, the ITBs discharges analyzed here are produced in discharges with a non-monotonic q profile. This is due to the fact that there is NBI

heating during the current ramp up phase. A non-monotonic q profile means that the position of minimum q (q_{min}) is not at the center of the plasma but at some position between the center and edge of the plasma. A non-monotonic q profile is also referred to as a reversed q profile. Error bars on the recovered q profile are important since, if they are large they could show that a monotonic q profile could be non-monotonic within the error bars, and vice versa. At the time that this work was undertaken error bars on the q profile produced by CLISTE were not available. Hence, a method for approximating them was devised which involved using a Monte Carlo technique. This method is discussed in the next section.

2.2.4 Monte Carlo error bars on the q profile

The q-profile in the center of the plasma is mainly determined by the MSE diagnostic data (rather than the magnetics). Thus, the error in the reconstruction can therefore be estimated by considering the error on the MSE diagnostic channels alone. The maximum error on each of the MSE channels is 0.2 degrees, except on the innermost (most central) channel where the error is expected to be much larger. Due to the very large uncertainty on the innermost MSE channel it was not fitted in the CLISTE runs, neither was it used to approximate the error bars. The maximum error of 0.2 degrees on the other 9 channels was used to add noise to the MSE data to produce 100 different versions of the MSE data for each of the nine ITB discharges analyzed. The CLISTE code is also used to calculate the $E \times B$ shearing rate and at the same time as the noise was being added to the MSE data, noise was added to the toroidal rotation velocity, v_{tor}, data (an average error of 20% was assumed). Such that there was also 100 input files containing noisey v_{tor} data. Then the CLISTE equilibrium code was run for each of the 100 sets of input files. The results of the CLISTE code (i.e. the q profile and $\gamma_{E\times B}$ information) for the 100 runs were collected and averaging was used to get the mean and standard deviation of the results. Since, q profile and $\gamma_{E\times B}$ information was needed for all the

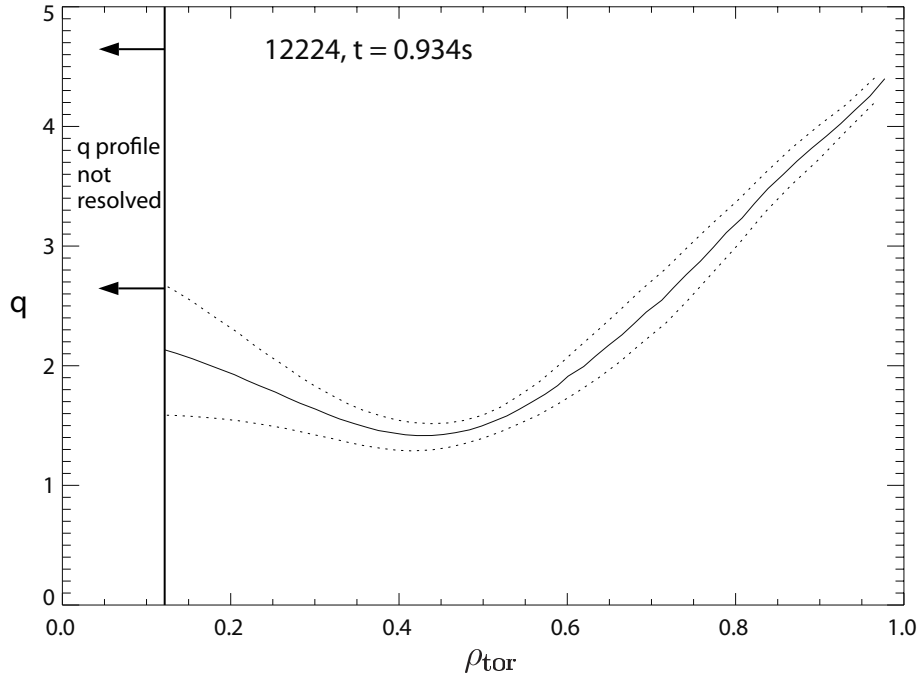

Figure 2.3: An example of a Monte Carlo q profile and error bars: limiter discharge 12224 at 0.934s $I_p \approx 1MA$, $B_t \approx -2.46T$ and $n_e \approx 2.8 \times 10^{19} m^{-3}$. The q profile towards the center is not resolved because the innermost MSE channel is not used in the equilibrium.

ITB discharges being analysed, this process was repeated for all nine of the discharges. The results for discharge 12224 are shown in figure 2.3, the error bars show two standard deviations or 95% error bars. Also, the results for discharge 13149 are shown in figure 2.4.

The method and results for the calculations of the error bars on the $\gamma_{E\times B}$ profiles is given in chapters 4.2 and 6.4. It is also possible to use the error bars on each MSE channel to directly calculate the error on the q profile. This method is discussed in the next section.

2.2.5 q profile error bars with CLISTE

Since the error bars on the MSE data are a maximum value, it is possible to use them in CLISTE to calculate error bars on the recovered q profile. Equation (2.16) gives the

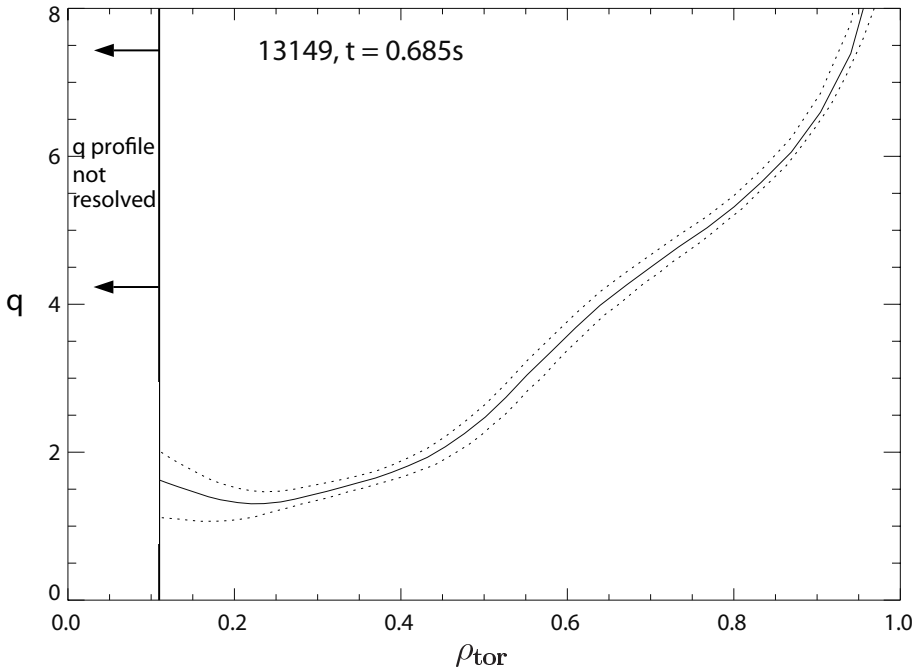

Figure 2.4: An example of a q profile and error bars: limiter discharge 13149 at 0.685s $I_p \approx 1MA$, $B_t \approx -2.78T$ *and* $n_e \approx 3.9 \times 10^{19} m^{-3}$. *The q profile towards the center is not resolved because the innermost MSE channel is not used in the equilibrium. The q profile error bars are calculated only in the region spanned by the MSE channels.*

equation for q in simplified cylindrical geometry, in general geometry the q profile is given by (see [34] for a detailed derivation)

$$q = \frac{|\nabla\phi|}{|\nabla\psi|} = \frac{\nabla\phi}{2\pi R B_\theta}, \tag{2.18}$$

this along with equation (2.15) shows that q is directly proportional to $\tan\gamma$. This means that by using a CLISTE equilibrium, in order to get the positions of the channels, one can calculate an "experimental" value for q which is (almost) independent of the equilibrium using the equation [34]

$$q_{exp} = q_{fit} \frac{B_{\theta(fit)}}{B_{\theta(exp)}}, \tag{2.19}$$

where q_{exp} is q value calculated directly from the MSE γ, q_{fit} is the fitted q value from CLISTE at the position of the MSE channel, $\mathbf{B}_{\theta(fit)}$ is the fitted magnetic field using CLISTE and $\mathbf{B}_{\theta(exp)}$ is directly from the MSE diagnostic. It is assumed that flux topology is consistent between the model and experiment. Using equation (2.19) the error bars on the q-value can be estimated by adding $\pm 0.2^{\circ}$ to the γ_{exp} and recalculating q_{exp}. These error bars can then be interpolated to include every position where q is calculated within the region spanned by the MSE channels. Figure 2.5 shows an example of a recovered q profile interpolated confidence bands for discharge 12224. Also, figure 2.6 shows the output q profile and error bars from CLISTE. Note that the q_{exp}, marked with a star, is shown to be not equal to the calculated q value, q_{fit}.

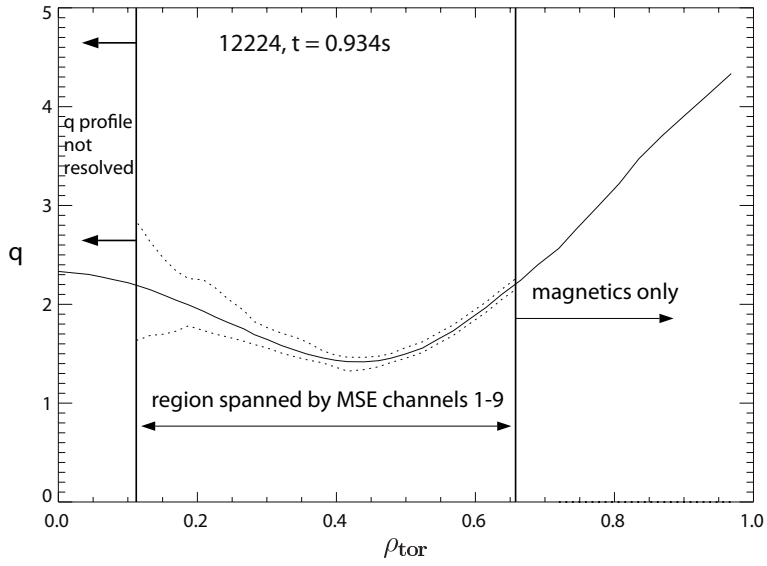

Figure 2.5: An example of a q profile and the interpolated confidence bands: limiter discharge 12224 at 0.934s. The q profile error bars are calculated only in the region spanned by the MSE channels.

The comparison of the results presented, figures 2.3 and 2.5, in this chapter show that the two methods of calculating the q-profile error bars are consistent. Since, these q profile error bars are now an automatically calculated as part of CLISTE , and hence faster, they will be used in the rest of this thesis. Nevertheless, the Monte Carlo method was useful initially as a check for the development of the direct calculations within

CLISTE . Also, the Monte Carlo method is still necessary for approximating the error bars for the $\gamma_{E\times B}$ calculations.

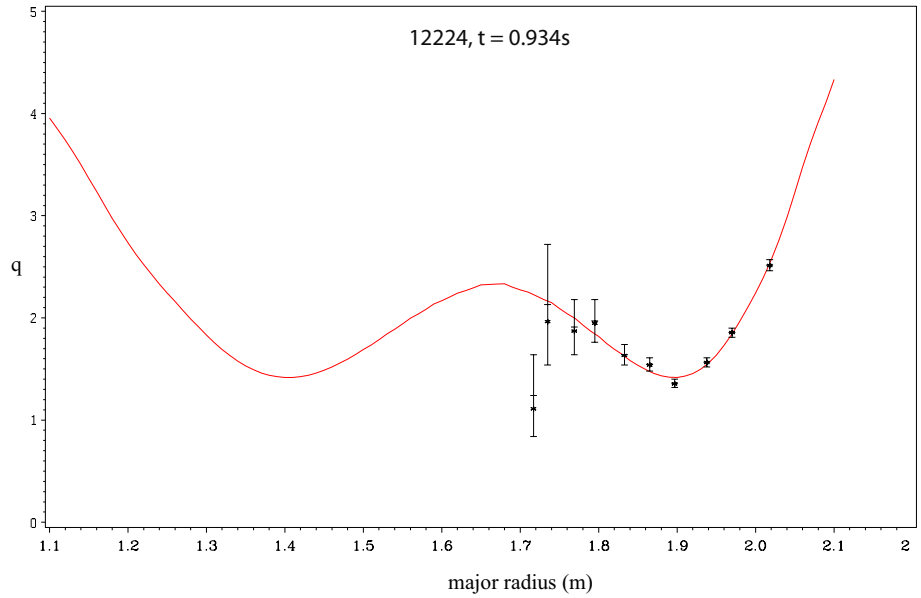

Figure 2.6: The q profile and error bars plotted over the major radius of the plasma: limiter discharge 12224 at 0.934s $I_p \approx 1MA$, $B_t \approx -2.46T$ *and* $n_e \approx 2.8 \times 10^{19} m^{-3}$. *The q profile error bars are calculated only in the region spanned by the MSE channels. The star symbols indicate the experimentally calculated q value.*

Chapter 3

Evolution of the ITB and the q profile

In this chapter the findings of studies into the evolution of the ITB and the relationship between the ITB structure and q profile are presented. Please note that almost all the results presented in this chapter are published in E.D. Quigley *et al.*, Nucl. Fusion 2004 [35]. As discussed in chapter 2 the q profiles and their error estimates were found using CLISTE, constrained with MSE data [31]. Note that the q profile, in figure 3.1, is not plotted inside $\rho_{tor} \approx 0.12$, since the q profile is not accurately recovered within this position due to the omission of the innermost channel. The ITB discharges used in this analysis were run with 1MA plasma current, $I_P = 1MA$, up to 7.5MW neutral beam injection power, $NBI \leq 7.5MW$, at least one discharge had electron cyclotron current drive (ECCD) and the discharges were run with the plasma in an inner limiter or upper single null plasma configuration. The position of the foot and the top (i.e. top of the steep gradient region see figure 3.2(a)) of the barriers were found manually by approximating the best fit to the ion temperature profile data and the errors on these positions were estimated by approximating the worst fit to the data. An example of the ion temperature data and the fit to it can be seen in figure 3.2(a).

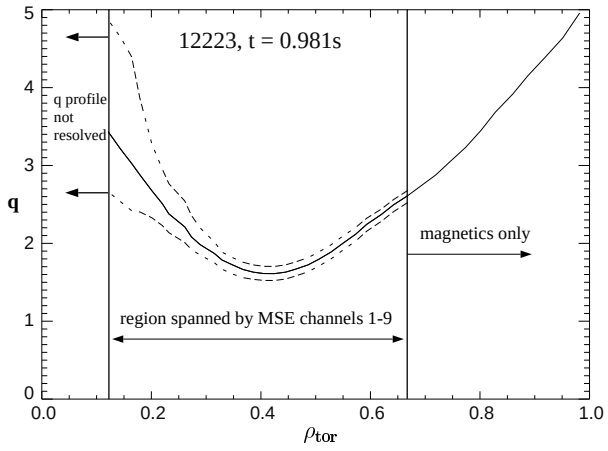

Figure 3.1: An example of a q profile and error bars: limiter discharge 12223 at 0.981s $I_p = 1MA$, $B_t = -2.66T$ *and* $n_e = 2.6 \times 10^{19} m^{-3}$. *The q profile towards the center is not resolved because the innermost MSE channel is not used in the equilibrium. The q profile error bars are calculated only in the region spanned by the MSE channels.*

3.1 Evolution in ITB discharges

Figures 3.3 and 3.4 show the evolution of the ITB foot and position of the q_{min} and $q = 2$ surfaces for discharges 13130 and 12229 respectively. Often, there are two steps in the steep gradient region of the ion temperature, which can be interpreted as a 'staircase' ITB, see figure 3.2. The discharges analyzed here sometimes had two steps and could be characterized as having an inner and an outer foot. These inner and an outer foot positions where present are also plotted in the figures. Sometimes this effect is transitory and in other cases it lasts for the remainder of the ITB phase. One might be tempted to think that these steps in the ion temperature gradient are an artifact of, or due to the noise of, the measurement. However, we would like to point out certain facts that in our opinion make it unlikely that this is true. Firstly, these structures were seen in every ITB discharge analyzed i.e. all seven discharges. Secondly, they are seen to last for more than one time-point see figure 3.2(b) and (c) which shows the steepening of the inner ITB for six time-points and figure 3.3 where the discharge exhibits an inner ITB which lasts for

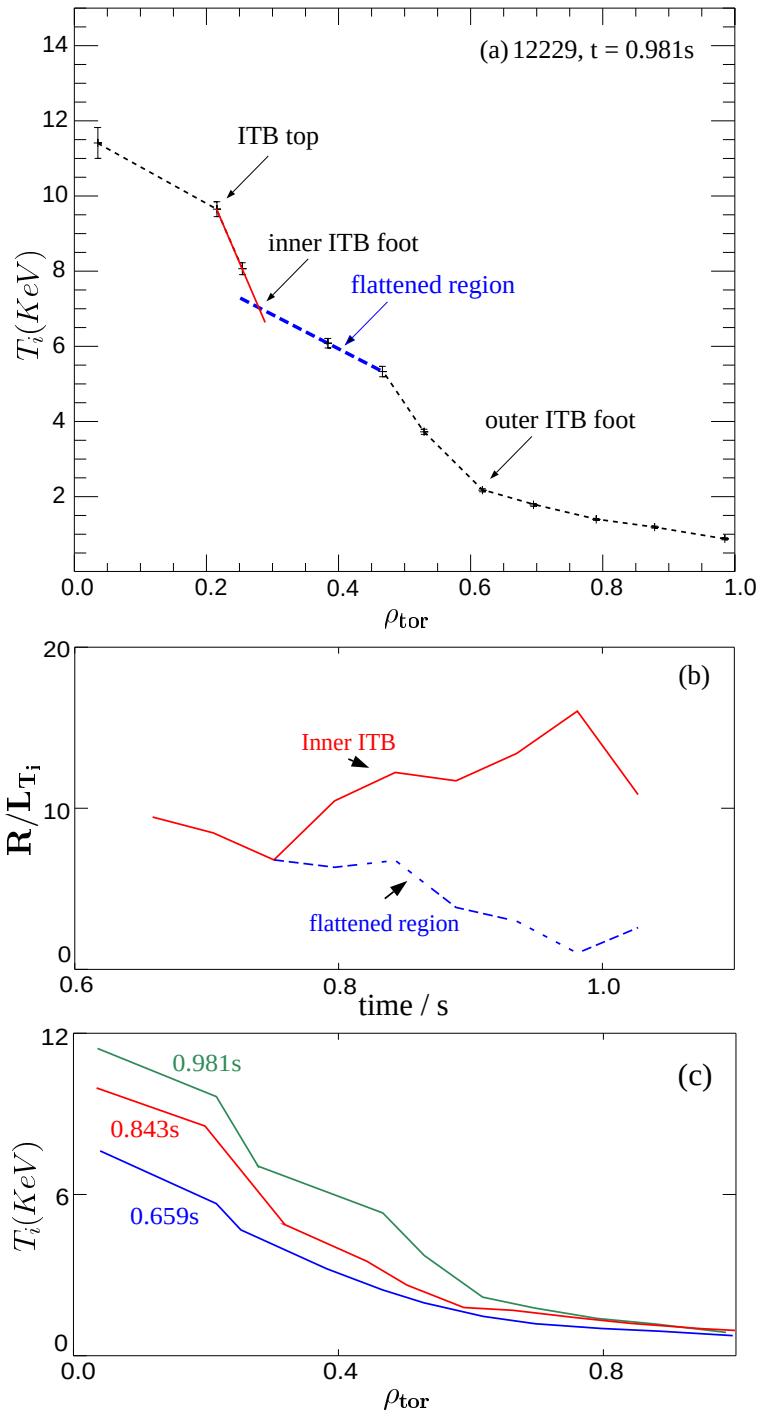

Figure 3.2: (a) T_i profile showing the 'staircase' ITB in discharge 12229 and indicating the positions of the outer and inner ITB foot and the top of the ITB for discharge 12229. (b) The time evolution of the ion temperature gradient length for the same discharge, showing the different gradient lengths of the inner ITB and the flattened region. (c) The ion temperature profiles for discharge 12229 at 0.659s, 0.843s and 0.981s, showing the appearance of the staircase ITB.

at least eight consecutive time-points (i.e. from 0.9s to 1.5s). Thirdly, the second step is seen to come and go during the ITB phase, as can be seen for both discharges, and the steep gradient region is smooth before it appears. Also, their appearance coincides with rational q surfaces entering the plasma, such that they are expected to be connected with MHD activity. It is possible, and in our opinion quite probable, that this structure in the ion temperature is due to a flattening in the profile in the vicinity of a rational surface. This would mean that there is, in fact, only one ITB in which the steep gradient region is simply 'interrupted' by a rational surface. Fourthly, the staircase ITB effect is seen to move between different ion temperature data channels.

ITBs on ASDEX Upgrade usually form with their outer foot inside or very close to the q_{min} position. The ITB outer foot moves radially outward with time and with increased NBI power until it lies at or more often outside the position of q_{min}, it can be positioned as far out as at the outer $q = 2$ surface. In some discharges on ASDEX-Upgrade $\rho_{tor,outerfoot}$ is seen to follow the $q = 2$ surface (figure 3.3) and in others it seems to, more or less, follow $\rho_{tor,q_{min}}$ (figure 3.4).

On the JT60U and JET experiments one step ITBs form with their foot inside or very close to q_{min}[36, 37], while on DIII-D ITBs always form with their foot inside q_{min} [38]. The DIII-D and JT60U experiments report that the ITB foot seems to follow q_{min} and that it can lie slightly outside q_{min}[37, 38, 39]. At JET it has been found that the ITB foot starts inside q_{min} and later moves outside to follow the $q = 2$ surface[36].

During a 'staircase' ITB the outer ITB foot lies outside the position of q_{min}, while the inner ITB foot lies inside. In figure 3.3 the outer foot is seen to follow the outer $q = 2$ surface and the inner foot the inner $q = 2$ surface. In the example in figure 3.4 the outer foot seems to follow q_{min} while the inner ITB foot position first appears around the time and position of the $q = 2$ surface it then disappears and reappears later at a position

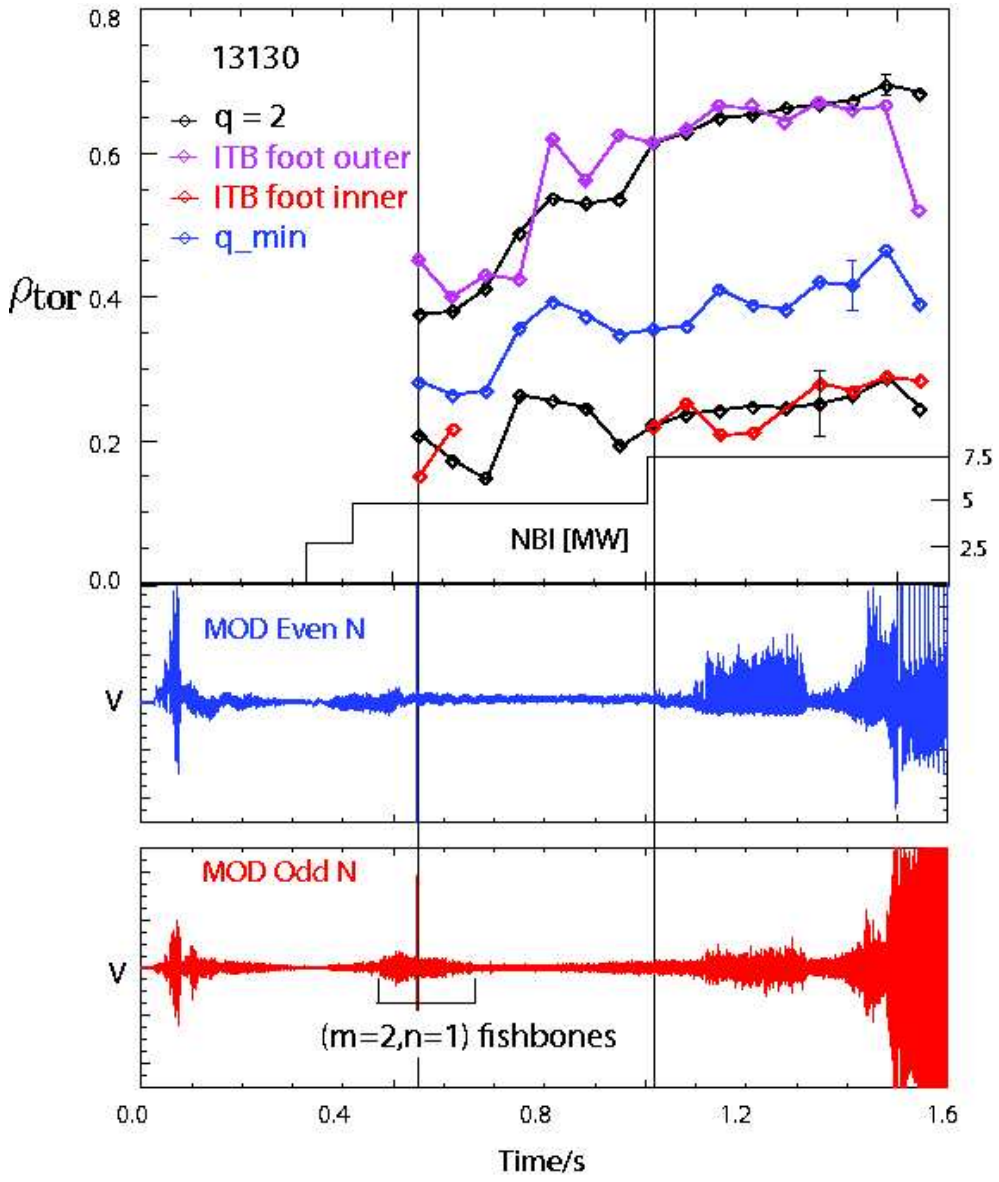

Figure 3.3: Plot of the evolution of the ITB feet, position of q_{min} and $q = 2$ of the 'staircase' ITB discharge 13130. The pink and red lines indicate the outer and inner barrier feet locations, respectively. Blue and black lines indicate the position of q_{min} and $q = 2$, respectively, and vertical lines mark the time-points of the appearance of a second ITB. (Note that the inner ITB appears for a short time at the beginning of the discharge, it then disappears and reappears later in the discharge.)

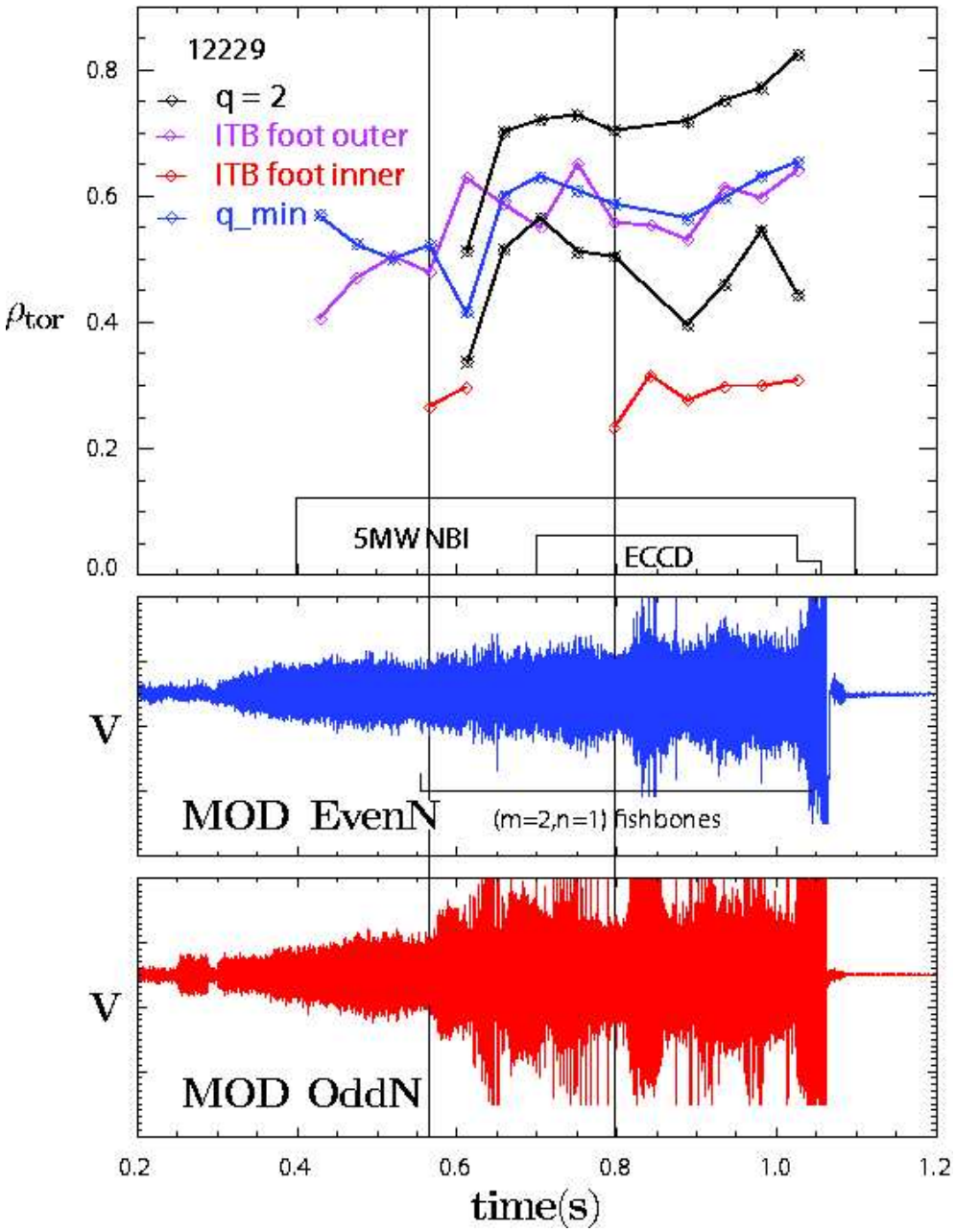

Figure 3.4: Plot of the evolution of the ITB feet, position of q_{min} and $q = 2$ of the 'staircase' ITB discharge 12229. The pink and red lines indicate the outer and inner barrier feet locations, respectively. Blue and black lines indicate the position of q_{min} and $q = 2$, respectively, and vertical lines mark the time-points of the appearance of a second ITB. (Note that the inner ITB appears for a short time at the beginning of the discharge, it then disappears and reappears later in the discharge.)

inside the $q = 2$ surface. The lower parts of the figures 3.3 and 3.4 shows the MHD activity over the duration of the discharges and vertical lines mark the time-points when a second ITB appears, at (or very nearby) all of these time-points MHD activity is apparent. All of the 5 other discharges that were analyzed also exhibited formation of an inner barrier almost always around the time of the appearance of the $q = 2$ surface in the plasma. This and also the fact that the inner foot is sometimes seen to follow the inner $q = 2$ surface indicate that MHD activity is connected with these extra ITBs. 'Staircase' ITBs are also seen on the JET and DIII-D experiments, here steps in the ITB seem to be triggered by the occurrence of a $q = 2$ surface, on JET the inner and outer foot also follow the position of the inner and outer $q = 2$ surface respectively[36]. On DIII-D 'staircase' ITBs were formed in a discharge with a monotonic q profile and only the inner ITB foot is located at the $q = 2$ surface[40]. Note that the formation of a second step in the steep gradient region causes, the ITB region to become broader and, the gradient length to become smaller, both of which are requirements for advanced tokamak operation[39].

Figure 3.4 also shows quite clearly that narrow (i.e. ITB outer foot located close to the plasma center) ITBs on ASDEX-Upgrade can form before the $q = 2$ surface appears in the plasma (also seen on DIII-D [40]) and before fishbones are seen in the discharge. Results from JET indicate that $q = 2$ can act as a trigger for ITB formation [36]. In contrast, on JT60-U the $q = 3$ surface has been identified as a possible trigger for ITB formation[41]. The T-10 and RTP experiments have also reported ITB triggering by rational q surfaces[42, 43]. However the T-10 and RTP experiments report ITBs in the electron temperature channel, thus, caution should be taken when making comparisons with the ITBs presented here.

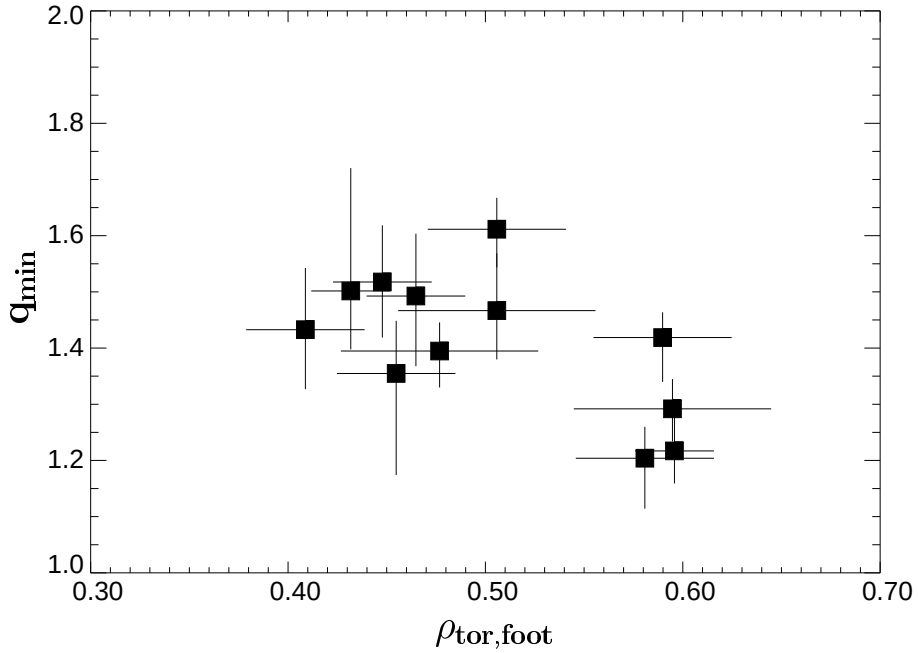

Figure 3.5: Normalized toroidal flux radius of the barrier foot plotted against the minimum value of q at a time-point when ITBs are well developed.

3.2 Positioning of well developed ITBs

Here, the position of the foot and top of the barrier are compared with the q and shear profiles, at a time when the ITB is well developed. The error bars on the q profile, shear and the position were approximated using the same method described at the beginning of this chapter.

On comparison of the position of the foot of the barrier with q_{min} see figure 3.5, we find the value of that q_{min} at the position of the foot of the barrier is between 1.1 and 1.7, i.e. $1.1 \leq q_{min} \leq 1.7$. It is also seen that the most extended barriers seem to have lower values of q_{min}. However, all of the most extended ITBs are at later time-points, which is in agreement with DIII-D and JT-60U results [44] which found that ITBs propagate outward with time. Therefore it can not be determined what leads to the barrier extending outward: the value of q_{min} or the longer time.

Figures 3.6 and 3.7 show that it is not necessary for strong ITBs on ASDEX Upgrade

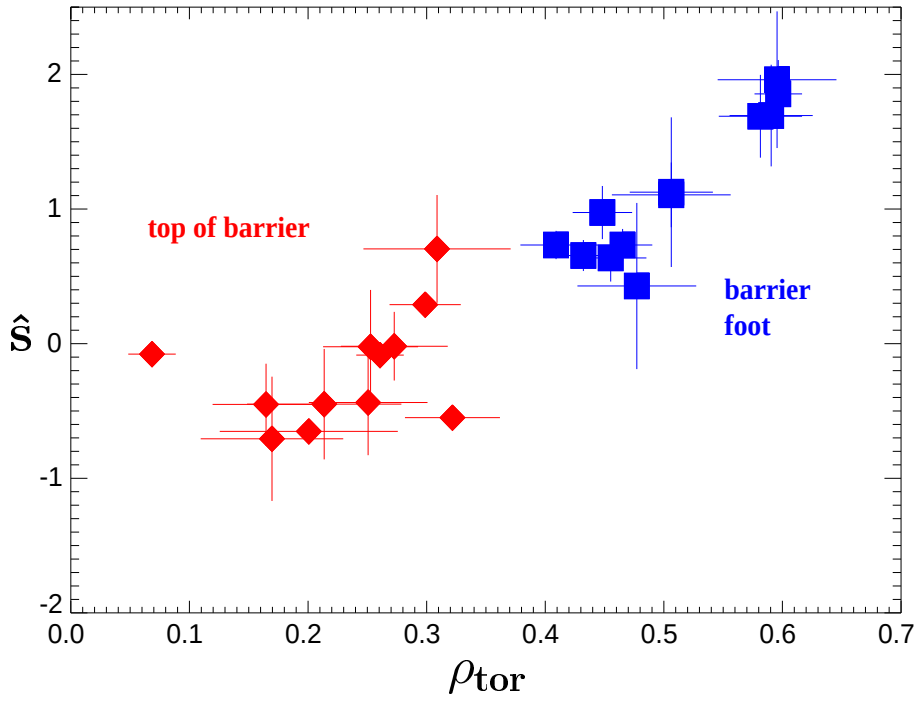

Figure 3.6: Comparison of $\rho_{tor,foot}$ and $\rho_{tor,top}$ with $\hat{s}$ for ITB discharges at a time-point when ITBs are well developed.

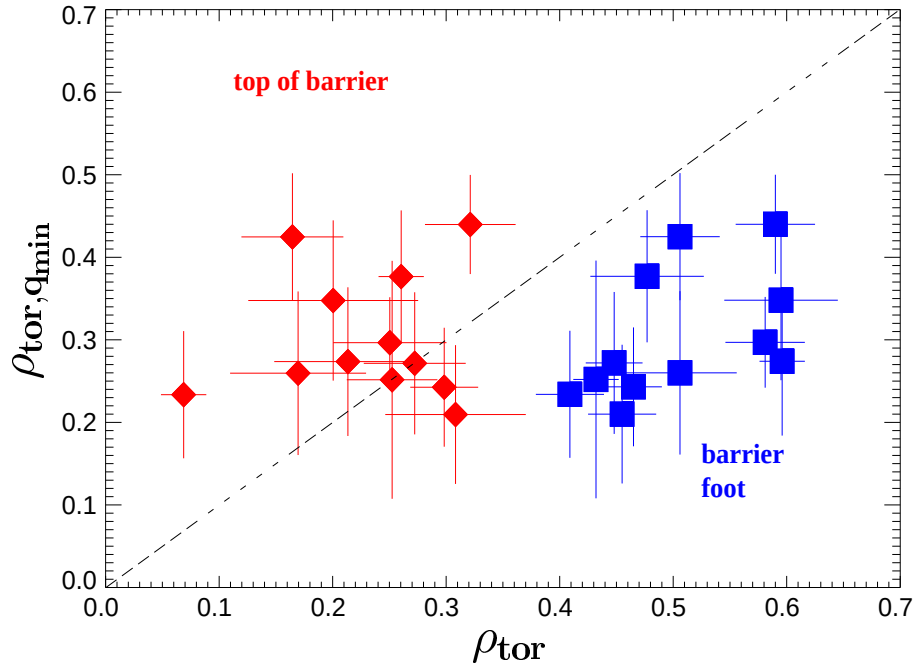

Figure 3.7: Comparison of $\rho_{tor,foot}$ and $\rho_{tor,top}$ with $\rho_{tor,q_{min}}$ for ITB discharges at a time-point when ITBs are well developed. The dashed line indicates $\rho_{tor} = \rho_{tor,q_{min}}$.

to always straddle the $\hat{s} = 0$ position. In the steepest ITB discharges the steep gradient region lies entirely in the positive shear region. The other discharges straddle the $\hat{s} = 0$ and thus encompass part of the negative shear region and some of the positive shear region up to $\hat{s} \approx 2$. These are generally broader ITBs, this broadness seems to be caused by there being more than one step in the ITB region. The shear and the position of the barrier foot are seen to be linearly related, i.e. the broader the barrier the higher the shear at the foot (and vice versa). This is reflected in the plot in figure 3.6 which shows that all of the ITBs are located with their foot at a larger radial position than q_{min}. On the DIII-D experiment it has also been found that ITBs are not limited to the negative shear region [44]. Although with low power (5MW) the ITB is confined to the core of the plasma, with increased power (7.5MW) it can move farther out into the positive shear region [45]. Research at JET also shows that ITBs can develop that encompass both the negative and positive shear regions, but that shear is always less than 1 inside the barrier [46].

3.3 Discussions

The results presented in this chapter show that the sustainment of the barrier is not related to negative shear, because barriers are found to occur at positions at which the shear is positive. The formation of an ITB, however, does seem to require heating during the current ramp up phase, which indicates that negative shear could still play a role in the formation of the barrier.

Narrow ITBs form, before the occurrence of fishbones and the $q = 2$ surface, with their foot inside or very close to the position of q_{min}. 'Staircase' ITBs have been seen on ASDEX-Upgrade and are expected to be connected with MHD activity. Sometimes the positions of these second barriers are seen to follow the $q = 2$ surface, such that they are not inconsistent with a flattening in the ion temperature profile in the vicinity of a rational surface. The position of the ITB seems, to some extent, to be controlled by the q profile i.e. broader barriers have broader positions of q_{min}. Since ITBs normally position themselves at or very close to q_{min} it has been hypothesized that $\hat{s} = 0$ may have a stabilizing effect on turbulence. However, we have seen that very steep gradient ITBs can lie outside the position of q_{min}, in the positive shear region (sometimes outside $\hat{s} = 1$), thus, it is likely that this hypothesis is not valid and that ITBs are not limited by the $\hat{s} = 0$ position.

Chapter 4

ITB formation criteria

In this chapter the results of analysis of various possible ITB formation criteria are presented. Please note that almost all the results presented in this chapter are published in E.D. Quigley *et al.*, Nucl. Fusion 2004 [35]. ITBs on ASDEX Upgrade are produced by applying neutral beam injection (NBI) in the current ramp up phase, see a typical ITB scenario in figure 4.1. This produces a hollow current density and a non-monotonic q profile. While a detailed study into the power threshold for ITB formation has thus far not been undertaken at ASDEX Upgrade, it should be noted that ITBs are not seen to form in discharges with less than 5MW NBI in the ramp up phase. With only neutral beam heating ITBs are seen mainly in the ion temperature channel, and generally not in the electron temperature or density channels. The fact that no electron ITBs were seen is related to the low heat flux in the electron channel, however, it cannot be claimed that this is well understood since the electron transport remains anomalous. All ITB discharges found and examined here had negative magnetic shear or a very flat q profile. Please note, a strong ITB is defined here as one where the normalized inverse ion temperature gradient length is greater than 10, i.e. $R/L_{Ti} > 10$. This definition is motivated by the fact that for standard (non-ITB) discharges $R/L_{Ti} \approx 5 - 6$.

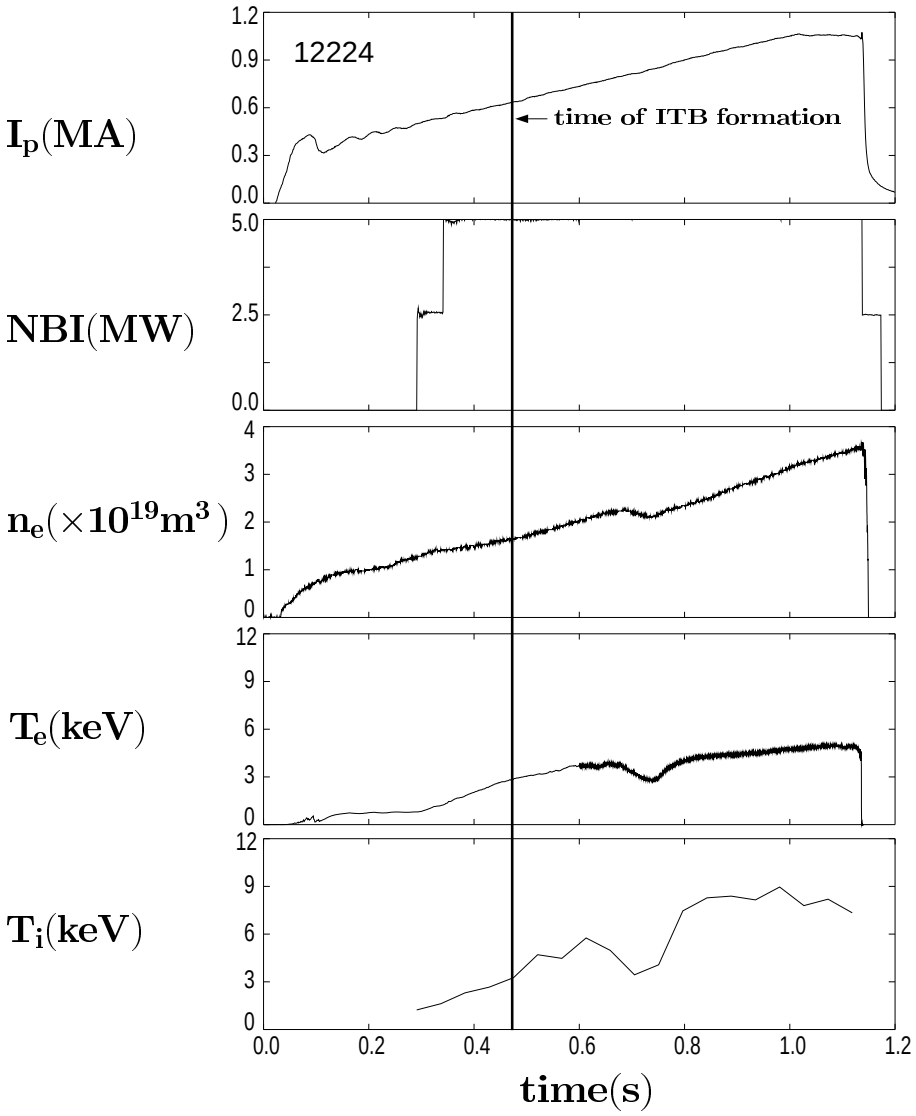

Figure 4.1: Typical time evolution of ASDEX Upgrade parameters for the discharges used for the global formation criteria analysis showing the plasma current, heating power, line averaged density, electron and ion temperature (both temperature measurements were taken at $\rho_{tor} \approx 0.22$*).*

4.1 Global formation criteria

Correlations between ITB formation and plasma parameters, just before formation, have been investigated, by making comparisons between discharges, with the same ramp-up scenario, which did or did not develop an ITB. The ITB discharges chosen were those of the 1999 campaign, in which approximately 5MW of NBI power was switched on at around 0.3s, while I_p was ramped up at a rate of approximately $1\text{MA}s^{-1}$ up to a maximum of 0.8MA or 1MA, see figure 4.1, with the plasma in an inner limiter or upper single null plasma configuration. The inner limiter or upper single null plasma configuration keeps the plasma in L-mode, which is necessary for ITB formation and sustainment. This original ITB scenario was unreliable for the production of ITBs and one aim of this work was to identify an experimental setup which would allow ITBs to be reproducibly generated.

It was found that barriers form only at low line averaged density, between $1.5 \times 10^{19} m^{-3}$ and $2.3 \times 10^{19} m^{-3}$. From figure 4.2(a) it can be seen that in the time interval where the ITBs typically form, approximately 0.4s-0.5s, the line averaged density for the ITB discharges is lower than for the non-ITB discharges. It seems that for the non-ITB discharges when conditions would otherwise facilitate ITB formation, the line averaged density is too high and thus an ITB does not form. This hypothesis is supported by evidence from the 2002 campaign ITB discharges, in both upper and lower single null plasmas, where heating during the current ramp was delayed until 0.7 seconds (see figure 4.2(b)). This delayed heating prevents the neutral beam fueling from generating higher density before ITB formation. Here, very reproducible strong ITBs are seen to form very soon after the NBI power is switched on, at around 0.71 seconds, when other conditions are favorable for ITB formation and the line averaged plasma density is even lower than that of the ITB discharges from the 1999 campaign. (Note, the line averaged density increases more rapidly in the 2002 discharges after the NBI is switched on because the NBI power is higher than in the 1999 discharges.) Theory predicts that

the power threshold for ITB formation should scale with density [11] and experimental results show that this threshold is very sensitive to changes in density [47, 48, 49]. Also in the 1999 campaign, a clear correlation of barrier formation with the time since boronization was found, with barriers forming only in discharges just after boronization. This is expected to be linked to the need for lower density since just after boronization the density is generally low. No clear correlation with ECE radiation temperature, gas puff, radiation power or internal inductance could be established.

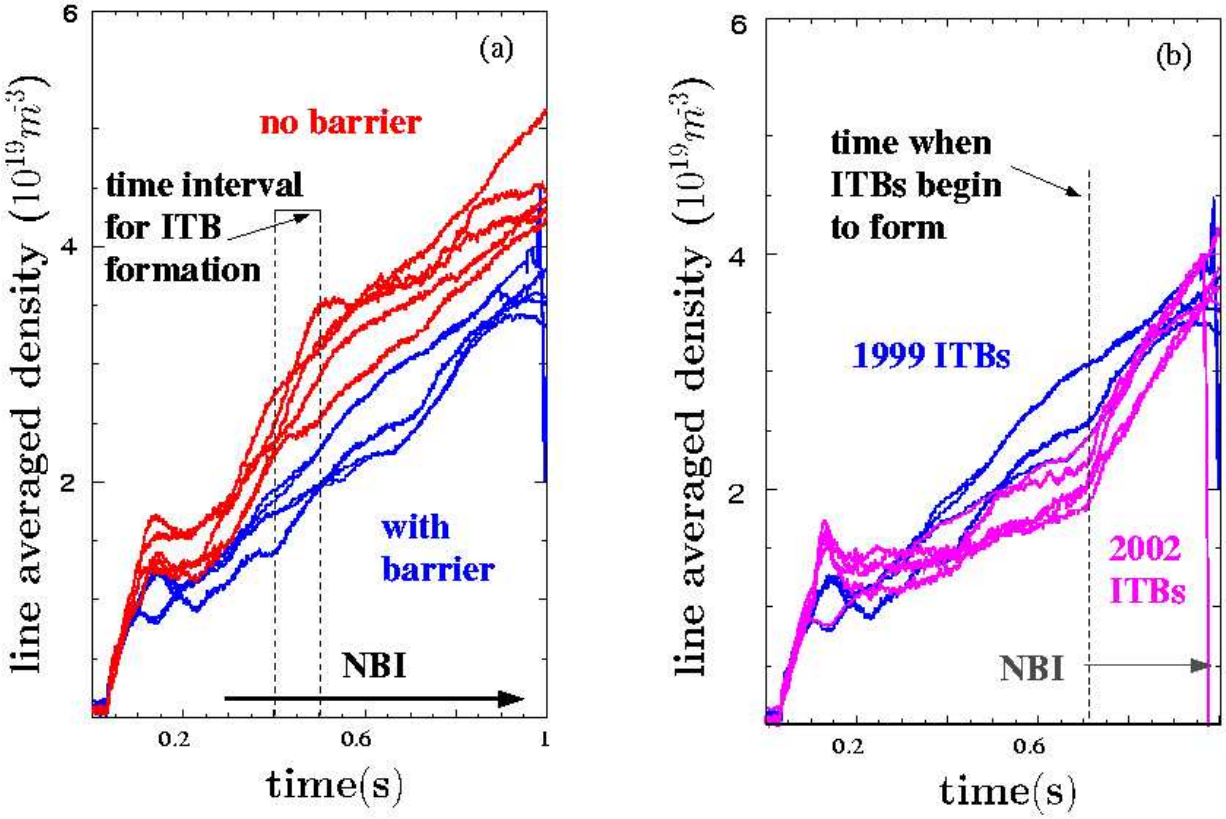

Figure 4.2: Comparison of line averaged density evolution for (a) ITB (in blue) and non-ITB (in red) discharges (also the ITB discharges shown here were run very soon after boronization, while the non-ITB discharges were not) and (b) 1999 ITB discharges (in blue) and 2002 ITB discharges (in pink).

4.2 Investigation of possible turbulence suppression mechanisms

Anomalous transport is thought to be caused by plasma turbulence[50]. Reduction of this transport to approximately neoclassical levels during ITB events is generally believed to be due to the suppression of this turbulence. Turbulence is driven by the free energy sources of a large number of micro-instabilities[51, 52] essentially initiated by the temperature and density gradients[9]. In particular, ion temperature gradient (ITG) turbulence and its suppression is thought to be an important factor for ITB formation, see also chapter figure 1 for a more detailed description of the ITG mode. ITG modes are stabilized by a steep density gradient[9, 53, 54] and by $E \times B$ shear [55], and are known to depend on magnetic shear, ion to electron temperature ratio T_i/T_e, impurity concentration in the plasma, and the Shafranov shift of the magnetic axis[11]. The variation in magnetic shear and the ratio T_i/T_e is similar in ITB and non-ITB discharges before ITB formation and, although stabilizing, alone they are not sufficient for ITB formation.

A possible explanation, for the requirement of lower density for ITB formation (mentioned in section 2) is that by slightly lowering the density and keeping the input power and torque the same, the toroidal velocity and consequently the $E \times B$ shear will increase possibly allowing the turbulence to be suppressed. However, no evidence was found of the toroidal velocity being higher for ITB discharges.

4.2.1 The density gradient

The density gradients for the target ITB and target non-ITB discharges, taken before the switch on of the NBI power, are shown in figure 4.3, and it can be seen that the target ITB discharges as a whole have a steeper normalized density gradient than the target non-ITB discharges.

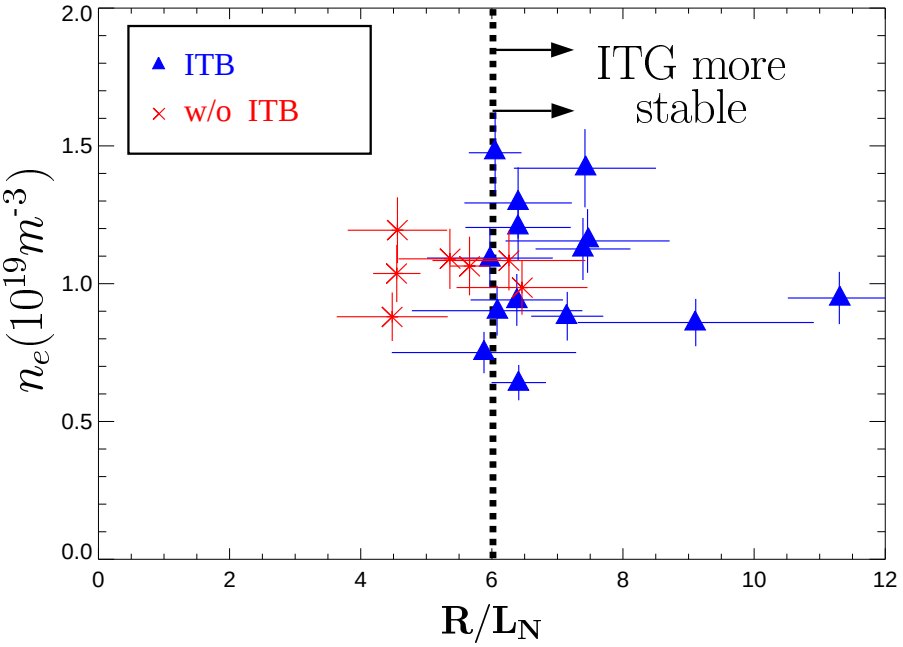

Figure 4.3: Comparison of the local inverse density gradient length R/L_N and the density, evaluated just before the NBI is switched on and at approximately $\rho_{tor} = 0.4$, for ITB (triangles) and non-ITB (stars) discharges.

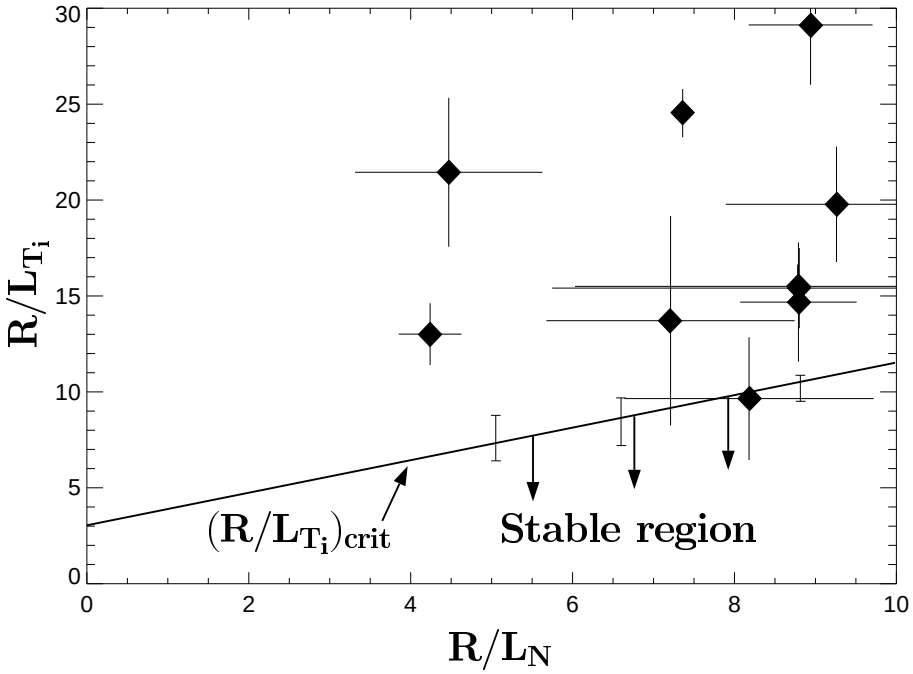

Figure 4.4: Plot of R/L_N against R/L_{T_i}, for ITB discharges evaluated when the ITB is strongest and at approximately $\rho_{tor} = 0.4$, showing ITG stable region.

Figure 4.4 shows the critical ITG boundary, for the ITB discharges, with respect to the electron density gradient, which was calculated using the gyro-kinetic linear stability code GS2 [56] [57] in the steep gradient region of the ITB, with the values of $T_i/T_e = 1.8$, $\hat{s} = -0.2$ and $q = 1.8$ fixed for all the discharges. It also shows values of the density gradient length plotted against the ion temperature gradient length calculated at the time when the ITB is strongest, approximately 400 ms after the time shown in figure 4.3. Theory predicts that if the condition $R/L_T \leq (R/L_T)_{crit}$ is fulfilled, then the ITG modes are stable. From the plot it can be seen that only few discharges lie close to this boundary, indicating that the modes may be stable in these discharges. However, in the majority of the discharges the modes are not sufficiently stabilized by the density gradient. Thus these results (figures 4.3 & 4.4) show that the density gradient may play some role in the early stages of the discharge to facilitate ITB formation.

In conclusion, the line averaged density is clearly a control parameter for barrier formation. Although this may be partly explained by the local density gradient, it is clear that the latter is not very important for barrier formation. It therefore remains unclear why the line averaged density plays such an important role.

4.2.2 The $E \times B$ shear and the Shafranov shift

The generally accepted condition for turbulence suppression due to $E \times B$ shear is when the shearing rate, $\gamma_{E\times B}$, is of the order of or greater than the maximum linear growth rate, γ_{max}, $\gamma_{E\times B} \geq \gamma_{max}$[24]. $\gamma_{E\times B}$ was calculated for these discharges using the equation[25]

$$\gamma_{E\times B} = \frac{(RB_p)^2}{B}\frac{\partial}{\partial\psi}\left[\frac{E_r}{RB_p}\right],$$

where R is the major radius, B_p is the poloidal magnetic field, B is the total magnetic field and E_r is the radial electric field. Unfortunately, this criterion is not exact and it has been found that there can be up to a factor of 2.5 deviation from it[11][26]. Figure

4.5(a) shows $\gamma_{E\times B}$ and γ_{max} for calculations without the Shafranov shift and figure 4.5(b) with the Shafranov shift. γ_{max} was calculated using the GS2 code in $\hat{s}-\alpha$ equilibrium. The error bars on $\gamma_{E\times B}$ were calculated using a Monte Carlo technique. This method involved adding noise to the MSE data (a maximum error of 0.2 degrees) and the toroidal rotational velocity information (an average error of 20% was assumed) 100 times. Then the CLISTE equilibrium code[31] was run using these 100 files and the $\gamma_{E\times B}$ results were averaged to get the mean and standard deviation. This process was repeated for each of the ITB discharges studied in this thesis. The radial electric field was also calculated using CLISTE, neglecting the poloidal rotation. Previous measurements on ASDEX Upgrade[18] have shown that the poloidal rotation, within the error bars, is of the same order of magnitude as the neoclassical contribution and that its contribution to the electric field is much smaller than that of the toroidal rotation. Although the magnetic shear and electron to ion temperature ratio are known to have a stabilizing effect on the ITG instability, it must be noted that a fully developed ITB has its steepest normalized temperature gradient in the region of small shear (as discussed in section 4.1) and has $T_e/T_i \approx 0.75$. Therefore, the effect of these stabilizing mechanisms is small for a fully developed barrier, although this may not necessarily be true for ITB formation. Comparison of the plots show that the inclusion of the Shafranov shift in the calculations reduces γ_{max} considerably, and it can be concluded that it is an important stabilizing mechanism for these discharges. Also from figure 4.5(b) we can see that some discharges (at least 4) still have unstable modes (i.e. where γ_{max} is approximately four times greater than $\gamma_{E\times B}$). This indicates that something is missing in the explanation of the barrier formation. In view of previous results it is unlikely that a poloidal rotation can be the cause of the discrepancy[18]. Since the points that have a much larger growth than shearing rate are almost all very narrow barriers, it is possible that the growth rate is overestimated in the ballooning transform due to the strong variation of the drift frequency over the extent of the mode. Another explanation could be that the neglect of the geometry effects from the γ_{max} calculations, in the GS2 code using the $\hat{s}-\alpha$ model, has caused the γ_{max} values to be incorrectly calculated. It is also possible that

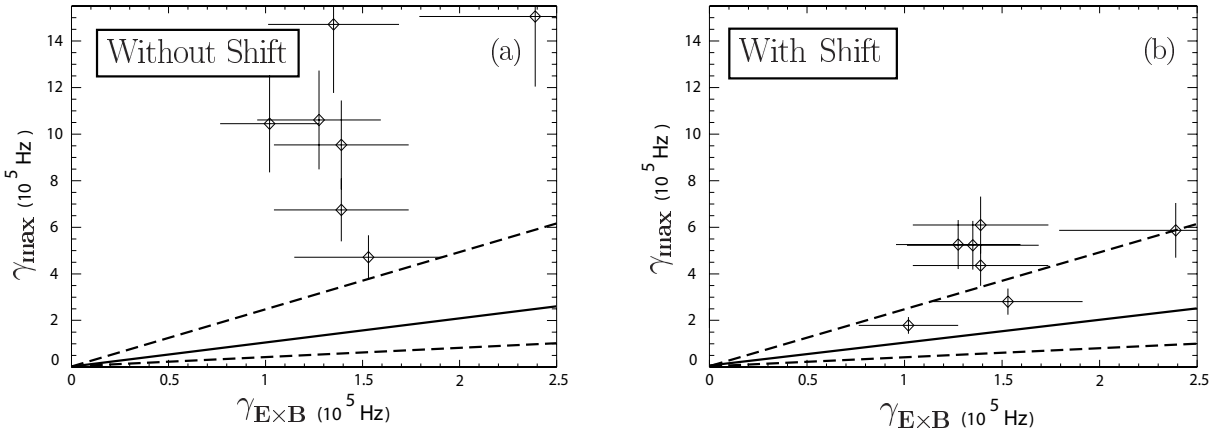

Figure 4.5: Comparison of $\gamma_{E\times B}$ with γ_{max}, for ITB discharges at time when ITB is strongest, for (a) calculations without the Shafranov shift and (b) with the Shafranov shift, line indicates $\gamma_{E\times B} = \gamma_{max}$, dashed lines indicate the factor of 2.5 deviation from this criterion.

the generally accepted model of $E \times B$ shear suppressing the turbulence during an ITB event is incomplete.

4.3 Discussions

It has been found that ITBs at ASDEX Upgrade form only at low density, possibly due to a steeper normalized density gradient. This was further illustrated by ITB discharges in the 2002 campaign where the density was kept low and strong ITBs were reliably produced.

The Shafranov shift has been identified as a relatively important stabilizing mechanism. Also, the results presented here indicate that $E \times B$ shear is not sufficient to explain the suppression of the turbulence in all ITB discharges. This could be due to the neglect of the poloidal rotation, however if this were the case it would be necessary for the contribution of the poloidal rotation to the $E \times B$ shear to be much larger than that of the toroidal rotation. Since other studies have found the poloidal rotation to be much smaller, it is highly improbable that including the contribution of the poloidal rotation in the calculations would increase the $E \times B$ shear sufficiently, this possibility is further

investigated in chapter 6. It is more likely that this is due either, to the inadequacies of the $\hat{s} - \alpha$ model for studying ITBs, or the incompleteness of the $E \times B$ shear paradigm. In next chapter (chapter 5) the dependencies of the $\hat{s} - \alpha$ model are tested.

Chapter 5

ITG mode stability

In this chapter the accuracy of the simplified circular $\hat{s} - \alpha$ model is examined (the $\hat{s} - \alpha$ model was used in the final calculations of the previous chapter, see figure 4.5). This is achieved by comparing the calculations with those of the more complete Miller model, which uses the shaped geometry in the calculations. Firstly, the effect of plasma shaping is examined in the Miller model in order to determine the dependence of the ITG stability on the plasma shape. Then, the effect of the density gradient, the electron temperature gradient, the Shafranov shift parameter and the inverse aspect ratio are compared between the two models.

The gyro-kinetic linear stability code, GS2[56] [57], is used for the purposes of this study. The GS2 code is based on the electromagnetic linearized gyro-kinetic equation, including an appropriate term to account for collisions, along with the quasi-neutrality condition and Ampère's law.

The examination involved scanning each plasma shaping parameter individually using the GS2 code to calculate the maximum linear growth rate of the mode. In this way the dependence of the stability of the mode on the shaping parameters can be ascertained. This was done for two different ITG cases, the simple ITG case and the experimental

ITB case (i.e. using the experimental settings of ITB discharge 12223). In order to compare the $\hat{s}-\alpha$ and Miller models, the relationship between the α in the $\hat{s}-\alpha$ model and the first derivative of the Shafranov shift, Δ', in the Miller equilibrium must be derived.

Note that the growth rate of a mode, γ is a measure of how quickly the amplitude of the mode grows, the slower the amplitude grows the more stable the plasma is. The maximum linear growth rate, γ_{max}, is the growth rate of the most unstable mode. Note also that γ_{max} can be naturally normalized to v_t/R, where v_t is the thermal velocity. All plots in this chapter, with the exception of figure 5.16, show the normalized γ_{max} values.

5.1 The derivation of the Shafranov shift

Here the outward shift of the magnetic surfaces will be calculated, this is described by the force balance equation (2.4), and is called the Shafranov shift, Δ. In order to do this some simplifications will be made. As in chapter 2 the calculations will be done using a plasma of circular cross-section. It is also assumed that the inverse aspect ratio is small $\epsilon = r/R \ll 1$, since the Shafranov shift is of the order of ϵ^2 this means that it is also small. Using these assumptions the perturbation of the surfaces with respect to concentric circles is small and the equations can be solved iteratively through an expansion in ϵ.

As shown in chapter 2 the Grad-Shafranov equation, in cylindrical co-ordinates, is given by

$$-\Delta^*\Psi = -\frac{\partial^2\Psi}{\partial R^2} - \frac{\partial^2\Psi}{\partial z^2} + \frac{1}{R}\frac{\partial\Psi}{\partial R} = \mu_0 R^2\, p'(\Psi) + FF'(\Psi). \tag{5.1}$$

Thus, one starts by making the following transformation

$$R = R_0 + r\cos\theta,$$
$$z = r\sin\theta$$

This transformation is similar to the one from Cartesian to circular surfaces. Although (R, z) are part of a cylindrical coordinate system, they are Cartesian in the poloidal plane. Two terms of equation (5.1) are the Laplacian operator in a 2-D Cartesian coordinate system, which has a well known form in polar coordinates

$$\nabla^2 = \frac{\partial^2}{\partial R^2} + \frac{\partial^2}{\partial z^2} = \frac{1}{r}\frac{\partial}{\partial r}\left[r\frac{\partial}{\partial r}\right] + \frac{1}{r^2}\frac{\partial^2}{\partial \theta^2}. \tag{5.2}$$

The last term of equation (5.1) can also be rewritten as

$$\frac{\partial \Psi}{\partial R} = \frac{\partial r}{\partial R}\frac{\partial \Psi}{\partial r} + \frac{\partial \theta}{\partial R}\frac{\partial \Psi}{\partial \theta} = \cos\theta\frac{\partial \Psi}{\partial r} - \frac{\sin\theta}{r}\frac{\partial \Psi}{\partial \theta}. \tag{5.3}$$

Substituting equations (5.2) and (5.3) into the Grad Shafranov equation one finds

$$\frac{1}{r}\frac{\partial}{\partial r}\left[r\frac{\partial \Psi}{\partial r}\right] + \frac{1}{r^2}\frac{\partial^2 \Psi}{\partial \theta^2} - \frac{\cos\theta}{R}\frac{\partial \Psi}{\partial r} + \frac{\sin\theta}{rR}\frac{\partial \Psi}{\partial \theta} = -\frac{\partial}{\partial \Psi}\left(\frac{F^2}{2}\right) - \mu_0 R^2\frac{\partial p}{\partial \Psi}. \tag{5.4}$$

If one now multiplies equation (5.4) across by r^2, one has

$$r\frac{\partial}{\partial r}\left[r\frac{\partial \Psi}{\partial r}\right] + \frac{\partial^2 \Psi}{\partial \theta^2} - \epsilon r\cos\theta\frac{\partial \Psi}{\partial r} + \epsilon\sin\theta\frac{\partial \Psi}{\partial \theta} = -r^2\frac{\partial}{\partial \Psi}\left(\frac{F^2}{2}\right) - \mu_0 r^2 {R_0}^2\frac{\partial p}{\partial \Psi}. \tag{5.5}$$

The smallness of ϵ can now be used to order the terms in equation (5.5), since $r \ll R$. Discarding terms in ϵ and dividing across once more by r^2, the lowest order is given by

$$\frac{1}{r}\frac{\partial}{\partial r}\left[r\frac{\partial \Psi_0}{\partial r}\right] + \frac{1}{r^2}\frac{\partial^2 \Psi_0}{\partial \theta^2} = -\frac{\partial}{\partial \Psi_0}\left(\frac{F^2}{2}\right) - \mu_0 {R_0}^2\frac{\partial p}{\partial \Psi_0}. \tag{5.6}$$

Here, Ψ_0 is the lowest order poloidal flux. The next order can be calculated using the following equation for the total poloidal flux

$$\Psi = \Psi_0(r) + \Psi_1(r, \theta)....,$$

where $\Psi_1/\Psi_0 = O(\epsilon)$. If one substitutes this into the Grad Shafranov equation and keeps all the terms of order ϵ, one finds

$$\begin{aligned}\frac{1}{r}\frac{\partial}{\partial r}\left[r\frac{\partial \Psi_1}{\partial r}\right] + \frac{1}{r^2}\frac{\partial^2 \Psi_1}{\partial \theta^2} - \frac{\cos\theta}{R}\frac{\partial \Psi_0}{\partial r} + \frac{\sin\theta}{rR}\frac{\partial \Psi_0}{\partial \theta} = \\ -\frac{\partial}{\partial \Psi}\left(\frac{F^2}{2}\right) + \frac{\partial}{\partial \Psi_0}\left(\frac{F^2}{2}\right) - \mu_0 R^2\left(\frac{\partial p}{\partial \Psi} - \frac{\partial p}{\partial \Psi_0}\right) - 2\mu_0 R_0 r\cos\theta\frac{\partial p}{\partial \Psi_0}.\end{aligned} \tag{5.7}$$

Now, for any quantity $G = G(\Psi)$, with the approximation $\Psi = \Psi_0 + \Psi_1$, one has

$$\begin{aligned}\frac{\partial G}{\partial \Psi_0}(\Psi) &= \frac{dG}{d\Psi}(\Psi)\,\frac{\partial \Psi}{\partial \Psi_0} \\ &= \frac{dG}{d\Psi}(\Psi).\end{aligned}$$

Such that a first order Taylor expansion of $\frac{dG}{d\Psi}(\Psi)$ about Ψ_0 in the small parameter Ψ_1 yields

$$\begin{aligned}\frac{dG}{d\Psi}(\Psi) &= \frac{\partial G}{\partial \Psi_0}(\Psi_0 + \Psi_1) \\ &= \frac{\partial G}{\partial \Psi_0}(\Psi_0) + \frac{\partial^2 G}{\partial \Psi_0^2}(\Psi_0)\,\Psi_1.\end{aligned}$$

Using this and the fact that $\Psi_0 = \Psi_0(r)$ equation (5.7) becomes

$$\frac{1}{r}\frac{\partial}{\partial r}\left[r\frac{\partial \Psi_1}{\partial r}\right] + \frac{1}{r^2}\frac{\partial^2 \Psi_1}{\partial \theta^2} - \frac{\cos\theta}{R}\frac{\partial \Psi_0}{\partial r} = -\Psi_1 \frac{\partial^2}{\partial \Psi_0^2}\left[\frac{F^2}{2} + \mu_0 R_0^2 p\right] - 2\mu_0 R_0 r\cos\theta\frac{\partial p}{\partial \Psi_0}. \quad (5.8)$$

If one now substitutes

$$\Psi_1 = \psi_1(r)\cos\theta,$$

all the terms in equation (5.8) become proportional to $\cos\theta$ and one can divide across the equation to get

$$\frac{1}{r}\frac{\partial}{\partial r}\left[r\frac{\partial \psi_1}{\partial r}\right] - \frac{\psi_1}{r^2} + \psi_1\frac{\partial^2}{\partial \Psi_0^2}\left[\frac{F^2}{2} + \mu_0 R_0^2 p\right] = \frac{1}{R_0}\frac{\partial \Psi_0}{\partial r} - 2\mu_0 R_0 r\frac{\partial p}{\partial \Psi_0}. \quad (5.9)$$

The left-hand side of equation (5.9) can be further simplified if one uses the lowest order equilibrium given in equation (5.6), such that

$$\frac{\partial^2}{\partial \Psi_0^2}\left[\frac{F^2}{2} + \mu_0 R_0^2 p\right] = -\frac{\partial}{\partial \Psi_0}\left[\frac{1}{r}\frac{\partial}{\partial r}(r\frac{\partial \Psi_0}{\partial r})\right] = -\frac{1}{B_\theta}\frac{\partial}{\partial r}\left[\frac{1}{r}\frac{\partial}{\partial r}(RC_\theta)\right].$$

Using this equation the first order equation can be rewritten in the form

$$B_\theta\frac{\partial}{\partial r}\left[r\frac{\partial \psi_1}{\partial r}\right] - \frac{B_\theta \psi_1}{r} - r\psi_1\frac{\partial}{\partial r}\left[\frac{1}{r}\frac{\partial}{\partial r}(rB_\theta)\right] = rB_\theta^2 - 2\mu_0 r^2\frac{\partial p}{\partial r}. \quad (5.10)$$

The left hand side of equation (5.10) can also be written in the following form

$$\frac{\partial}{\partial r}\left[rB_\theta{}^2\frac{\partial}{\partial r}(\frac{\psi_1}{B_\theta})\right] = rB_\theta{}^2 - 2\mu_0 r^2\frac{\partial p}{\partial r}, \tag{5.11}$$

where the subscript 0 has been dropped from the zeroth-order quantities, a derivation of this equation is also given in ref. [58]. If the flux surface Ψ is displaced by a distance $\Delta(\Psi_0(r))$, Ψ can be written as [7]

$$\begin{aligned}\Psi &= \Psi_0 + \Psi_1 \\ &= \Psi_0 - \Delta(r)\frac{\partial \Psi_0}{\partial R}.\end{aligned} \tag{5.12}$$

One can derive an expression for the Shafranov shift, Δ, using equation (5.12).

$$\begin{aligned}\Delta(r) &= \frac{-\Psi_1}{\Psi_0{}'} \\ &= \frac{-\Psi_1}{R_0 B_\theta}.\end{aligned} \tag{5.13}$$

Where the definition of the flux function given in equation (2.6c) has been used to give $\partial\Psi_0/\partial r = R_0 B_\theta$. The derivative of the Shafranov shift is given by

$$\Delta' = \frac{\partial \Delta}{\partial r} = -\frac{1}{R_0}\frac{\partial}{\partial r}(\frac{\psi_1}{B_\theta}). \tag{5.14}$$

Rearranging equation (5.11) one has

$$\frac{\partial}{\partial r}(\frac{\psi_1}{B_\theta}) = \frac{1}{rB_\theta{}^2}\int_0^r \left(yB_\theta{}^2(y) - 2\mu_0 y^2\frac{\partial p}{\partial y}\right)\, dy. \tag{5.15}$$

Substituting this into equation (5.14) gives a solution for the derivative of the Shafranov shift.

$$\Delta' = \frac{\partial \Delta}{\partial r} = -\frac{1}{R_0 rB_\theta{}^2}\int_0^r \left(yB_\theta{}^2(y) - 2\mu_0 y^2\frac{\partial p}{\partial y}\right)\, dy. \tag{5.16}$$

The local internal inductance, $l_i(r)$, and poloidal beta, $\beta_p(r)$, are defined by the following relations:

$$l_i(r) = \frac{2}{r^2 B_\theta{}^2}\int_0^r yB_\theta{}^2(y)\, dy, \tag{5.17}$$

$$\beta_p(r) = -\frac{1}{r^2 B_\theta{}^2}\int_0^r 2\mu_0 y^2\frac{\partial p}{\partial y}\, dy. \tag{5.18}$$

Thus, using equations (5.17) and (5.18), equation (5.16) can be re-written as [59]

$$\Delta' = -\frac{r}{R_0}\left[\frac{1}{2}l_i(r) + \beta_p(r)\right]. \tag{5.19}$$

The $\hat{s} - \alpha$ equilibrium is based on a 1979 paper presented by B.Coppi [60]. In this paper the displaced circular magnetic surfaces approximation is used and a simplified relationship between Δ' and α is derived. Here, the relationship is derived in a slightly different manner, in keeping with the derivation thus far.

When a large aspect ratio and a constant toroidal field, B_ϕ, are assumed and the variation of R is neglected, $R \cong R_0$. Also, here it is assumed that the shear is small, $\hat{s} \ll 2$, and hence the q is taken to be approximately constant. The poloidal field is given by $B_\theta = rB_\phi/R_0 q$, substituting in to equation 5.17 gives

$$li(r) = \frac{1}{2}. \tag{5.20}$$

Close to the axis the pressure profile can be approximated by

$$p(r) = p_0\left(1 - cr^2\right), \tag{5.21}$$

where p_0 is the pressure at the axis and c is a constant. Using equation 5.21, $p'(y)$ can be calculated as

$$p'(y) = p'(r)\frac{y}{r} \tag{5.22}$$

Substituting into equation 5.18 one has

$$\beta_p(r) \simeq -2\mu_0 \frac{R_0^2 q^2}{r^5 {B_\phi}^2}\frac{dp}{dr}\int_0^r y^3\, dy \tag{5.23}$$

$$\simeq -\frac{1}{2}\mu_0 \frac{R_0^2 q^2}{r {B_\phi}^2}\frac{dp}{dr}. \tag{5.24}$$

Now, substituting equations 5.23 and 5.20 into equation 5.19, one finds

$$\Delta' = -\frac{\epsilon}{4} + \frac{1}{2}\mu_0 \frac{R_0 q^2}{{B_\phi}^2}\frac{dp}{dr}. \tag{5.25}$$

Thus, the first term scales with epsilon and can be neglected, such that Δ' can be approximated by

$$\Delta' \simeq \frac{1}{2}\mu_0 \frac{R_0 q^2}{{B_\phi}^2} \frac{dp}{dr}. \tag{5.26}$$

The measure of the pressure gradient, α, can be given by

$$\alpha = -2\mu_0 \frac{R_0 q^2}{B_\phi^2} \frac{dp}{dr}. \tag{5.27}$$

Such that

$$\Delta' \simeq -\frac{\alpha}{4}. \tag{5.28}$$

5.2 The $\hat{s} - \alpha$ equilibrium

The $\hat{s} - \alpha$ magnetohydrodynamic (MHD) equilibrium model was first proposed by Connor, Hastie and Taylor in 1978 [61] as a simplification for testing their method for determining plasma stability. The equilibrium represents a large-aspect-ratio tokamak with displaced circular flux surfaces. The basic equations are given by [60]

$$R = R_0 + \Delta(r) + r\cos\theta,$$
$$z = r\sin\theta.$$

The magnetic field is uniform over the magnetic surfaces but the shear is non-uniform. Thus, the effects of plasma shaping on the stability of the plasma are neglected as is the effect of the finite aspect ratio.

5.3 The Miller equilibrium

The Miller equilibrium is a generalization of the circular $\hat{s} - \alpha$ local equilibrium to finite aspect ratio, elongation, κ, and triangularity, δ [59]. The shape of the flux surface is given by

$$R = R_0 + r\cos\left[\theta + \arcsin(\delta)\sin(\theta)\right],$$
$$z = \kappa r\sin(\theta).$$

Also, the effects of the Shafranov shift are included. The model is particularly suited for studying localized stability such as those carried out using the ballooning mode representation of the gyro-kinetic equations. Thus, the effects of the plasma shaping on the growth rate of the modes can be analyzed. Also, a comparison of the stability predicted by the $\hat{s} - \alpha$ model can be made. The comparisons are made for two different

cases, firstly the case of the simple ITG and secondly the experimental ITB case in which the settings of a experimental ITB discharge, 12223, are used. The settings of the two cases are described in the next sections.

5.4 The dependencies of a simple ITG

In the simple ITG case only the ion temperature gradient is non-zero, i.e. $\nabla T_e = \nabla n_e = \nabla n_i = 0$, see table 5.1, this is done so that all modes other than the ITG mode are suppressed in the calculations. In this way one can be sure that the calculated maximum growth rate relates only to the ITG mode and is not effected by other types of instabilities. This allows the dependencies of the ITG mode to be analyzed. The dependencies are analyzed by running 2-D scans of the parameter of interest (e.g. elongation or triangularity) and R/L_{T_i} using the gyro-kinetic linear stability code, GS2. R/L_{T_i} is scanned because it is the main drive of the mode.

Model	R/L_N	R/L_{T_e}	α/Δ'	T_e/T_i	$\hat{s}$	q	Z_{eff}	κ	$\frac{d\kappa}{d\rho}$	δ	$\frac{d\delta}{d\rho}$	ϵ
$\hat{s}-\alpha$	0	0	0	1	1	1.5	1	-	-	-	-	0.1
Miller	0	0	0	1	1	1.5	1	1	0	0	0	0.1

Table 5.1: Table of the basic $\hat{s}-\alpha$ and Miller settings of the simple ITG. Note that, unless otherwise stated, these settings are only changed in the calculations when a parameter is being scanned.

5.4.1 The effect of the triangularity

The triangularity, δ, has been scanned between 0 and 1 and the normalized ion temperature gradient length, R/L_{T_i}, between 2 and 11.6. Using the GS2 code the maximum linear growth rates of the mode, γ_{max}, were calculated. The results are shown

in figure 5.1 γ_{max} increases with δ until $\delta = 0.2$, it then decreases. The maximum proportional decrease in γ_{max}, which is when $R/L_{T_i} = 6.8$, is small, approx. 15% (from $\delta = 0.2$ to $\delta = 1$). Note that the figure shows the normalized γ_{max} values. Here γ_{max} is normalized by dividing by v_t/R, where $v_t = \sqrt{\frac{T_i}{m_i}}$ is the thermal ion velocity and $m_i \approx 3.34 \times 10^{-27} kg$ is the ion mass. If one assumes $T_i = 3KeV$ for the simple ITG case, then the normalization factor is $v_t/R \approx 2.3 \times 10^5$. Thus, this normalization factor is a constant for the simple ITG settings.

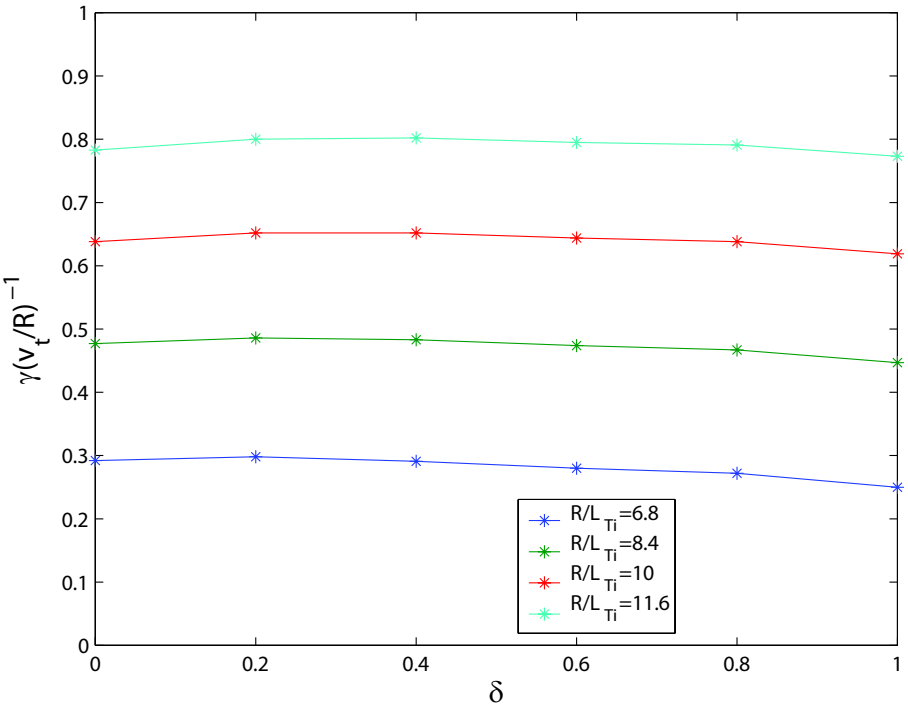

Figure 5.1: The relationship between δ and γ_{max}, for different values of R/L_{T_i}, for the simplified ITG calculated with the Miller equilibrium. Note that the growth rate is normalized with respect to the v_t/R, where v_t is the thermal ion velocity. If one assumes $T_i = 3KeV$, then the normalization factor is $v_t/R \approx 2.3 \times 10^5$.

In the scans, for each value of δ a R/L_{T_i} scan was performed and γ_{max} was calculated. When these results are plotted, i.e. R/L_{T_i} versus γ_{max} see figure 5.2, it can be seen that there is an almost linear relationship between R/L_{T_i} versus γ_{max}. Thus, if one then extrapolates the fit through the points down to the $\gamma_{max} = 0$ axis one arrives at a

particular value of R/L_{T_i}. This value of R/L_{T_i} is known as the critical value, $R/L_{T_i(crit)}$, below which the mode is stable. The ITG mode is driven by R/L_{T_i}, however there is a threshold in R/L_{T_i} below which the the mode is not active, i.e. $\gamma_{max} \leq 0$, this threshold corresponds to $R/L_{T_i(crit)}$ see chapter 1.6. Figure 5.3 shows the dependence of the critical ion temperature gradient length, below which the modes are not active, on the triangularity. From the plot it can seen that $R/L_{T_i(crit)}$ has only a small dependency on the triangularity.

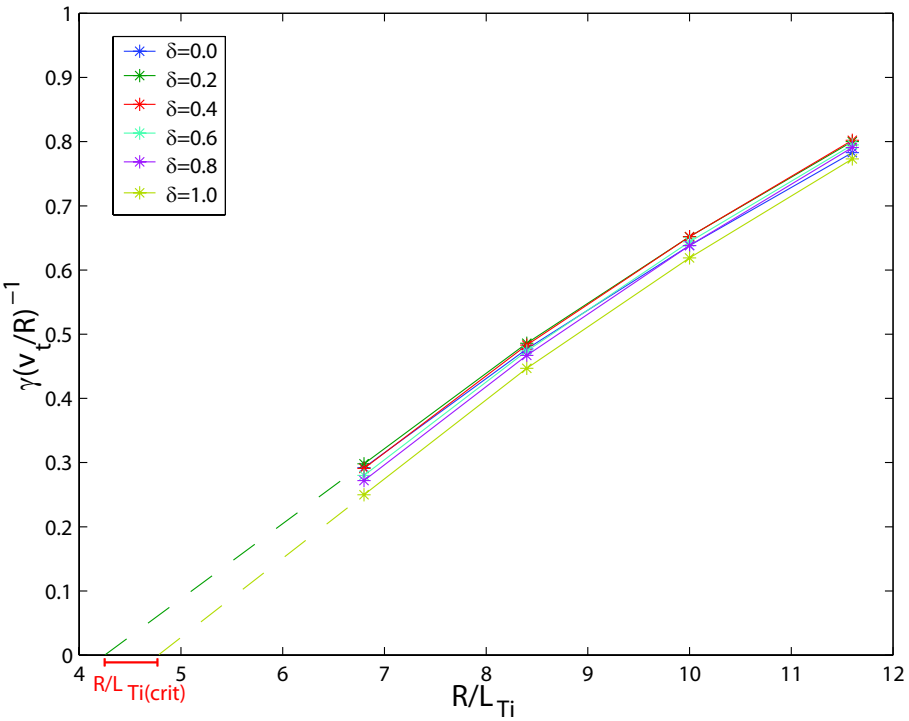

Figure 5.2: The relationship between R/L_{T_i} and γ_{max}, for different values of δ, for the simplified ITG calculated with the Miller equilibrium. The plot also shows an example of how the fit can be extrapolated down to the $\gamma_{max} = 0$ axis in order to calculate the $R/L_{T_i(crit)}$ values.

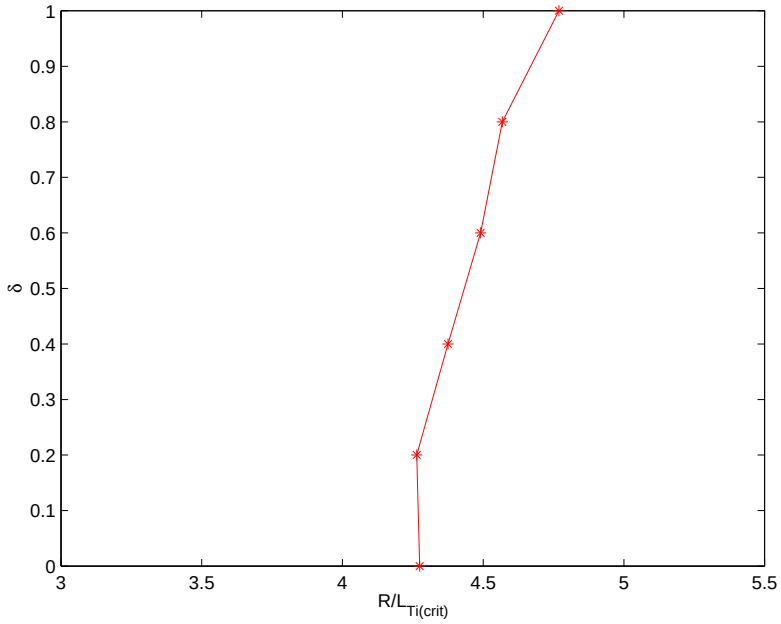

Figure 5.3: The relationship between $R/L_{T_i(crit)}$ and δ, for the simplified ITG calculated with the Miller equilibrium.

Thus, it can be concluded that the neglect of the triangularity from the calculations in the $\hat{s} - \alpha$ model is justified, since it makes only a moderate difference to the results.

The effect of the gradient in triangularity ($d\delta/d\rho$) was also investigated, in the model. During these scans the triangularity was set to the experimental value of 0.025 (12223), which was calculated in the GS2 interface. Then $d\delta/d\rho$ was scanned between 0 and 0.025. A limited number of scans were done and the results indicate that $d\delta/d\rho$ has more or less no effect on γ_{max}. Hence, it was considered unnecessary to include these results here.

5.4.2 The effect of the elongation (κ)

The elongation has been scanned between 1 and 2 and R/L_{T_i} between 2 and 11.6. The results for these scans are displayed in figures 5.4 and 5.5. In figure 5.4 one can see that γ_{max} decreases with κ. The maximum fractional change is at $R/L_{T_i} = 6.8$ where γ_{max} decreases by approximately 40%, between $\kappa = 1$ and $\kappa = 2$. These results illustrate the stabilizing effect of the elongation on the ITG mode. Since this effect is neglected in the $\hat{s} - \alpha$ model calculations, the maximum linear growth rate of the modes could be overestimated by up to 40%, as figure 5.4 shows. Figure 5.5 illustrates the dependence of $R/L_{T_i(crit)}$ on κ. The critical gradient, at which the modes become unstable, is higher for larger values of κ. Overall $R/L_{T_i(crit)}$ increases by a factor of approximately 1.2.

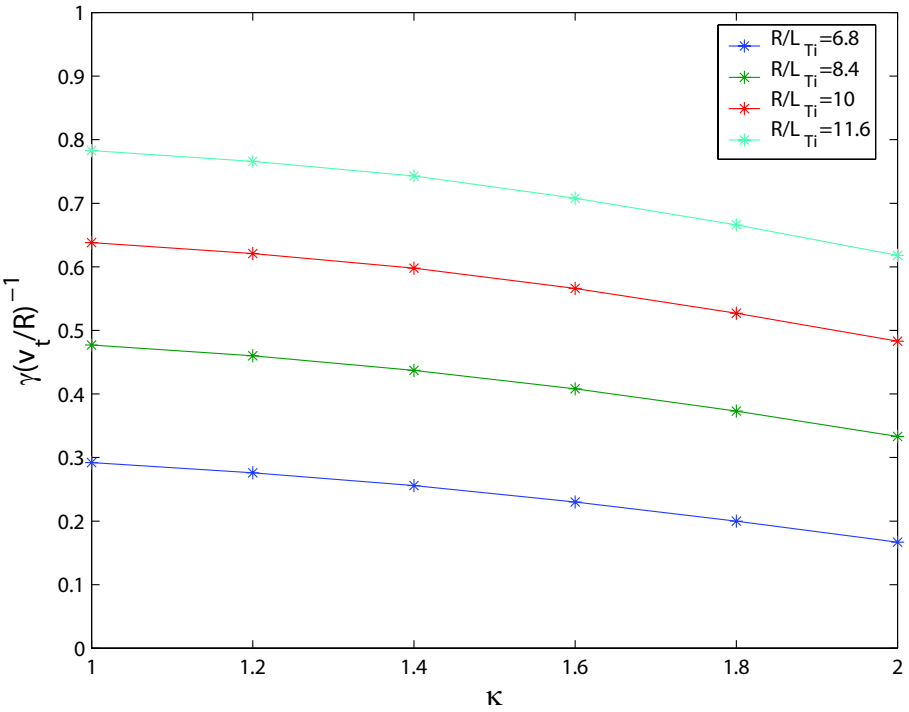

Figure 5.4: The relationship between κ and γ_{max}, for different values of R/L_{T_i}, for the simplified ITG.

A scan of the gradient of the elongation with respect to the minor radius was also done. During these scans the elongation was set to 1.395, $d\kappa/d\rho$ was scanned between 0 and 1 and R/L_{T_i} between 2 and 11.6. The results displayed in figures 5.6 and 5.7 show

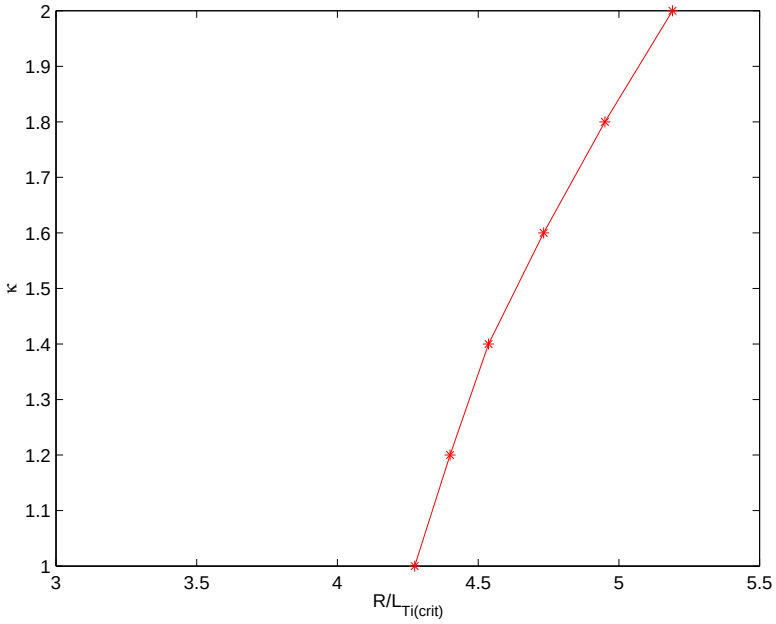

Figure 5.5: The relationship between κ and $R/L_{T_i(crit)}$, for the simplified ITG calculated with the Miller equilibrium.

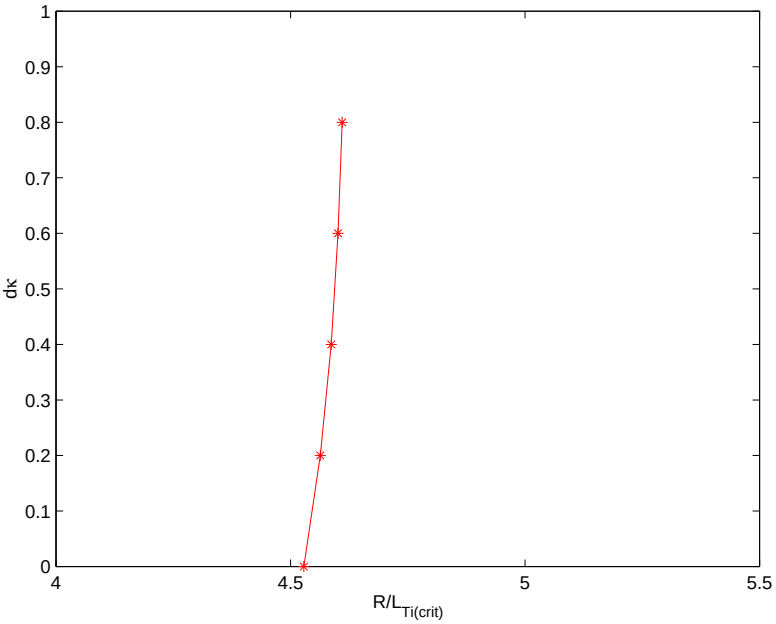

Figure 5.6: The relationship between $R/L_{T_i(crit)}$ and $\frac{d\kappa}{d\rho}$ in the simple ITG case.

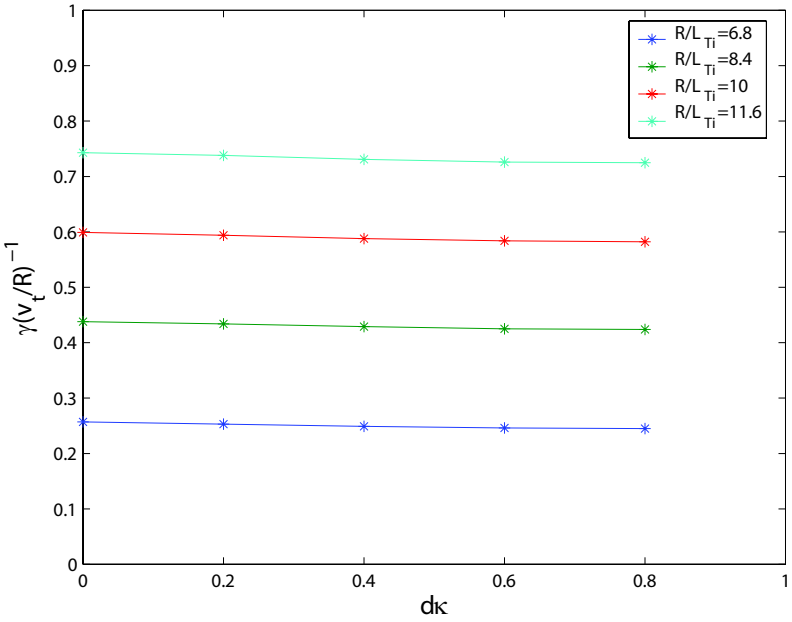

Figure 5.7: The relationship between $d\kappa$ and γ_{max} for the simplified ITG.

that the increase in $d\kappa/d\rho$ causes at most a 5% decrease in γ_{max}, thus the stabilizing effect of $d\kappa/d\rho$ is small and it can be concluded that it is unimportant in the calculations.

5.4.3 The effect of the inverse aspect ratio (ϵ).

In order to study the effect of the inverse aspect ratio in the two models a circular plasma was used in the calculations done with the Miller equilibrium, i.e. $\kappa = 1$ and $\delta = 0$. In this way the effect of ϵ alone can be ascertained. A 2-D scan of both ϵ and R/L_{T_i} was performed. The inverse aspect ratio was scanned from 0.02 to 0.3 and the normalized ion temperature gradient length between 2 and 11.6. The results are presented in figures 5.8, 5.9 and 5.10. It can be seen that the growth rate of the modes increase with larger inverse aspect ratio, see figure 5.8 for both the Miller, shown in full lines, and $\hat{s} - \alpha$, shown in dashed lines, models. The maximum linear growth rate is seen to increase by as much as a factor of 2.5 in some cases, between $\epsilon = 0.02$ and $\epsilon = 0.244$ for the Miller model. In the calculations using the $\hat{s} - \alpha$ model the increase is

much slower than for the Miller equilibrium. The overall increase in γ_{max}, in the $\hat{s}-\alpha$ model, is approximately 70% less than that calculated with the Miller equilibrium, in most cases. One can also see from figure 5.8 that the Miller model approaches the $\hat{s}-\alpha$ one in the limit of very low ϵ. This plot shows nicely the relationship between the $\hat{s}-\alpha$ and Miller models. As mentioned before the Miller model is simply the $\hat{s}-\alpha$ model generalized to finite aspect ratio (large ϵ), elongation and triangularity. When the Miller calculations are done with a circular plasma and small ϵ then the results agree with the $\hat{s}-\alpha$ results, as expected. Thus, the results presented here clearly show that the $\hat{s}-\alpha$ model underestimates the contribution of the inverse aspect ratio to the growth rate of the ITG mode. The γ_{max} calculated by using the Miller equilibrium can be up to nearly two times larger than that calculated by the $\hat{s}-\alpha$ model, at the same value of ϵ and R/L_{T_i}.

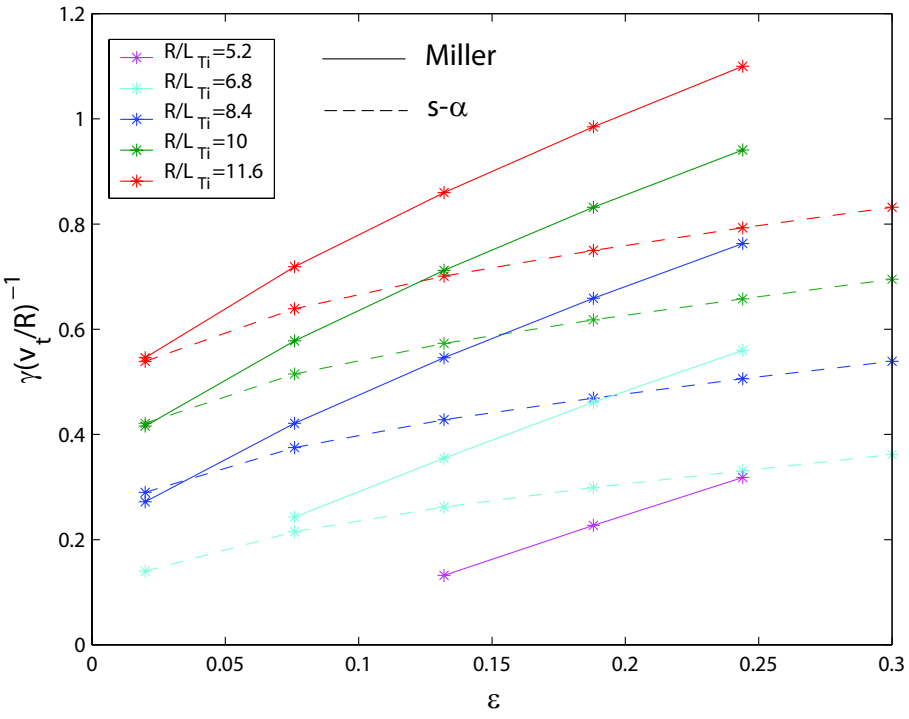

Figure 5.8: Comparison of the γ_{max} dependence on ϵ for the $\hat{s}-\alpha$ and Miller equilibria. The solid lines represents the Miller model results and the dashed lines represent the $\hat{s}-\alpha$ model results.

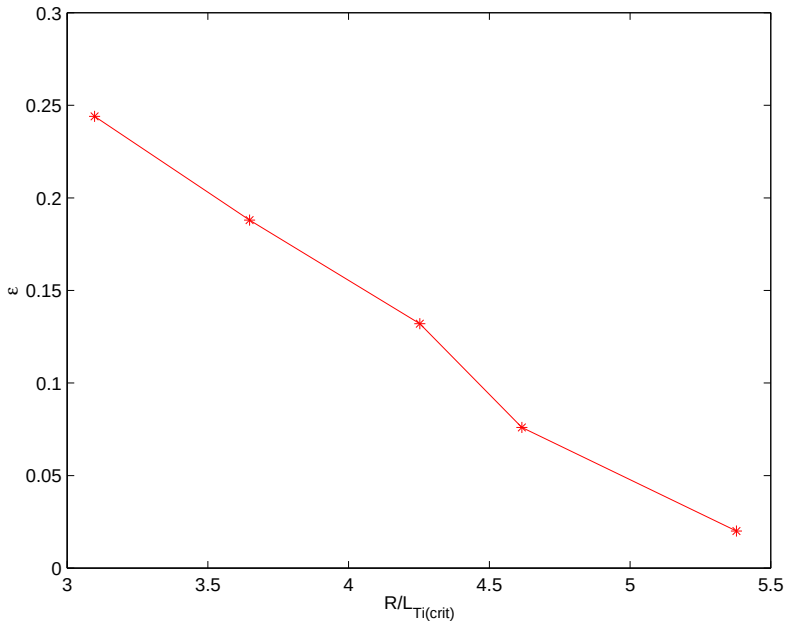

Figure 5.9: The relationship between $R/L_{T_i(crit)}$ and ϵ, for the simplified ITG with the Miller equilibrium.

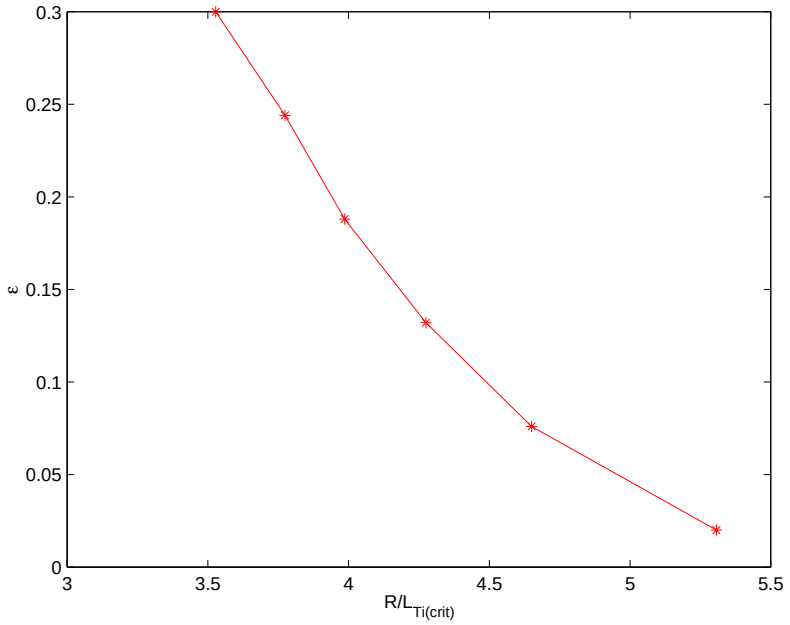

Figure 5.10: The relationship between $R/L_{T_i(crit)}$ and ϵ, for the simplified ITG in $\hat{s} - \alpha$ equilibrium.

Figure 5.9 shows the relationship between ϵ and $R/L_{T_i(crit)}$ in the Miller equilibrium. The critical normalized gradient in the ion temperature below which the mode is stable decreases with larger inverse aspect ratio, that is they are inversely and almost linearly related. $R/L_{T_i(crit)}$ decreases by approximately a factor of 1.8 between $\epsilon = 0.02$ and $\epsilon = 0.244$. Figure 5.10 exhibits the ϵ dependence of $R/L_{T_i(crit)}$ for the $\hat{s} - \alpha$ model. The decrease in $R/L_{T_i(crit)}$ is approximately a factor of 1.5 between $\epsilon = 0.02$ and $\epsilon = 0.244$. At $\epsilon = 0.244$ the Miller model predicts $R/L_{T_i(crit)} \approx 3.1$ and the $\hat{s} - \alpha$ model predicts $R/L_{T_i(crit)} \approx 3.75$. Thus, if one assumes that the Miller model gives the more accurate results, it can be concluded that the $\hat{s} - \alpha$ model can overestimate the critical ion temperature gradient by approximately 20% at high ϵ.

The results presented thus far in this chapter show that the main influences included in the Miller equilibrium are the elongation and the inverse aspect ratio. Since, in the case of the simple ITG mode, increasing the elongation from 1 to 2, in the Miller model, can decrease γ_{max} by approximately 40% and in contrast using $\epsilon = 0.244$, in the Miller model, increase γ_{max} by approximately 70% more than that predicted by the $\hat{s} - \alpha$ model at the same settings (as figure 5.8 shows). One would, therefore, expect that the use of a shaped plasma and a finite aspect ratio in the form of the Miller model would result a net increase in γ_{max} relative to that calculated in the $\hat{s} - \alpha$ model. This is further discussed for the experimental ITB case in section 5.5.1.

5.4.4 The effect of the Shafranov shift parameters.

The effect of the Shafranov shift related parameters on the stability of the ITG mode was also examined. Scans of α and Δ' were done using the settings of the simple ITG case described above and the effect in the $\hat{s} - \alpha$ and Miller equilibria were compared. In the Miller equilibrium scans a simplified case of a circular plasma cross-section was used, i.e. $\kappa = 1$ and $\delta = 0$. Note that two different values of ϵ were used in these

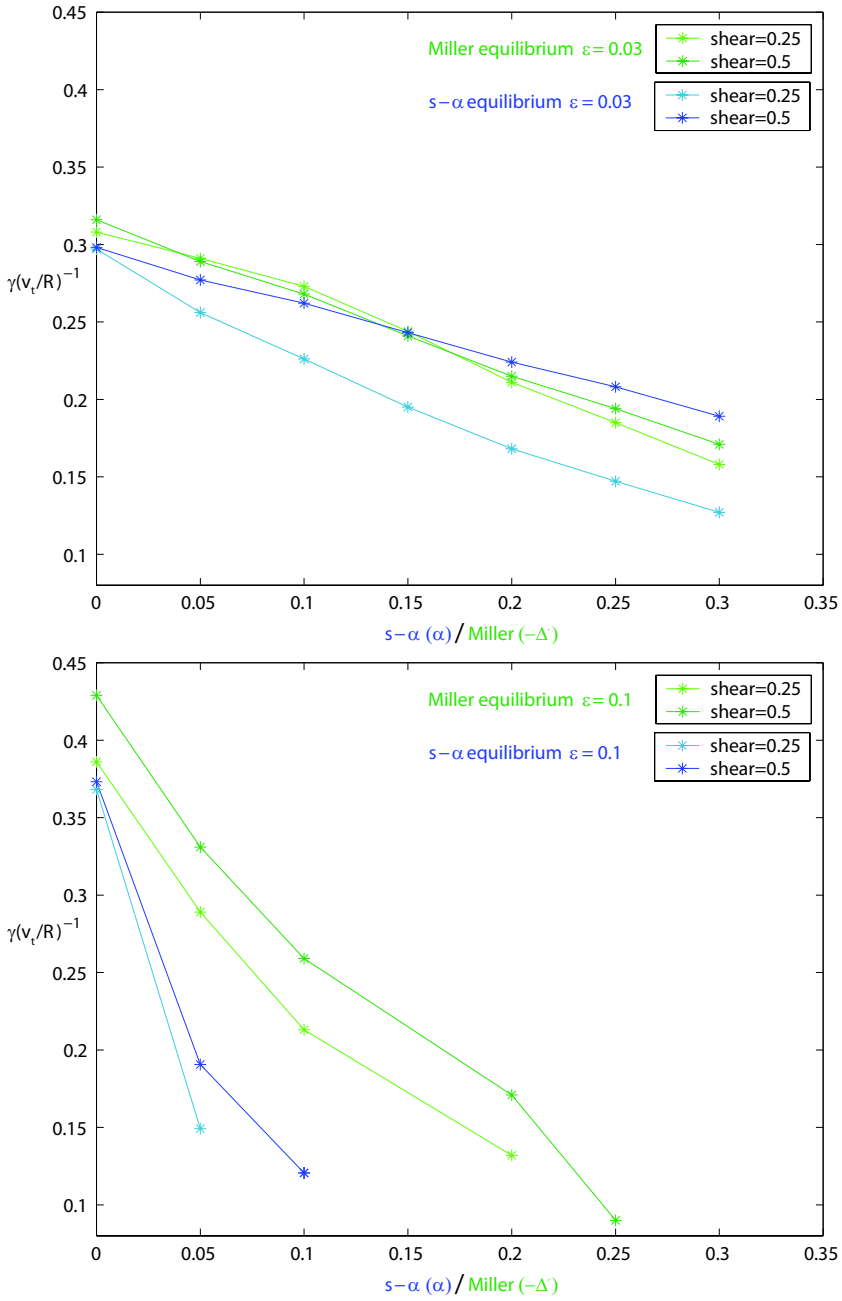

Figure 5.11: The effect of Δ' and α in the Miller and $\hat{s}-\alpha$ equilibria respectively, for the simple ITG case. Note that the figures show the results for different ϵ, $\epsilon = 0.03$ above and $\epsilon = 0.1$ below.

calculations, a moderate value of $\epsilon = 0.1$ and a small inverse aspect ratio, $\epsilon = 0.03$, in

order to illustrate the effect of ϵ in the scans. The results are shown in figure 5.11 where the normalized γ_{max} values are plotted against the α or $-\Delta'$ depending on the model used ($\hat{s}-\alpha$ or Miller), for $\epsilon = 0.03$ and 0.1.

On comparison of the $\hat{s}-\alpha$ and Miller plots at $\epsilon = 0.03$ it can be seen that the behavior is very similar in both models at $\hat{s} = 0.25$ and $\hat{s} = 0.5$. Both models predict an almost linear, inverse relationship between α or $-\Delta'$ and γ_{max}. Thus, it can be concluded that there is little or no difference, in the treatment of α or $-\Delta'$, in the two models in the limit of small ϵ. However, at $\epsilon = 0.1$ both the $\hat{s}-\alpha$ and Miller models predict a much larger stabilizing effect of the Shafranov shift parameter. It is evident also from figure 5.11 that the effect in the $\hat{s}-\alpha$ model at $\epsilon = 0.1$ is greater than for the Miller model. In particular, the turning on of α in the $\hat{s}-\alpha$ model reduces the growth rate of the modes dramatically, whereas, this effect is less pronounced in the Miller model.

If the simplified relationship between the Shafranov shift parameters of the two models, $\alpha \simeq -4\Delta'$, is true one would expect that the effect of α and Δ' in the models would be qualitatively the same, as it is seen to be. However, one would also expect that, with all other settings being the same, the $\hat{s}-\alpha$ model would predict the same γ_{max} value for α as the Miller model would predict for $\Delta' = -\alpha/4$. Looking at figure 5.11 this is not seen to be the case. This indicates that either the relation $\alpha \simeq -4\Delta'$ is not true or the treatment of α and Δ' in the models is different.

Thus, we can say that the effects of $\alpha/-\Delta'$ in the models is qualitatively the same with increasing $\alpha/-\Delta'$ decreasing the calculated γ_{max} values. The effect of α in the $\hat{s}-\alpha$ model is, however, more pronounced than the Miller model, at moderate ϵ. Here the $\hat{s}-\alpha$ model can calculate up to 50% smaller γ_{max} values than the Miller model at the same value of $-\Delta'$.

5.5 The dependencies in the experimental ITB case.

Now that the dependencies for the simplified situation have been identified a comparison with the experimental ITB case can be undertaken. For the experimental ITB case the settings are taken from the ITB discharge 12223, both the $\hat{s} - \alpha$ and Miller model settings are shown in table 5.2.

Model	R/L_N	R/L_{T_i}	R/L_{T_e}	α/Δ'	$\frac{T_e}{T_i}$	$\hat{s}$	q	Z_{eff}	κ	$\frac{d\kappa}{d\rho}$	δ	$\frac{d\delta}{d\rho}$	ϵ
$\hat{s} - \alpha$	2.23	16.63	15.52	0.87	1	-0.24	2.03	1	-	-	-	-	0.195
Miller	2.23	16.63	15.52	0.08	1	-0.24	2.03	1	1.395	0.847	0.025	0.007	0.195

Table 5.2: Table of $\hat{s} - \alpha$ and Miller experimental settings for the ITB discharge 12223. Note that, unless otherwise stated, these settings are only changed in the calculations when a parameter is being scanned.

A scan of the triangularity was done for the experimental settings of discharge 12223. Again, γ_{max} is seen to increase with δ, the overall change in γ_{max} is still very small, approx. 5%. Also a scan of the elongation was done for the experimental settings of discharge 12223. The experimental settings were the same as those of the scan of the triangularity for 12223 except that the triangularity δ was set to 0.025. As seen in the simple ITG case, γ_{max} decreases steadily with κ, the overall decrease is approx. 35%.

Thus, it can be concluded that the neglect of the triangularity from the calculations in the $\hat{s} - \alpha$ model is justified since it makes only a very small difference to the results. However the neglect of the elongation from the calculations in the $\hat{s} - \alpha$ model could lead to the growth rates of the modes being overestimated by as much as 35% and $R/L_{Ti(crit)}$ being underestimated by as much as 20%.

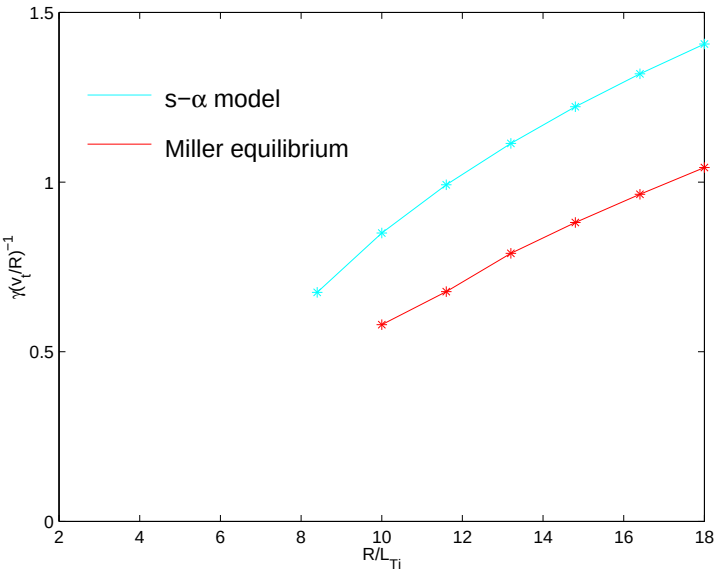

Figure 5.12: A comparison of the Miller (in red) and $\hat{s}-\alpha$ (in blue) models for the experimental settings of discharge 12223 and different values of R/L_{T_i}, with $\Delta' = 0$ and $\alpha = 0$. Note that the growth rate is normalized with respect to the v_t/R, where v_t is the thermal ion velocity. Since $T_i = 3.763KeV$, then the normalization factor is $v_t/R \approx 2.58 \times 10^5$.

5.5.1 The effect of the electron temperature gradient and the density gradient.

Figure 5.12 shows a comparison of the $\hat{s}-\alpha$ and Miller models for the experimental ITB case of discharge 12223, see table 5.2, however the Shafranov shift related parameter is set to zero, $\Delta' = 0$ and $\alpha = 0$. From this, one can see that the $\hat{s}-\alpha$ model predicts a much more unstable plasma than the Miller model. This is not what one would expect after studying the results outlined above of the effects of the elongation, triangularity and inverse aspect ratio.

Figure 5.13 illustrates other dependencies in the $\hat{s}-\alpha$ model which until now were not examined in this thesis. The results presented in this figure seem to show that the unexpected results of 5.12 can be explained by the large effect of $R/L_{T_e} \approx R/L_{T_i}$ and the inclusion of the real value of R/L_n has in the simulations in the $\hat{s}-\alpha$ model. Figure 5.13

shows that when $R/L_{T_e} = R/L_{T_i}$ (in light blue) in the simple ITG model the calculated γ_{max} is much greater than when it is calculated with $R/L_{T_e} = 0$. This difference is seen to increase with higher values of $R/L_{T_e} = R/L_{T_i}$. When R/L_n is set to the non-zero value, of $R/L_n = 2.23$, (in pink) another increase in the γ_{max} calculated is seen. These results explain why when the experimental settings of discharge 12223 are used in the calculations, see the dark blue curve in figure 5.13, the calculated γ_{max} values are much larger than those of the simple ITG (the red curve).

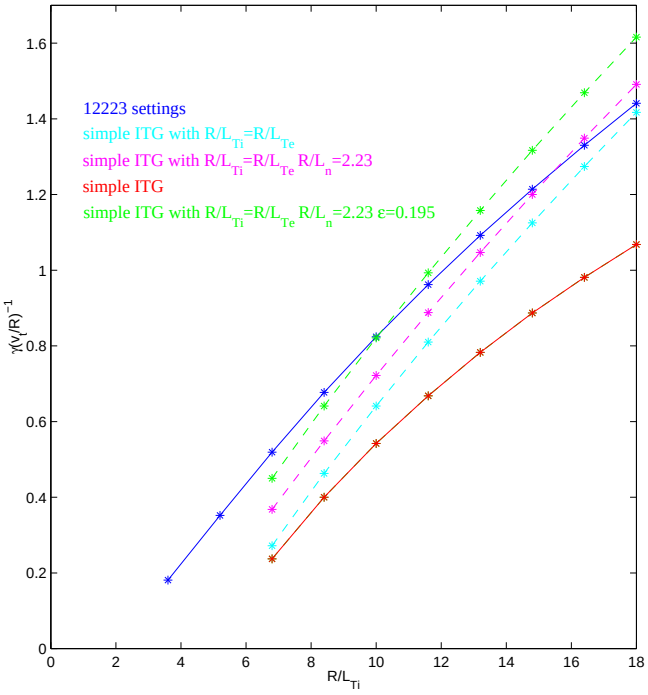

Figure 5.13: A study of the dependencies of the $\hat{s} - \alpha$ model, note $\alpha = 0$. Shown are the γ_{max} calculations for the simple ITG case (in red), the simple ITG case with $R/L_{T_e} = R/L_{T_i}$ (in light blue), the simple ITG case with $R/L_{T_e} = R/L_{T_i}$ and $R/L_N = 2.23$ (in pink), the simple ITG case with $R/L_{T_e} = R/L_{T_i}$, $R/L_N = 2.23$ and $\epsilon = 0.195$ (in green) and the experimental ITB settings of discharge 12223 (in dark blue).

A possible explanation of the above identified effects of $R/L_{T_e} \approx R/L_{T_i}$ and a non-zero R/L_n in the $\hat{s} - \alpha$ model is that for the simple ITG case the electron dynamics do not enter strongly. However, in the case of a experimental ITB, where in this case

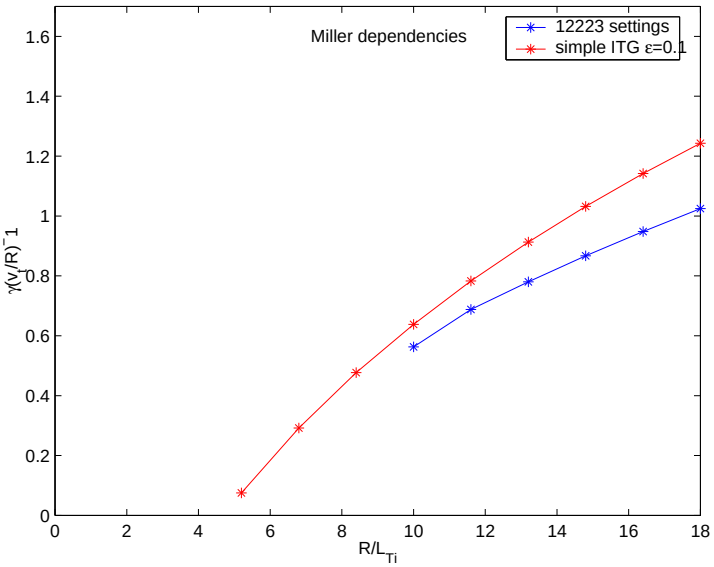

Figure 5.14: A study of the dependencies of the Miller model, note $\Delta' = 0$. *Note also that the results for the experimental ITB are shown in blue and for the simple ITG at* $\epsilon = 0.1$ *in red.*

$R/L_{T_e} \approx R/L_{T_i}$ and $R/L_n = 2.23$, the electron dynamics do drive other modes, other than the ITG mode. Thus far, in this thesis, the density gradient has been considered to be stabilizing, which indeed it is for a pure ITG. Theory, however, predicts that R/L_{T_e} and R/L_n are destabilizing for the so called trapped electron mode (TEM) [62]. Although the main modes that GS2 identifies in this case are ITG modes, there seems to be a significant drive from the electrons. This indicates that the modes identified in the plasma are not pure ITG modes. Thus, in this case the density gradient and the electron temperature gradient can destabilize the mode, as they are seen to do in the results presented in figure 5.13.

A similar, though not as detailed, plot is given for the Miller equilibrium in figure 5.14 and shows that the difference is not so vast between the simple ITG case and 12223 experimental case. Note also that here the growth rates for the experimental ITB case are consistently lower than the simple ITG case, even though the simple ITG calculations were done at a lower inverse aspect ratio. This can be explained

by the inclusion of the elongation, $R/L_{T_e} \approx R/L_{T_i}$ and the density gradient in the calculations. Note also that the inclusion of $R/L_n = 2.23$ and $R/L_{T_e} \approx R/L_{T_i}$ in the calculations for the experimental ITB settings did not lead to a noticeable increase in the calculated γ_{max} values as it did in the $\hat{s} - \alpha$ model. It is probable then that it is a overestimation of the destabilizing effects of R/L_{T_e} and R/L_n that cause the higher γ_{max} values calculated, for the experimental ITB case, in the $\hat{s} - \alpha$ model, presented in figure 5.12.

These results highlight the inadequacies of the $\hat{s} - \alpha$ model, as a tool for the stability calculations of the experimental ITB case discussed here. It can, thus, be concluded that; firstly, plasma shaping in the form of elongation (but not so much the triangularity) is of some importance for the accurate determination of the growth rates of the modes. Secondly, the $\hat{s} - \alpha$ model greatly underestimates the influence of the ion temperature gradient and the inverse aspect ratio on the growth rate of the mode. The $\hat{s} - \alpha$ model also seems to vastly overestimates the role of R/L_{T_e} and R/L_n in driving the TEM modes, as compared with the Miller model.

5.5.2 The effect of the Shafranov shift parameters.

The Shafranov shift related parameter scans for the simple ITG case of a circular plasma were repeated for the experimental ITB settings of discharge 12223, see table 5.2. The results are plotted in figure 5.15 which shows that the effect in the $\hat{s} - \alpha$ and Miller equilibria are very different. The $\hat{s} - \alpha$ model predicts only a very small reduction in γ_{max} between $\alpha = 0$ and $\alpha = 0.05$, after which point γ_{max} increases greatly and steadily with α. In the Miller equilibrium γ_{max} decreases until $\Delta' = 0.1$, it remains small until $\Delta' = 0.2$ after which point it increases rapidly. Also, the Miller model predicts that the ITG modes are much more stable than in the $\hat{s} - \alpha$ model. The scans of α and Δ' (figure 5.15) show a very different behavior of γ_{max}, both qualitatively and

quantitatively. Here, the $\hat{s} - \alpha$ model shows a very different dependence on α than that shown for the simplified ITG settings, see figure 5.11.

As shown at the beginning of this chapter the simplified relationship between α and Δ' is expected to be $\alpha \simeq -4\Delta'$. However, experimentally α can be quite a lot larger than Δ', see table 5.3 for the values of α and Δ' for various ITB discharges. In the discharge analyzed here, 12223, $\alpha \approx 0.87$ and $\Delta' \approx -0.082$, thus, α is approximately 10 times larger than $-\Delta'$. Looking at the other ITB discharges, in table 5.3, one sees that this is is a representative upper limit for the discharges. Thus at the experimental ITB settings the simplified relation $\alpha \simeq -4\Delta'$ does not hold.

Discharge	time/s	α	Δ'	$\alpha/-\Delta'$
12223	0.982	0.87	−0.083	10.5
12224	0.935	1.05	−0.133	7.9
13130	1.345	0.28	−0.102	2.8
13148	0.751	0.86	−0.085	10.1
13148	1.081	0.49	−0.087	5.6
13149	0.685	0.57	−0.117	4.9
13150	0.751	0.67	−0.154	4.4

Table 5.3: Table of α and Δ' values for real experimental ITB discharges.

Looking again at figure 5.15 at the results for the Miller equilibrium it can be seen that a change in Δ' from zero to -0.082 would indeed decrease the maximum linear growth rate, by approximately 25%. To see the effect of changing α from zero to 0.87 one would have to calculate the effects of α to higher values than those shown in figure 5.15, and due to time constraints this could unfortunately not be done within the time-frame of this work. However, figure 4.5 in chapter 4 includes the calculations for discharge 12223 at $\alpha = 0$ and $\alpha = 0.87$ and for this discharge shows a decrease in γ_{max} of approximately 35%.

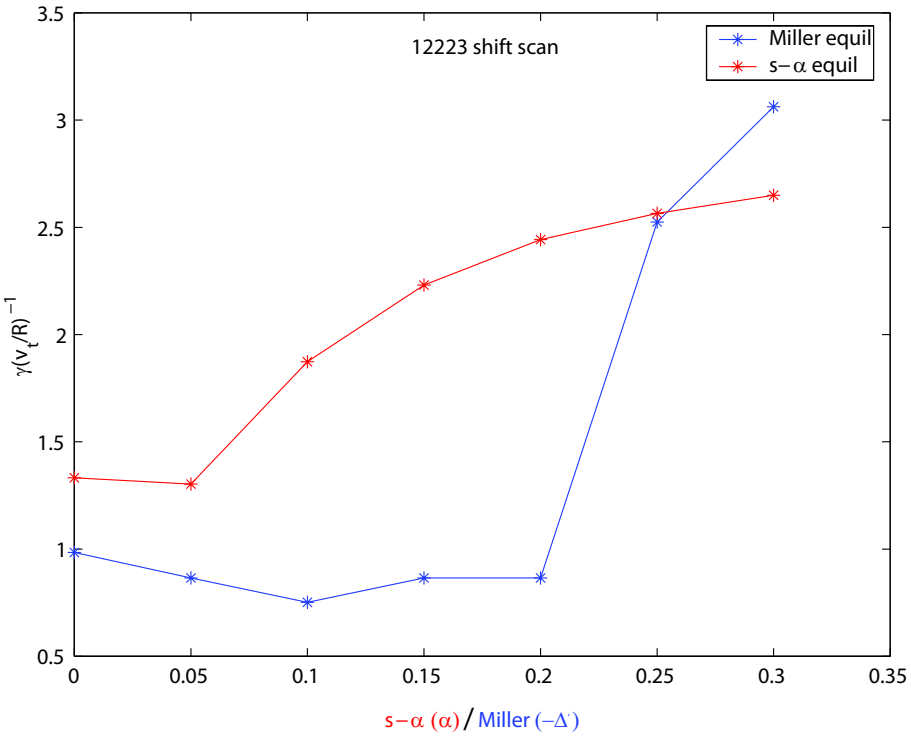

Figure 5.15: A comparison of the Miller and $\hat{s}-\alpha$ handling of the Shafranov shift related parameters, Δ' and α, for the experimental settings of discharge 12223. The Miller model results are shown in blue, here γ_{max} values are plotted versus $-\Delta'$. The $\hat{s}-\alpha$ model results are shown in red, here γ_{max} values are plotted versus α.

These results prompted the recalculation of the results shown in figure 4.5, which compared the calculated $E \times B$ shearing rate, $\omega_{E\times B}$ with the maximum linear growth rates of the modes, γ_{max}, calculated using the $\hat{s}-\alpha$ model for the ITB discharges of interest. These calculations were repeated using the Miller equilibria, along with the experimental values of elongation and triangularity which were neglected in the original $\hat{s}-\alpha$ model calculations previously used. As can be seen in figure 5.16 the results are quite interesting.

One can see, in figure 5.16, that the effect of the inclusion of the Shafranov shift related parameter is not as large as was previously predicted by the $\hat{s}-\alpha$ model. However,

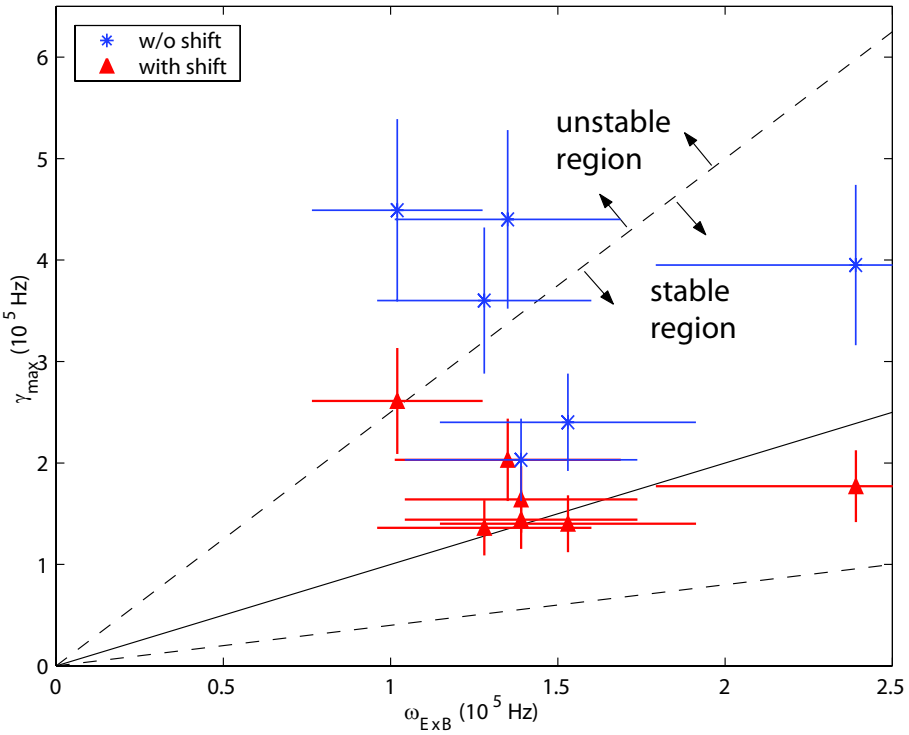

Figure 5.16: A comparison of the $E \times B$ shear with the maximum linear growth rate calculated using the Miller equilibrium, without the shift (in blue) and with the shift (in red). Note that here the un-normalized values of γ_{max} are plotted.

when it is included the discharges do satisfy the condition for mode stabilization by $E \times B$ shear, predicted by Waltz[24] as discussed in chapter 4.2. It is important to note that this is in contrast with the conclusions made before based on the results discussed in chapter 4.2 where the $E \times B$ shear was found to be not large enough to explain mode suppression during an ITB event. The large role of the Shafranov shift in facilitating mode suppression is also evident in the figure. There are three discharges in particular in which when the Shafranov shift contribution was neglected in the calculations the modes could not have been stabilized by the $E \times B$ shear. It can now be concluded that in these ITB discharges the $E \times B$ shear is sufficient to explain the mode suppression and that the earlier results were due to inaccurate dependencies within the $\hat{s} - \alpha$ model. It can also be concluded that the Shafranov shift and the $E \times B$ shear are, the most important stabilizing mechanisms identified in this the-

sis and that they are equally important from the point of view of turbulence suppression.

5.6 The calculation of the Shafranov shift parameters.

It is important at this stage that the method of calculating both α and Δ' be discussed, in order that an indication of the accuracy of the values quoted in this chapter can be ascertained. The values for α and Δ' given in the last section were calculated using the experimental profiles.

In this method for calculating α equation (5.27) is used with q and B_ϕ obtained from an equilibrium reconstruction. If one assumes that $n_i = n_e = n$, with $P = P_e + P_i = nT_e + nT_i$, $\frac{dP}{dr}$ can be expressed as

$$\frac{dP}{dr} = -\frac{P}{R_0}\left[\frac{R_0}{L_N} + \frac{\tau}{1+\tau}\frac{R_0}{L_{Te}} + \frac{1}{1+\tau}\frac{R_0}{L_{Ti}}\right], \tag{5.29}$$

where L_N and L_{Te} are the density and electron temperature gradient lengths respectively. Δ', the gradient lengths and $\tau \equiv T_e/T_i$ are calculated using a GS2 interface program.

The above calculation neglects the main deuterium ion dilution due to impurities. For this to be taken into account the ion density would be approximated by $n_i = n_e/Z_{eff}$, assuming that all ions have the same charge, here Z_{eff} is the effective charge of the plasma given by $Z_{eff} = \sum_p n_p Z_p^2/n_e$, n_p is the particle density and Z_p is the particle charge. For discharge 12223 Z_{eff} was calculated to be $Z_{eff} \approx 1.8$, using this value α can be calculated to be $\alpha = 0.85$. Thus, the inclusion of the effective charge in the calculations reduces α only very slightly and it can be concluded that it is acceptable to neglect it in the calculations.

5.7 Summary and discussions.

The dependencies within the $\hat{s} - \alpha$ and Miller models have been rigorously tested using the GS2 code and the results presented in this chapter. Here, the main results will be summarized and discussed.

The effects of plasma shaping within the Miller model were studied. It was found that the triangularity, the gradient in the triangularity and the gradient in the elongation have little effect on the growth rates of the ITG modes. On the other hand, γ_{max} is seen to steadily decrease with increasing elongation. Neglect of the elongation from the calculations could lead to the growth rate of the modes being overestimated by as much as 40% and $R/L_{Ti(crit)}$ being underestimated by as much as 20%.

Increasing the Shafranov shift related parameters in the two models is shown to cause a reduction in the maximum linear growth rate. In the simple ITG case, with $\epsilon = 0.1$, the decrease in γ_{max} in the $\hat{s} - \alpha$ model is seen to be much greater than for the Miller model. This is also seen using the settings of the experimental ITB case, again the $\hat{s} - \alpha$ model shows a larger reduction in γ_{max} than the Miller model. It has also been shown that the simplified relation $\alpha \simeq -4\Delta'$ does not hold for the shaped equilibrium used in the experiment.

Studies of the effect of the inverse aspect ratio in the $\hat{s} - \alpha$ and Miller models revealed that the $\hat{s} - \alpha$ model predicts a much smaller influence on γ_{max} than the Miller model. Both models show an almost linear relationship between ϵ and γ_{max}, with larger values of γ_{max} at larger values of ϵ. However the increase is almost 70% less in the $\hat{s} - \alpha$ model than in the Miller model, between $\epsilon = 0.02$ and $\epsilon = 0.244$. These results indicate that

the $\hat{s} - \alpha$ model severely underestimates the contribution of the inverse aspect ratio to the growth rate of the modes.

When scans of R/L_{Ti} were done for the experimental ITB settings of discharge 12223, using the $\hat{s} - \alpha$ and Miller models, the results showed that the $\hat{s} - \alpha$ model predicts a much more unstable plasma than the Miller model. It was found that this was due to the strong destabilizing effect of the density gradient and $R/L_{T_e} \approx R/L_{T_i}$ in the $\hat{s} - \alpha$ model. These results cannot be understood on the basis of the results for the simple ITG, because apparently the experimental ITB case is not a pure ITG case. This apparent discrepancy between the two models is probably due to the drive of the electrons in the experimental case. The results indicate that the geometry has a somewhat different effect in the simple (or pure) ITG case than it has in the case of an ITG case with substantial electron drive. However, further study is required in order to prove if this explanation is the correct one.

It can be concluded that the Miller model is a much more accurate model for the calculation of the stability of ITB discharges. In light of this, it was decided that the calculations of γ_{max} should be redone for all ITB discharges studied in this work. The γ_{max} values were calculated and were compared with the $E \times B$ shearing rate values which were given in chapter 4. The γ_{max} values are much smaller than the values calculated using the $\hat{s} - \alpha$ model and it was found that $\gamma_{max} \approx \gamma_{E \times B}$. It can be concluded that in these ITB discharges the $E \times B$ shear is sufficient to explain the mode suppression and that the earlier results were due to the incomplete equilibrium description of the $\hat{s} - \alpha$ model. It is also evident that the Shafranov shift and the $E \times B$ shear are the most important stabilizing mechanisms identified thus far in this thesis and that they are equally important from the point of view of turbulence suppression.

Chapter 6

ASTRA simulation of ITB discharges

In this chapter the results of the ASTRA simulation of ITB discharges will be discussed. These simulations are done in order to assess the agreement between current theoretical models and the experiment, in the case of ITBs. In the previous chapter it was shown that the paradigm of turbulence suppression due to $E \times B$ shear is in reasonable agreement with the experiment, although a factor of 2.5 uncertainty in the criterion must be allowed for. The results, however, showed only local calculations. Now, with these encouraging findings in mind the predictions over the whole barrier can be investigated. In this study the ASTRA transport code is used to simulate ITB discharges using the GLF23 model. The ASTRA (Automatic System for Transport Analysis) code [63] is a flexible programming system capable of creating numerical codes for predictive or interpretative transport modeling, for stability analysis or for processing experimental data. Several transport models are implemented in the ASTRA code, however, it is not possible to use the GS2 model in ASTRA, or in any other transport code, since it is too computationally intensive to be used in that way. Thus, since the GLF23 model has similar physics bases to the GS2 model it was decided that the GLF23 model would be the best choice.

The GLF23, or Gyro-Landau Fluid, model is based on the fluid equations including the effect of Landau damping.[64, 65] The types of instabilities included in this model are the toroidal ion temperature gradient (ITG) mode, the collision-less and dissipative trapped electron drift mode and the ideal magnetohydrodynamic (MHD) ballooning mode. This model includes a magnetic shear ($\hat{s}$), Shafranov shift (α) stabilization, as well as $E \times B$ shear stabilization of turbulence.

The ion and electron temperature and density are simulated by solving the set of transport equations, equations (59-60) in [63]. The experimental values close to the edge of the confinement zone (e.g. $\rho_{tor} = 0.8$) are taken as boundary conditions for the calculations because the physical model used in GLF23 is not expected to correctly describe the transport in the pedestal region of the plasma. Please note that the boundary for the two discharges, 12223 and 13149, analyzed differ, this is due to data quality reasons. For discharge 12223 it is $\rho_{tor} = 0.8$ and for discharge 13149 it is $\rho_{tor} = 0.7$. Also, in the simulations the experimental profiles for $\hat{s}$, q and v_{tor} are used. The experimental q profile evolution is calculated using the CLISTE equilibrium code constrained with MSE data over the entire duration of the discharge and involved recovering an equilibrium every 66 ms of the discharge. Thus, the q profile evolution includes approximately 14 time-points. The toroidal velocity measurements were taken from the charge exchange recombination spectroscopy (CXRS) diagnostic. The CXRS diagnostic measures the rotation of the carbon ions and assumes this to be the same for the main (deuterium) ions. The dilution of the main deuterium ions by impurity ions is taken into account in the ASTRA simulations. Due to the impurities the electron and ion densities are not equal. The effective charge of the plasma Z_{eff} is given by, $Z_{eff} = \sum_p n_{ij} Z_i^2 / n_e$, where n_{ij} is the impurity species density and Z_i is the impurity species charge. In this way the ion density can be approximated by $n_i = n_e / Z_{eff}$, assuming that all ions have the same charge. The main ion density can be thought of as being made up of two contributions, these are, the density of the bulk plasma and the

density of the fast ions. The electrons generated by the ionization of the fast neutrals thermalize with the plasma very rapidly. However, due to the significant velocity of the fast ions generated by the ionization of the neutral beam, relative to the the bulk ions, their thermalization time (slowing down time) is long and approaches, under the conditions of an ITB, the confinement time of the plasma. Thus, the ion density is given by $n_i = n_{i(th)} + n_i(fast)$ where $n_{i(th)}$ is the thermal ion density and $n_i(fast)$ is the fast ion density contribution from the neutral beams. Due to quasi-neutrality being satisfied the total experimentally measured electron density, $n_e[exp]$, equals that of the ions (for $Z_{eff} = 1$). This means that the electron density will reflect both the thermal as well as the non-thermal ion distribution. The ASTRA simulations shown in this chapter ignore the contribution to both the electron and ion densities from the neutral beam. The ASTRA code simulates the total electron density to be the density of the bulk electrons only, which we will call $n_e[m]$. The thermal (or bulk) ion density which is used as the total ion density in the calculations, is $n_{i(th)} = n_e[m]/Z_{eff}$. Thus, the total electron density can be approximated by $n_e = n_e[m] + n_i(fast)$. It should be noted that the total electron density, $n_e = n_e[m] + n_i(fast)$, is plotted in the figures in this chapter for comparison purposes. It is important to remember that this is not the density used in the calculations, the code uses $n_e[m]$ for the transport calculations. The simulated densities are further discussed in the next section.

Note that the growth rate of a mode, γ is a measure of how quickly the amplitude of the mode grows, the slower the amplitude grows the more stable the plasma is. The maximum linear growth rate, γ_{max}, is the growth rate of the most unstable mode. Note also that γ_{max} can be naturally normalized to v_t/R, where v_t is the thermal velocity, and since in this chapter γ_{max} is compared with $\gamma_{E\times B}$ the same normalization factor is chosen for the latter. All plots in this chapter show normalized γ_{max} and $\gamma_{E\times B}$ values.

Figures 6.1 and 6.2 show the results of the simulations for ITB discharges 12223 and 13149 respectively. Note that of the ITB discharges examined as part of this work, only

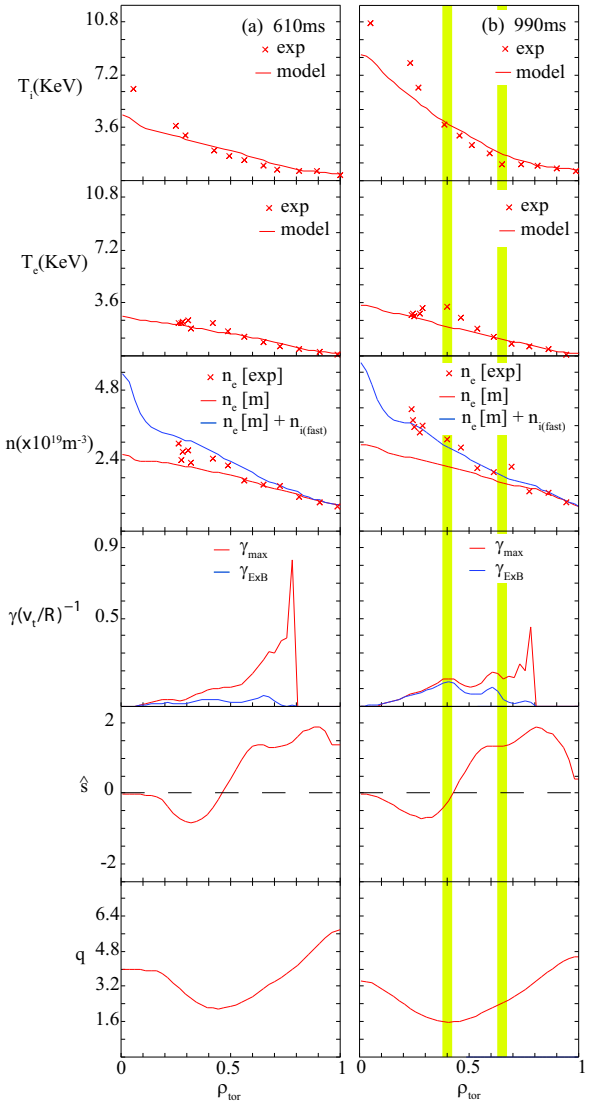

Figure 6.1: Simulation of ITB discharge 12223, results shown at (a) 610 ms and (b) 990 ms. Note that only the region $\rho_{tor} < 0.8$ is simulated, outside this the experimental values are used. The yellow bands indicate approximately the position of the barrier foot, either experimentally, analytically or both. The experimental data is also shown for the temperature and density (marked by x) so that one can compare the calculated values with the experimental ones easily.

these two had all the necessary experimental data available for simulation using the ASTRA code. In these simulations only the toroidal velocity contribution to the electric field is used, i.e. the contribution of the poloidal and velocities are neglected as is the

contribution of ∇p. It is shown in a later section, 6.3, that it is reasonable to calculate the electric field in this way. The fast ion density, or ion density of the neutral beams, is calculated using a pencil model and neutral beam deposition,[66] in a self-consistent manner. It is shown in the figures for comparison purposes only, it is not included in the calculations, see [67] as an indication of how this could effect the simulation.

In the case of discharge 12223, see figure 6.1(a) at 610 ms, from the ion temperature it can be seen that the experimental data shows the beginnings of an ITB, whereas the calculated profile does not. The normalized growth rate of the modes is much larger than the $E \times B$ shearing rate except at the very center of the plasma, where they both go to zero. No barrier is seen in the electron temperature or density either. At the later time point of 990 ms, figure 6.1(b), there is an ITB in the experimental ion temperature. The calculated profile also predicts an ITB, though not as strong as the experimental one. The modelled ion temperature profile does not fit the experimental one inside $\rho_{tor} \approx 0.3$, this could be due to the neoclassical transport being overestimated in this region. The neoclassical description of banana orbits is not perfect especially close to the center of the plasma. No barrier is seen in either the experimental or predicted T_e and n_e profiles. Also, looking at part 6.1(b), at 990 ms, one notices that $\gamma_{E\times B} \approx \gamma_{max}$ for $\rho_{tor} \leq 0.4$ and that there is a step in the $T_i[exp]$ profile at this position. In other words the inner ITB foot is located at approximately this position, in the negative shear region. There is, however, a second ITB region with a different gradient which extends outward and has its foot at approx. $\rho_{tor} \approx 0.65$ in the positive shear region, $\hat{s} \approx 1.4$, at this position γ_{max} is larger than $\gamma_{E\times B}$ but could still be within the error bars of the Waltz criterion for turbulence suppression discussed in section 4.2.[11, 26] .

At the early time-point, 570 ms, in discharge 13149, see figure 6.2(a), the ITB is already formed in $T_i[exp]$ and reaching temperatures of approx. 8.5 KeV in the center of the plasma. The simulated ion temperature does not agree with the experimental one. The other experimental and modelled profiles of n_e and T_e do not show an ITB. $\gamma_{max} > \gamma_{E\times B}$ over the entire plasma although in the region of approximately $\rho_{tor} \leq 0.3$ they are very

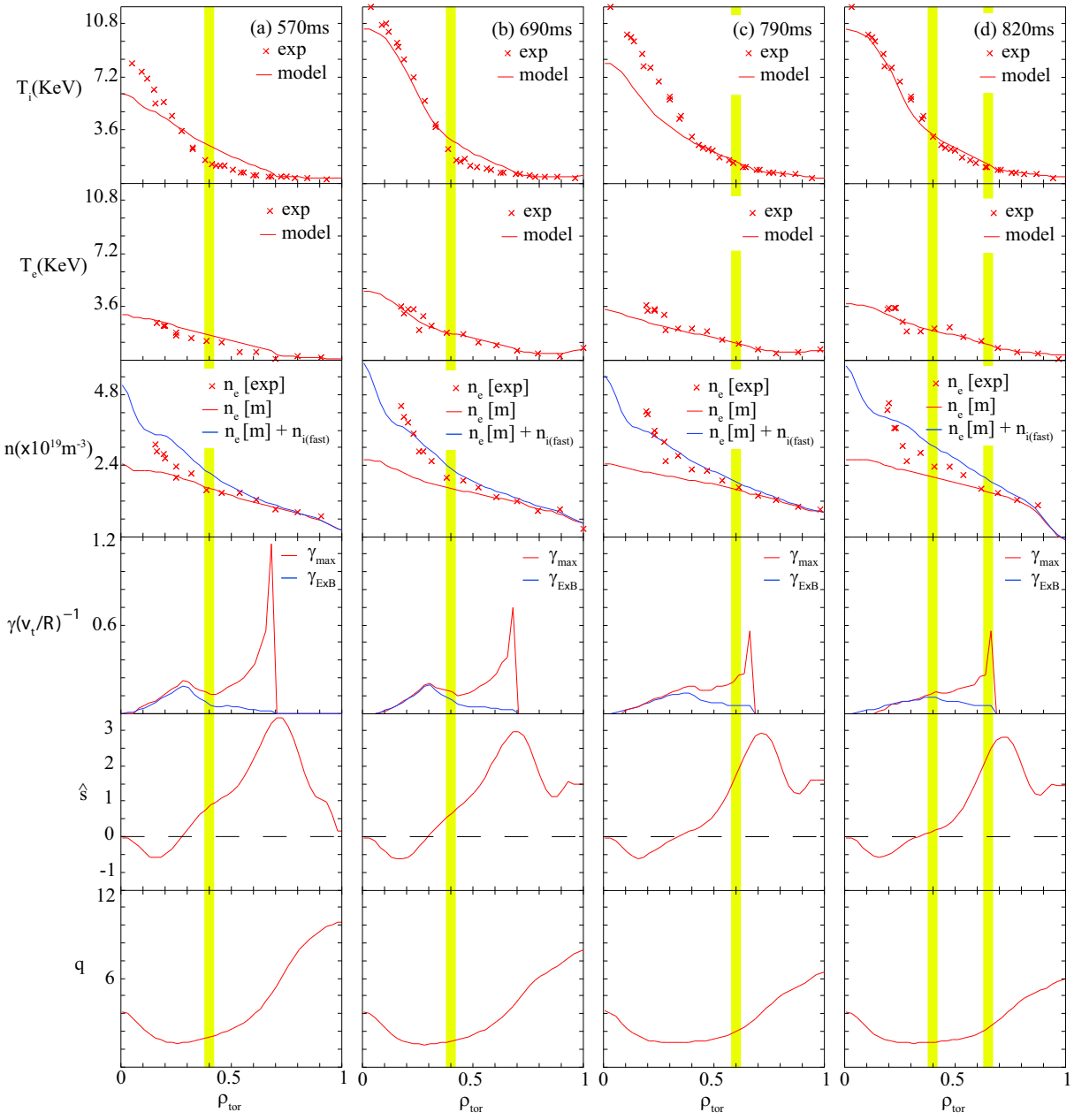

Figure 6.2: Simulation of ITB discharge 13149, results shown at (a) 570 ms, (b) 690 ms, (c) 790 ms and (d) 820 ms. Note that only the region $\rho_{tor} < 0.7$ is simulated, outside this the experimental values are used. The experimental data is also shown for the temperature and density (marked by x).

close in value and within the error bars of the Waltz criterion for turbulence suppression discussed in section 4.2.[11, 26] At the time point of 690ms 6.2(b) the ITB has become much stronger and is reasonably well predicted by the model inside $\rho_{tor} \approx 0.33$ which, incidentally, is the region where $\gamma_{E\times B}$ compares well with γ_{max}. The model predicts an inner ITB foot at $\rho_{tor} \approx 0.33$. Outside this the model predicts a higher ion temperature than the experiment. The model predicts an inner ITB foot at $\rho_{tor} \approx 0.33$ slightly inside the experimental one which is positioned at $\rho_{tor} \approx 0.4$. Later, at 790ms, the ITB has weakened in both the experimental and modelled profiles, so much so that the model barely predicts a barrier at all. Experimentally the ITB outer foot is more difficult to pinpoint than before and is approximately at $\rho_{tor} \approx 0.6$. At this position γ_{max} is much greater than $\gamma_{E\times B}$ and $\hat{s} \approx 2$, $q \approx 2.4$. The experimental inner foot is located at $\rho_{tor} \approx 0.4$, the modelled foot location is also at approximately $\rho_{tor} \approx 0.4$ and γ_{max} compares reasonably well with $\gamma_{E\times B}$ up to this position. At approximately 800ms additional NBI heating (2.5 MW) is switched on. At 820 ms, figure 6.2(d) the model fits the $T_i[exp]$ very well. Experimentally the ion temperature profile has only changed very slightly since 790ms. The experimental outer foot is positioned at $\rho_{tor} \approx 0.65$ at this position $\gamma_{max} >> \gamma_{E\times B}$, $\hat{s} \approx 2$ and $q \approx 2.5$. It is difficult to ascertain whether an outer foot is seen in the modelled profile since the transport is only calculated up to $\rho_{tor} \approx 0.7$ in this case. There is also an inner ITB region, in both the experimental and modelled profile, with its foot positioned at $\rho_{tor} \approx 0.4$ at this position $\gamma_{max} \approx \gamma_{E\times B}$, $\hat{s} \approx 0$ and $q \approx 1.5$. At all of these time-points no ITB is seen in the $T_e[exp]$ profile, which is well predicted by the model. The $n_e[exp]$ profile becomes increasingly more peaked, this is not reflected in the simulation, where $n_e[model]$ is flat and hardly changes throughout the discharge.

6.1 The simulated density

As mentioned before the simulations in section 6 were done using a calculated density profile. As can be seen in the previous figures in this chapter the experimental density is not well reproduced. The model predicts a flat density profile while the experimental profile is peaked. In this section the effect of the density peaking will be examined. Figures 6.3 and 6.4 show calculations using the measured (peaked) density profile and a calculated (flat) density profile for discharges 12223 and 13149 respectively. These simulations are done by using a density "switch" which switches the calculations from the measured density profile to a calculated one, in this way these calculations can be done within the same simulation.

In both cases, 12223 and 13149, the calculations before the switch, i.e. with the experimental density, figures 6.3(a) and 6.4(a) show no ITB even though there is one experimentally. Invariably when the peaked experimental density profile is used in the simulations no ITB is predicted by the model. However, once the density profile is switched to the calculated one (which is always unpeaked or flat) an improvement in the confinement is immediately seen. In fact, in figure 6.3(b) for discharge 12223 within 100ms of the switch, which took place at 1126ms, the predictions of the model are in line with the experiment, showing an ITB. Also note the reduction in γ_{max} and $\gamma_{E\times B}$ in the region $\rho_{tor} \leq 0.6$, however γ_{max} has decreased the most and hence $\gamma_{max} \approx \gamma_{E\times B}$ over a much greater region of the plasma.

For discharge 13149 the confinement improvement after the switch to the modelled density profile, which took place at 643ms, is slower, but by comparing 6.4(a) and 6.4(b) the speed with which the confinement improvement happens after the switch can be seen. Within 12ms a substantial improvement is seen in both the ion temperature and γ_{max}. This improvement continues and at 794ms (figure 6.4(c)) though the model does not fit the ITB it is predicting a weaker ITB and turbulence suppression over a large

part of the plasma radius ($\gamma_{max} \approx \gamma_{E\times B}$ for approximately $\rho_{tor} \leq 0.45$).

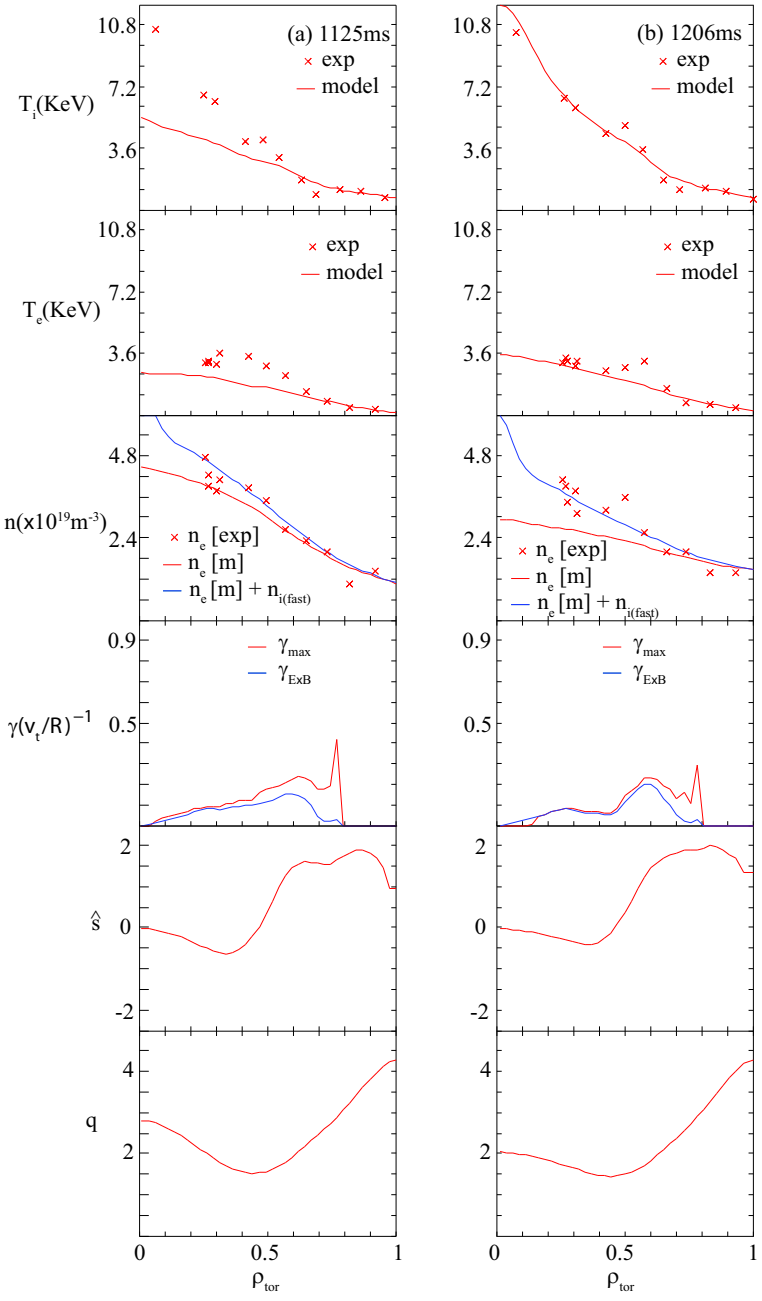

Figure 6.3: ASTRA results for discharge 12223 showing the dependence of the confinement on the peakedness of the density profile. Note: There is a switch at t = 1126 ms from the experimental n_e (a) to a calculated one (b).

Another very interesting point which is highlighted in figures 6.3 and 6.4 is that in 4 out of 5 of the time-points analyzed the $n_e[m] + n_i(fast)$ profile shows a remarkable fit to the $n_e[exp]$ profile. This indicates that the simulated density profile might indeed be the correct density profile for the thermal ions, since due to quasi-neutrality the electron density is equal to the sum of the thermal and the non-thermal contribution. As mentioned before $n_e = Z_{eff} n_i$. Thus, the modelled ion density profile is proportional to the modelled, flat, electron density profile. However, the ion density in the experiment consists of a thermal as well as a fast particle contribution. Assuming the ion thermal density profile is correctly predicted by the model, the electron density profile would be that of the thermal ions plus the contribution of the non-thermal part. Indeed, this fits the experimental results well and one could therefore argue that the prediction of the density is correct. The latter however is only true as long as the density gradient of the electrons does not strongly drive the instability. As figures 6.3 and 6.4 show either ∇n_i or ∇n_e does strongly drive the instability. On theoretical grounds one would expect such an effect from ∇n_e [68]. From the comparison with the experiment it follows that the effect of ∇n_e is too large in the model. When this drive is suppressed the prediction of the electron density profile is in good agreement. The fact that using the peaked experimental density (both ion and electron) in the simulations prevents an ITB forming indicates that either or both the ion and electron density gradient is strongly driving the modes. Since the plasma is also seen to be more turbulent. Since, the peakedness of the profiles could not be studied separately it is not possible to decide from these results which drive dominates. The electron density gradient has a strong effect on the trapped electron mode (TEM). Hence, theoretically it is expected to be the electron density gradient which is the stronger of the drives. Also, since the peaked density profile prevents the ITB from forming in the model, it can be concluded that the drive of the mode due to the density gradient is overestimated.

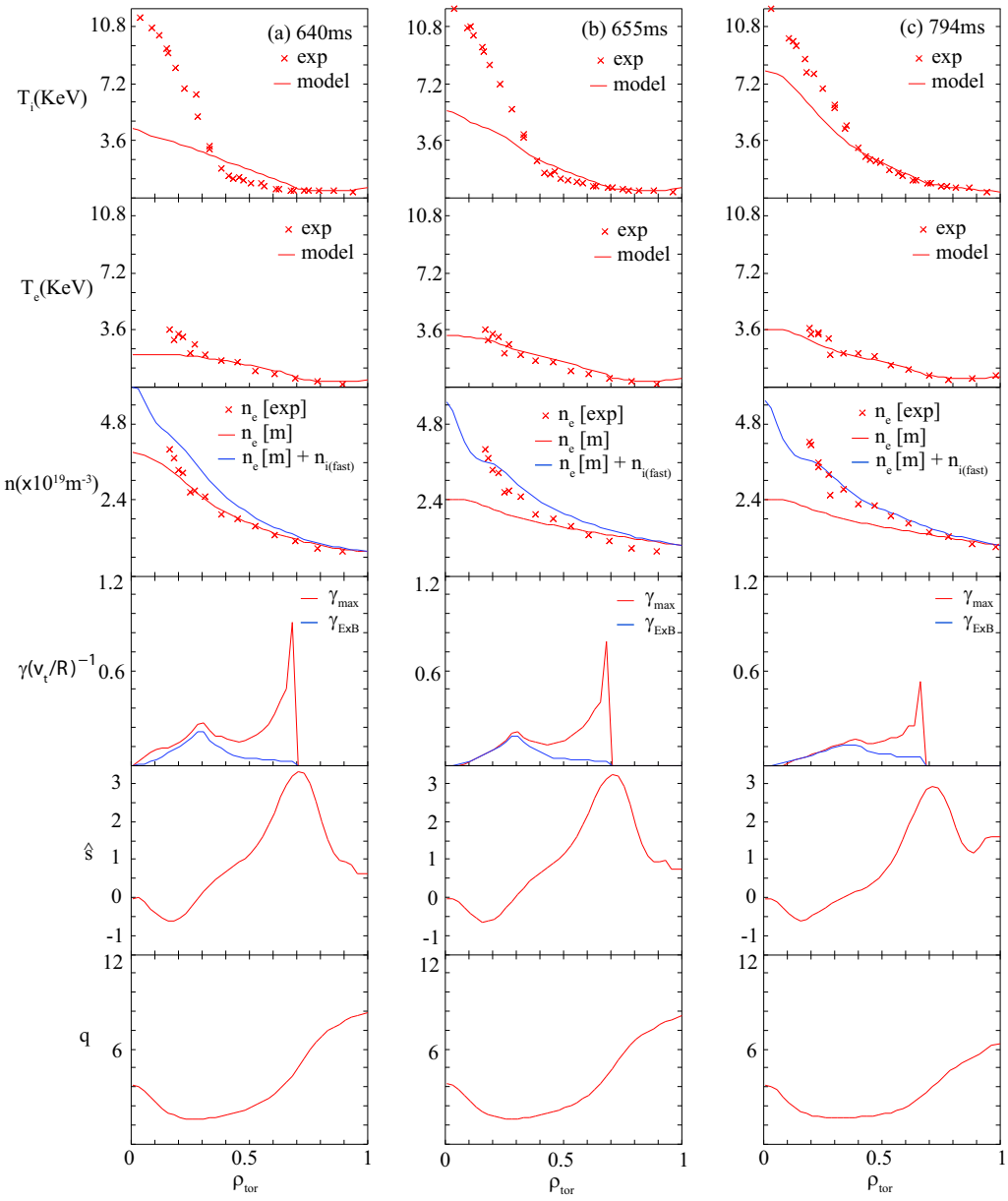

Figure 6.4: ASTRA results for discharge 13149 showing the dependence of the confinement on the peakedness of the density profile. Note: There is a switch at $t = 643$ ms from the experimental n_e (a) to a calculated one (b) and (c). Note also that the apparent discrepancy in the decreasing magnitude of γ_{max} and $\gamma_{E\times B}$ while T_i and ∇T_i are increasing strongly is due to the fact that γ is normalized to $\frac{v_{th}}{R}$.

6.2 The Shafranov shift

In this section the simulations of the effect of the Shafranov shift related parameter (α) are analyzed. This is done by calculating α within the model (α_{model}) and scaling it to agree with the (α) calculated from the experimental profiles (α_{exp}). Here, α is calculated from the temperature and density profiles using the method described in chapter 5.6. The α calculated from the modelled profiles is invariably smaller than α_{exp}. In the case of discharge 12223, figure 6.5, the different values of α used are 0.0, 0.5*α_{model} and 2.0*α_{model}. α_{model} is calculated from the modelled temperature and density profiles, whereas the experimental one is calculated from the experimental profiles and is shown as a comparison, i.e. α_{exp} is not used in the simulations. As can be seen from the figure changing α in this way makes very little difference to the confinement. Only a small change is seen in the fit to the experimental ion temperature profile with the fit becoming slightly worse between $\alpha = 0$ and $\alpha = 0.5 * \alpha_{model}$ and then a bit better again at $\alpha = 2.0 * \alpha_{model}$. The results for discharge 13149 are shown in figure 6.6. Here the first two plots show the results for discharge 13149 at two different values of α, $\alpha = 0.4 * \alpha_{model}$ and $\alpha = \alpha_{model}$, at the same time-point of 570ms. As seen with discharge 12223 there is practically no change in the confinement. The other plot in figure 6.6 shows the ITB at a later time-point, of 680ms, and shows a comparison with α_{exp}. Based on the results presented in figures 6.5 and 6.6, it can be concluded that the model is quite insensitive to changes in α. These results show that, in contrast to the $\hat{s} - \alpha$ model GS2 code results, presented in chapter 5, the GLF23 model is quite insensitive to changes in α.

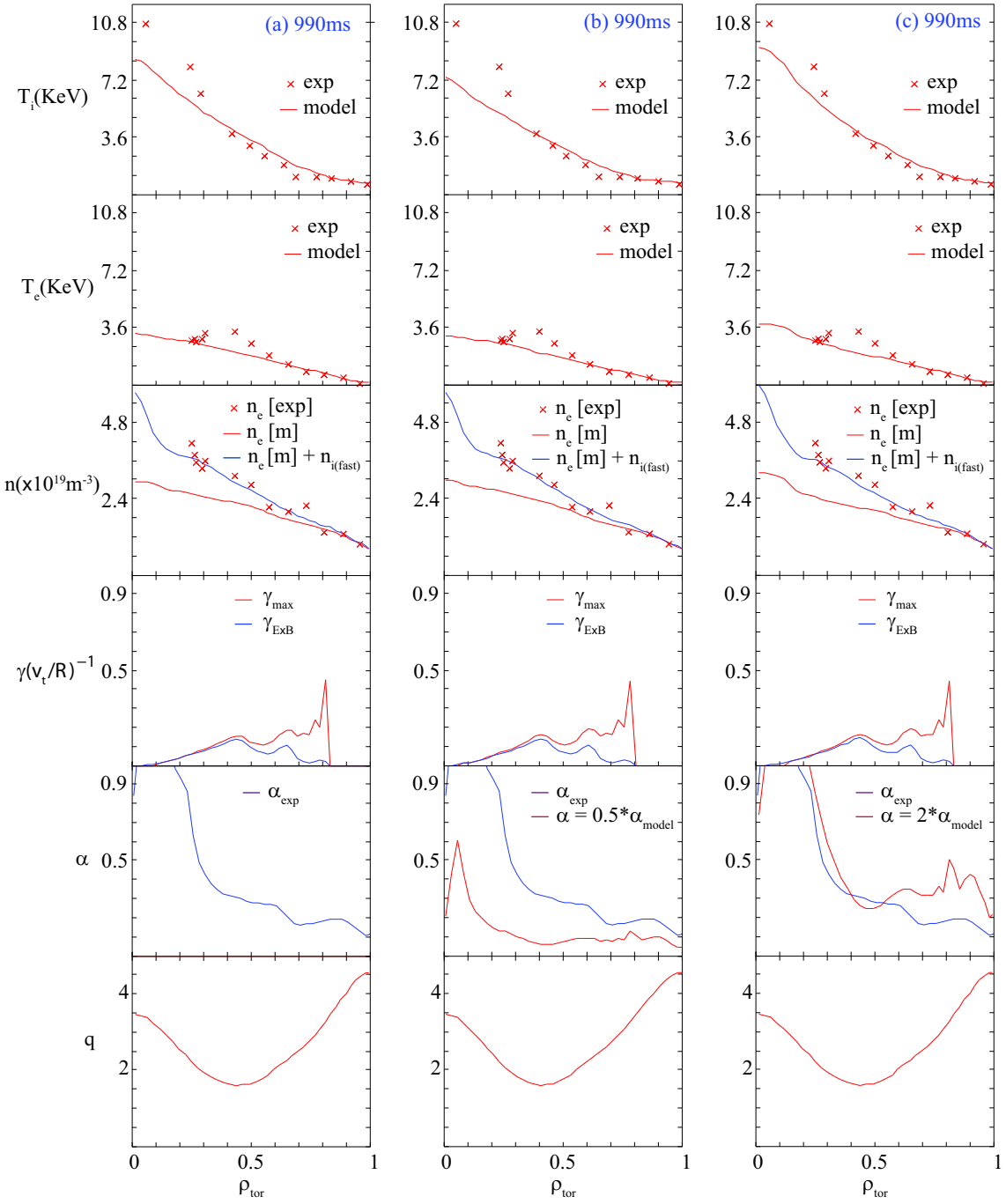

Figure 6.5: 12223 ASTRA results showing the effect of α. Note that only the region $\rho_{tor} < 0.8$ is simulated, outside this the experimental values are used. The experimental data is also shown for the temperature and density (marked by x).

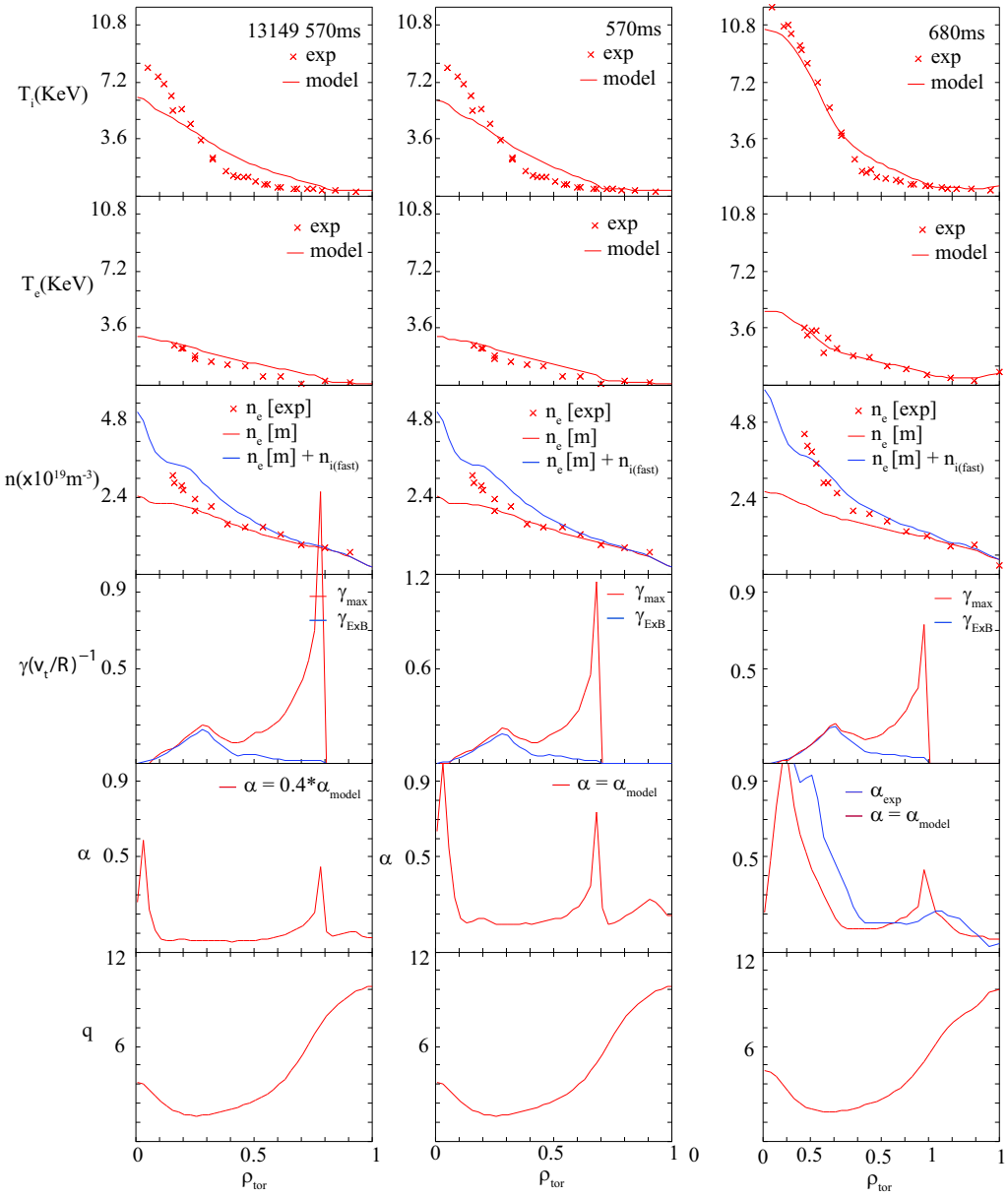

Figure 6.6: 13149 ASTRA results showing the effect of changing α at the same time-point, first and second columns. The third column shows a comparison of the experimental and modelled α profile at a later time-point. Note that only the region $\rho_{tor} < 0.7$ is simulated, outside this the experimental values are used. The experimental data is also shown for the temperature and density (marked by x).

6.3 The poloidal and diamagnetic velocities

Figure 6.7 shows the calculated contribution to the radial electric field from the poloidal, diamagnetic and toroidal velocities. As mentioned before the poloidal and diamagnetic velocities are not used in the transport simulations hence the total electric field also shown in the figures depends on the toroidal velocity. The v_{pol} and v_{dia} contributions are not as small as was previously expected.[18] In fact $E_r(v_{pol})$, $E_r(v_{dia})$ and $E_r(v_{tor})$ have the same order of magnitude. However, since $E_r(v_{dia})$ is in the opposite direction to $E_r(v_{pol})$ their combined contribution is small and hence the correction should be within the assumed error bars of approximately 20%. It can be concluded that it is acceptable to neglect their contribution in the calculations and use only the toroidal velocity contribution.

6.4 Main ion toroidal velocity

As a check for the $E \times B$ shearing rate calculations shown in sections 4.2 and 5.4.4, in this section $\omega_{E\times B}$ is calculated using the toroidal velocity of the main (deuterium) ions. The previous calculations were done using data from the Charge Exchange (CEZ) diagnostic which measures the toroidal rotation of the impurity (carbon) ions and assumes that this is the same as that of the main ions. However, it has been shown in the work reported in [69] that v_{tor} of the deuterium ions can be calculated, neoclassically, by adding a correction to v_{tor} of the carbon ions and is given by [70]:

$$v_{tor}(ion) \sim v_{tor}(imp) - \frac{3}{2} K_2 \frac{\nabla T_i}{Z_i e B_\theta} \tag{6.1}$$

where K_2 is a coefficient of the order of unity given in [70], Z_i is the main ion charge, e is the elementary charge, B_θ is the poloidal magnetic field and $< B > \sim B_\phi$ is assumed, this results in the v_{tor} correction being slightly overestimated[71]. This means that generally v_{tor} of the main ions is greater than that of the carbon ions. The correction is done using the ASTRA transport simulation code. The code requires the data

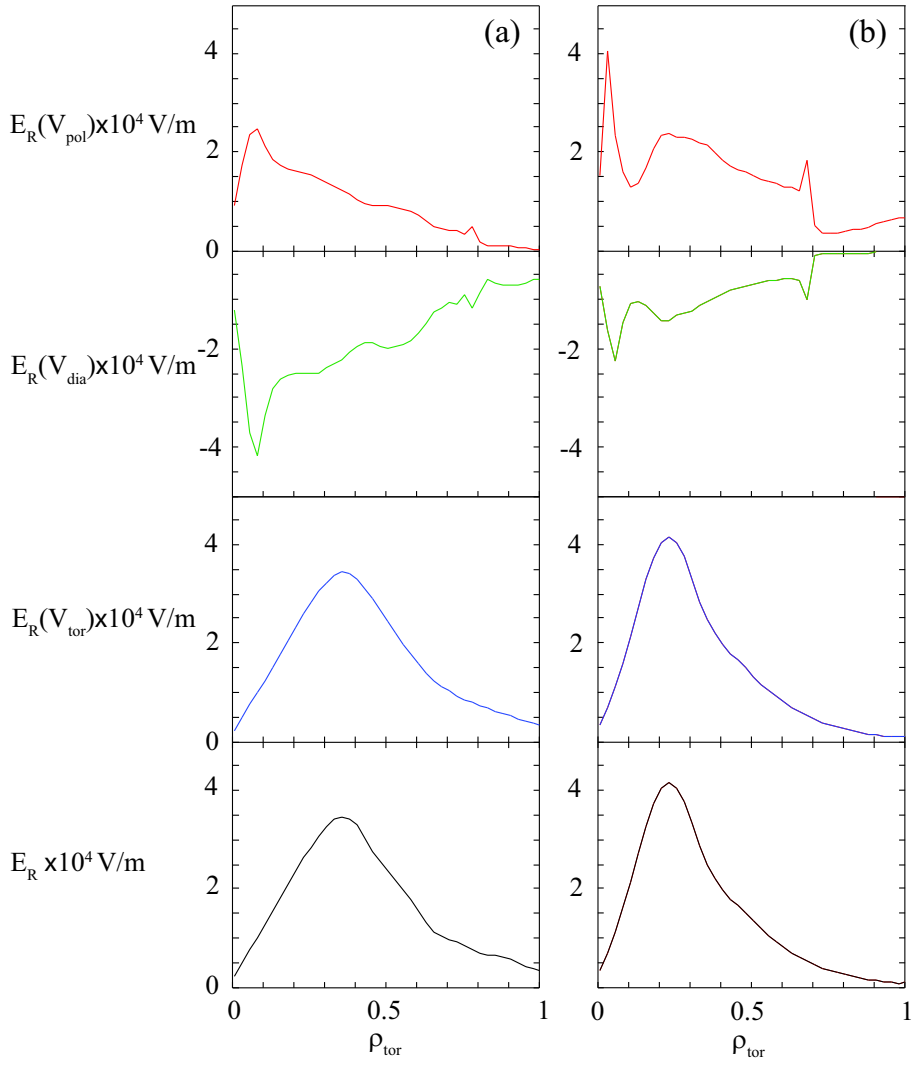

Figure 6.7: ASTRA results showing the contributions of v_{pol}, v_{dia} and v_{pol} to E_r for discharge (a) 12223 at t = 990 ms and (b) 13149 at t = 570 ms. Note that only the region $\rho_{tor} < 0.7$ is simulated, outside this the experimental values are used. The experimental data is also shown for the temperature and density (marked by x).

from various diagnostics as an input, thus, as mentioned earlier in this chapter, the calculations were only possible for two ITB discharges being studied. Hence, the results shown here merely act as an indication of the possible correction to $\omega_{E\times B}$ results given in section 4.2 and 5.4.4.

The ASTRA simulation code is used to exactly match the experimental discharge in question, i.e. the experimental density, temperature and v_{tor}(imp) measurements are used with some smoothing, they are not allowed to evolve within the simulation. The toroidal velocity of the main ions is then calculated by correcting the v_{tor}(imp) using equation (6.1) above. The calculated v_{tor}(ion) can then be used as an input for the CLISTE equilibrium code in order to recalculate the $E \times B$ shearing rate, using the same method as was used in section 6.

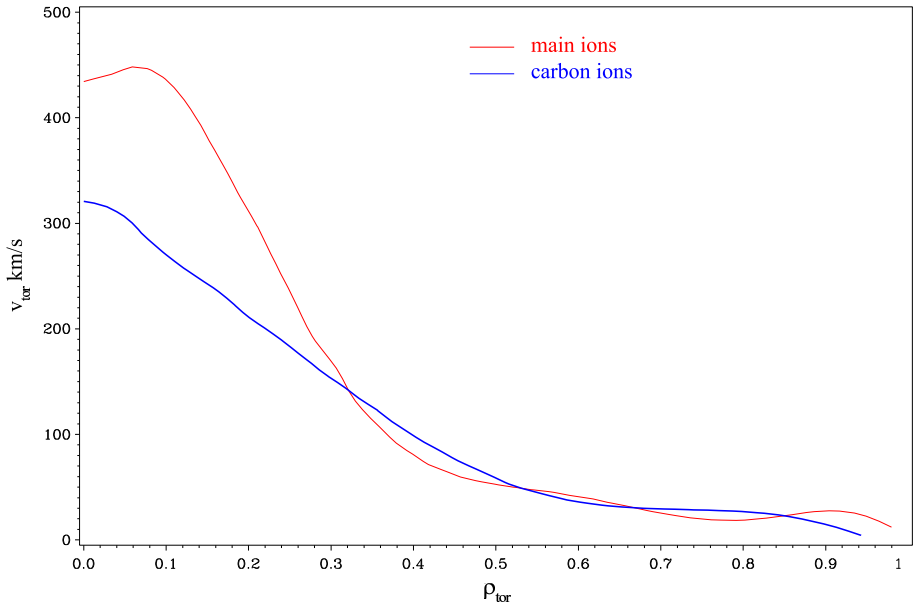

Figure 6.8: The calculated $v_{tor}(ion)$ for discharge 12223. $v_{tor}(ion)$ is shown in red and $v_{tor}(imp)$ is in blue.

The two discharges examined were discharge 12223 and 13149, the results for v_{tor}(ion) are shown in figures 6.8 and 6.9 respectively, also shown is the original v_{tor}(imp) as a comparison. One can see that in both cases there is an increase in v_{tor} towards the center of the plasma and the profiles become steeper inside $\rho_{tor} \approx 0.4$, nevertheless, the change in the profiles is not very large. As seen in figures 6.10 and 6.11 this increase

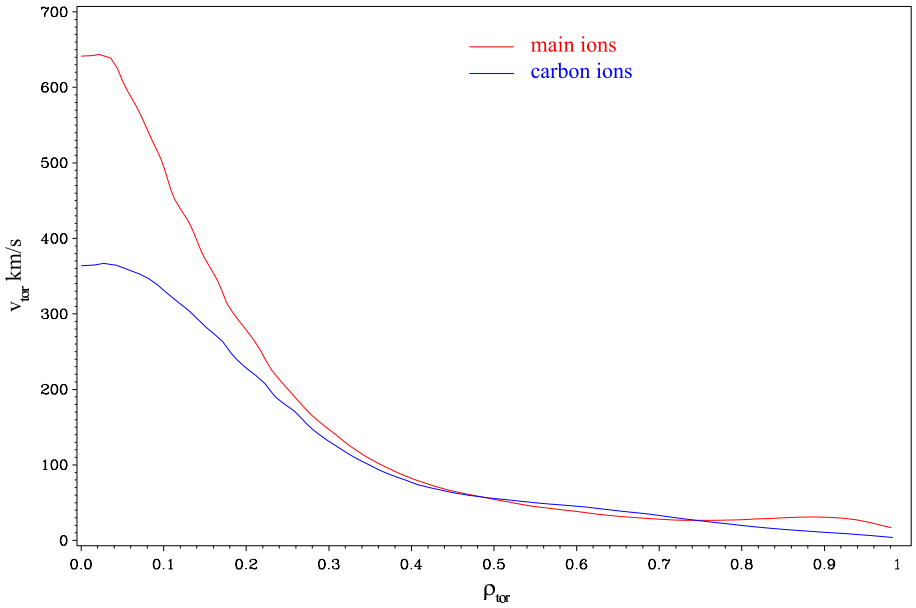

Figure 6.9: The calculated $v_{tor}(ion)$ for discharge 13149. $v_{tor}(ion)$ is shown in red and $v_{tor}(imp)$ is in blue.

in steepness greatly effects the calculated $\omega_{E\times B}$. These plots show the newly calculated $\omega_{E\times B}$ from v_{tor}(ion) in compared with the previous calculation using v_{tor}(imp) in blue, the dotted lines indicate the calculated Monte Carlo error bars. The new $\omega_{E\times B}$ profiles are sometimes outside the error bars, mainly towards the center of the plasma where $\omega_{E\times B}$(ion) is larger than $\omega_{E\times B}$(imp), here the new $\omega_{E\times B}$ can be up to a factor of 2 larger. However, in the area where the calculations for figure 4.5 are taken, in this case at approximately $\rho_{tor} = 0.4$, $\omega_{E\times B}$(ion) is within the error bars for these two discharges. Thus, these results indicate that using the real v_{tor}(ion) in the calculations for all the discharges would most likely increase the calculated $\omega_{E\times B}$ hence, a more stable situation would be predicted than that seen in figure 4.5. As with the results presented in chapter 5, these results reinforce the hypothesis of $\omega_{E\times B}$ being a major stabilizing mechanism within the plasma with relative importance from the point of view of ITB formation and sustainment.

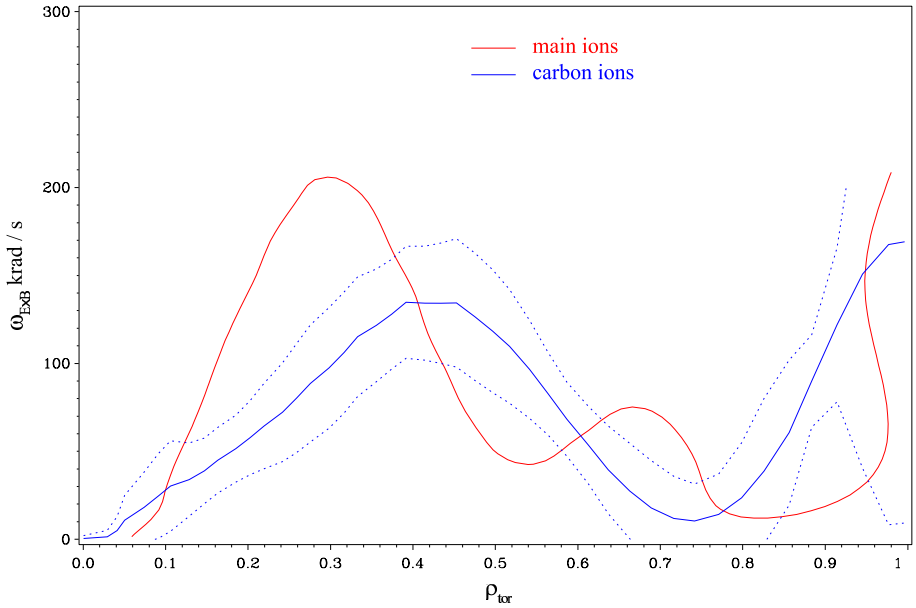

Figure 6.10: Comparison of $\omega_{E\times B}$ calculated from $v_{tor}(ion)$ and $v_{tor}(imp)$ for discharge 12223. The dotted blue lines represent the Monte Carlo error bars on $\omega_{E\times B}$ of the carbon ions.

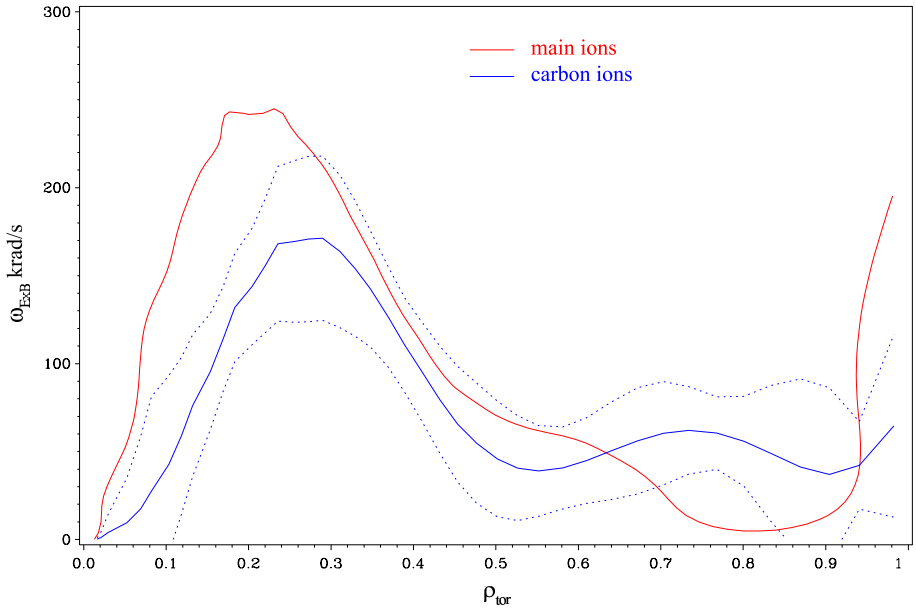

Figure 6.11: Comparison of $\omega_{E\times B}$ calculated from $v_{tor}(ion)$ and $v_{tor}(imp)$ for discharge 13149. The dotted blue lines represent the Monte Carlo error bars on $\omega_{E\times B}$ of the carbon ions.

6.5 Summary and discussions

The results presented in this chapter act as an indication of how well the GLF23 model simulates ITB behavior and what the mechanisms that control this behavior are. The results can not be taken as absolute proof of any particular theory since they are only based on two ITB discharges. However, the fact that both discharges display almost exactly the same dependencies we think makes for a very compelling argument in favor of the findings presented here. Overall, the model predicts the ITBs reasonably well, although the time of formation of the ITB is normally a bit delayed with respect to the experimental one. This could be due to the fact that the inputed experimental profiles are never completely exact, they are always averaged over some time interval and thus, may evolve a little slowly. The delay in ITB formation could also indicate a possible quantitative discrepancy in the model, where the effect of a certain turbulence suppression mechanism is underestimated or a drive for the modes is overestimated. A more detailed study of the model than was undertaken as part of this work would be necessary to clarify this discrepancy.

In general, the results support the main theory of ITB formation due to $E \times B$ shear decorrelation of turbulence. Although, the ITB, either experimental or modelled, is not limited to the region where $\gamma_{max} \approx \gamma_{E\times B}$ and can extend outward even possibly into the region where γ_{max} is much greater than $\gamma_{E\times B}$. This indicates that either the error bars for the criterion for turbulence suppression are underestimated or that complete suppression is not necessary for a weak ITB. The shape of the γ_{max} and $\gamma_{E\times B}$ profiles is interesting. Usually the γ_{max} profile has a maximum a the boundary and a minimum at the center of the plasma. The $\gamma_{E\times B}$ profile is largest at some position in between these points and is very small at the boundary.

The Model predicts a flat ion and electron density profile which is in disagreement with the experimental profiles. A possible explanation of this discrepancy is the role

of the non-thermal ion population. Due to the low density and high temperature of an ITB discharge, the non-thermal ion population reaches densities that are no longer negligible compared with the thermal ion population. It is known that the electron density must equal the total ion density, including both the thermal as well as the non-thermal component, because of quasi-neutrality. Since the non-thermal ion density is strongly peaked a situation in which a peaked electron density profile is observed with the density profile of the main ions actually being flat is possible. An ITB is not predicted when the experimental peaked density profiles are used in the simulations, such that it is expected that the model overestimates the contribution of ∇n_e in the calculations. However, this could also be due to an overestimation of the contribution of ∇n_i in the calculations, although this is the less likely possibility [68].

The model is appears quite insensitive to changes in α. This is in disagreement with the predictions of the GS2 code, presented in chapter 5, and indicates the the α contribution may not be handled properly in the model.

It has been shown that the v_{pol} and v_{dia} contributions are not as small as was previously expected.[18] In fact $E_r(v_{pol})$, $E_r(v_{dia})$ and $E_r(v_{tor})$ have the same order of magnitude. However, since $E_r(v_{dia})$ is in the opposite direction to $E_r(v_{pol})$ their combined contribution is small and hence the correction should be within the assumed error bars of approximately 20%. It can be concluded that it is acceptable to neglect their contribution in the calculations and use only the toroidal velocity contribution. The toroidal velocity of the main deuterium ions has been calculated as a check for the $E \times B$ shearing rate calculations shown in sections 4.2 and 5.4.4. The results indicate that using the real v_{tor}(ion) in the calculations for all the discharges would most likely increase the calculated $\omega_{E\times B}$ hence, a more stable situation would be predicted than that seen in figures 4.5 and 5.16. These results reinforce the hypothesis of $\omega_{E\times B}$ being a major stabilizing mechanism within the plasma with relative importance from the point of view of ITB formation and sustainment.

Chapter 7

Conclusions

The evolution of ITBs on ASDEX Upgrade has been investigated. The results show that narrow ITBs form, before the occurrence of fishbones and the $q = 2$ surface, with their foot inside or very close to the position of q_{min}. 'Staircase' ITBs have been seen on ASDEX-Upgrade and are expected to be connected with MHD activity. Sometimes the positions of these second barriers are seen to follow the $q = 2$ surface, such that they are not inconsistent with a flattening in the ion temperature profile in the vicinity of a rational surface. The position of the ITB seems, to some extent, to be controlled by the q profile i.e. broader barriers have broader positions of q_{min}. Since ITBs normally position themselves at or very close to q_{min} it has been hypothesized that $\hat{s} = 0$ may have a stabilizing effect on turbulence. However, we have seen that very steep gradient ITBs can lie outside the position of q_{min}, in the positive shear region (sometimes outside $\hat{s} = 1$), thus, it is likely that this hypothesis is not valid and that ITBs are not limited by the $\hat{s} = 0$ position.

Other results indicate that negative shear is likely to play a role in barrier formation, but is not important for a fully developed barrier. This is clear because as the ITB develops it moves into the positive shear region. It has also been found that ITBs at ASDEX Upgrade form only at low density, possibly due to a steeper normalized density

gradient. This was further illustrated by ITB discharges in the 2002 campaign where the density was kept low and strong ITBs were reliably produced.

The local theoretical predictions of the mode growth rate were checked for ITB discharges using the gyro-kinetic linear stability, GS2, code. These calculations were done primarily to check the predictions of two different models, the circular $\hat{s} - \alpha$ model and the Miller model which uses real geometry. Firstly, the effects of plasma shaping within the Miller model were studied. It was found that the triangularity, the gradient in the triangularity and the gradient in the elongation has very little effect on the growth rates of the ITG modes. On the other hand, γ_{max} is seen to steadily decrease with increasing elongation. Neglect of the elongation from the calculations could lead to the growth rate of the modes being overestimated by as much as 40% and $R/L_{Ti(crit)}$ being underestimated by as much as 20%.

Increasing α and Δ' in the two models is shown to cause a reduction in the maximum linear growth rate. The decrease in γ_{max} in the $\hat{s} - \alpha$ model is seen to be much greater than for the Miller model. It has also been shown that the simplified relation $\alpha = -4\Delta'$ does not hold for real ASDEX Upgrade equilibrium, at large ϵ.

Studies of the effect of the inverse aspect ratio in the $\hat{s} - \alpha$ and Miller models revealed that the $\hat{s} - \alpha$ model predicts a much smaller influence, of ϵ, on γ_{max} than the Miller model. Both models show an almost linear relationship between ϵ and γ_{max}, with larger values of γ_{max} at larger values of ϵ. However the increase can be almost 70% less in the $\hat{s} - \alpha$ model. These results indicate that the $\hat{s} - \alpha$ model severely underestimates the contribution of the inverse aspect ratio to the growth rate of the modes.

On the other hand, when scans of R/L_{Ti} were done for the real experimental settings of discharge 12223, using the $\hat{s} - \alpha$ and Miller models, it was found that the $\hat{s} - \alpha$

model predicts a much more unstable plasma than the Miller model. This was found to be due to the strong destabilizing effect of the electron temperature and density gradients in the $\hat{s} - \alpha$ model, these effects dominate in driving the modes. The $\hat{s} - \alpha$ model predicts either the density gradient or the electron temperature gradient, or both, to be driving the trapped electron mode (TEM) and, thus, causing the plasma to become more unstable. This is in contrast to the Miller model which predicts a more stable plasma. The $\hat{s} - \alpha$ model uses very a simplified equilibrium where the plasma is described by shifted circular flux surfaces, on the other hand the Miller model takes into account the real geometry of the plasma. Since this implies that Miller model is the more complete and hence the more accurate model, we can conclude that the $\hat{s} - \alpha$ model overestimates the drive of R/L_N and R/L_{Te} for the TEM modes, as compared with the Miller model. Similarly, we can conclude that the Miller model is correct in not predicting the TEM mode to be the dominant instability in these discharges.

Initial results comparing γ_{max}, calculated using the $\hat{s} - \alpha$ model, and the $E \times B$ shear indicated that $E \times B$ shear is not sufficient to explain the suppression of the turbulence in all ITB discharges. However, later studies into the dependencies of the $\hat{s} - \alpha$ model and comparing these with the Miller model, in the GS2 code, showed that the calculation of γ_{max} in the $\hat{s} - \alpha$ model to be too large. The γ_{max} values calculated using the Miller model were found to be much smaller than the values calculated using the $\hat{s} - \alpha$ model and it was found that $\gamma_{max} \approx \gamma_{E \times B}$. It can be concluded that in these ITB discharges the $E \times B$ shear is sufficient to explain the mode suppression and that the earlier results were due to inaccurate dependencies within the $\hat{s} - \alpha$ model. It is also evident from the calculations done with the Miller model that the Shafranov shift and the $E \times B$ shear are equally important from the point of view of turbulence suppression. It can be concluded that the Miller model is a much more accurate model for the calculation of the stability of ITB discharges.

Global plasma simulations using the GLF23 model in the ASTRA code were done and

the results act as an indication of how well the GLF23 model simulates ITB behavior and what the mechanisms that control this behavior are. Overall, the model predicts the ITBs reasonably well, although the time of formation of the ITB is normally a bit delayed with respect to the experimental one. This could be due to the fact that the inputed experimental profiles are never completely exact, they are always averaged over some time interval and thus, may evolve a little slowly. The delay in ITB formation could also indicate a possible quantitative discrepancy in the model, where the effect of a certain turbulence suppression mechanism is underestimated or a drive for the modes is overestimated. Clarification of the cause of this discrepancy was not possible within the time-frame of this work.

In general, the results calculated with the GLF23 model support the main theory of ITB formation due to $E \times B$ shear decorrelation of turbulence. Normally, the ITB, either experimental or modeled, is limited to the region where $\gamma_{max} \approx \gamma_{E\times B}$, however under certain conditions it can extend outward possibly into the region where γ_{max} is much greater than $\gamma_{E\times B}$.

This work also acted as a test for the GLF23 model and two main areas for concern were highlighted, the large drive of the density gradient and the insensitivity to the Shafranov shift. The model predicts a flat electron density profile which is in disagreement with the experimental profile. An ITB is not predicted when the experimental peaked density profiles are used in the simulations, so that it is expected that the GLF23 model overestimates the destabilizing effect of ∇n_e in the calculations (on the TEM mode). In other words, the model seems to predict the TEM mode as the dominant mode and because of this the stabilizing effect of ∇n_e on the ITG mode is offset by the drive of ∇n_e for the TEM mode. The GLF23 model appears quite insensitive to changes in the Shafranov shift. This is in disagreement with the predictions of the GS2 code and indicates the Shafranov shift may not be handled properly in the GLF23 model.

It has been shown that the v_{pol} and v_{dia} contributions are not as small as was previously expected.[18] In fact $E_r(v_{pol})$, $E_r(v_{dia})$ and $E_r(v_{tor})$ have the same order of magnitude. However, since $E_r(v_{dia})$ is in the opposite direction to $E_r(v_{pol})$ their combined contribution is small and hence the correction should be within the assumed error bars of approximately 20%. It can be concluded that it is acceptable to neglect their contribution in the calculations and use only the toroidal velocity contribution.

The toroidal velocity of the main Deuterium ions has been calculated [70] in section 6.4 as a check for the uncorrected $E \times B$ shearing rate calculations shown in sections 4.2 and 5.4.4 which were calculated using the impurity toroidal velocity. The results indicate that using the main ion toroidal velocity in the calculations for all the discharges would most likely increase the calculated $\omega_{E\times B}$ (by approximately 15%). Hence, a more stable situation would be predicted than that seen in figures 4.5 and 5.16.

In conclusion, internal transport barriers in ASDEX Upgrade have been studied in great detail. Their behavior has been mapped and linked to possible turbulence suppression mechanisms. It has been found that low density, negative magnetic shear, $E \times B$ shear and the Shafranov shift are very important for ITB formation. Negative shear and low density are less important for ITB sustainment but $E \times B$ shear and the Shafranov shift are necessary for turbulence suppression and ITB sustainment. It was also found that the $\hat{s} - \alpha$ model overestimates the drive of R/L_N or R/L_{Te}, or both, to the TEM mode, as compared with the Miller model. These results show that the Miller model is a much more accurate model for the calculation of the stability of ITB discharges.

7.1 Outlook

A detailed examination of the ITG mode stability in the $\hat{s} - \alpha$ model has been completed. This examination revealed the inadequacies of the $\hat{s} - \alpha$ model for studying the these ITB plasmas. In light of this a more detailed study into the accuracy of the model should now be undertaken in order to ascertain the cases where the $\hat{s} - \alpha$ model is accurate enough to be used. The results presented in this thesis indicate that it would also be important to investigate fully the effect of the geometry, using the Miller model, on other types of microinstabilities, as these results indicate a that the effect may be quite significant for the stabilization of the trapped electron mode (TEM).

The results of this examination also throw doubt on all other calculations done using the $\hat{s} - \alpha$ model which to the authors knowledge is the most widely used model in this research field. In the authors opinion it would be highly advisable to recheck, using the Miller model, any important results already obtained with the $\hat{s} - \alpha$ model.

Bibliography

[1] Joos F 1996 "The Atmospheric Carbon Dioxide Perturbation" *Europhysics News* **27** 213-218

[2] Ongena J 2000 "Energy for Future Centuries; Will Fusion be an Inexhaustible Safe and Clean Energy Source", *Transactions of Fusion Technology* **37** 3

[3] "World Population Prospects: The 2000 Revision" Population division of the department of economic and social affairs of the United Nations Secretariat, website: http://www.esa.un.org/unpp

[4] "The Green Paper on European Union Energy Policy" 2005, website: http://europa.eu.int/comm/energy-transport/en/lpi_lv_en1.html

[5] Rose D J and Clark M Jr 1961 *Plasmas and Controlled Fusion* Wiley New York

[6] Chen F F 1974 'Introduction to Plasma Physics and Controlled Fusion' Plenum Press New York

[7] Wesson J 1997 'Tokamaks' Clarendon Press Oxford

[8] Hinton F L and Hazeltine R D 1976 *Rev. Mod. Phys.* **48** 239

[9] Wolf R C 2003 *Plasma Phys. Control. Fusion* **45** R1

[10] Connor J W *et al* 2004 *Nucl. Fusion* **44** R1

[11] Burrell K H 1997 *Phys. Plasmas* **4** 1499

[12] Mazzucato E *et al* 1996 *Phys. Rev. Lett.* **77** 3145

[13] Lao L L 1996 *Phys. Plasmas* **3** 1951

[14] Koide Y and the JT-60 Team 1997 *Phys. Plasmas* **4** 1623

[15] Greenfield C M *et al* 1997 *Phys. Plasmas* **4** 1596

[16] Synakowski E J *et al* 1997 *Phys. Plasmas* **4** 1736

[17] Synakowski E J *et al* 1985 *Nucl. Fusion* **25** 1167

[18] Meister H *et al* 2001 *Nucl. Fusion* **41** 1633

[19] Peeters A G, private communications

[20] Beer M A 'Gyrofluid models of turbulent transport in tokamaks' PhD thesis (1995)

[21] Jenko F *et al* 2000 *Phys. Plasmas* **7** 1904

[22] Beer M A *et al* 1997 *Phys. Plasmas* **4** 1792

[23] Biglari H, Diamond P H , and Terry P W 1990 *Phys. Fluids* B**2** 1

[24] Waltz R E, Kerbel G D and Milovich J 1994 *Phys. Plasmas* **1** 2229

[25] Hahm T S and Burrell K H 1995 *Phys. Plasmas* **2** 1648

[26] Waltz R E, Kerbel G D, Milovich J and Hammett G W 1995 *Phys. Plasmas* **2** 2408

[27] P.J. Mc Carthy, Ph.D. thesis, University College Cork, 1992.

[28] Shafranov V D 1966 'Plasma Equilibrium in a Magnetic Field' *Reviews of Plasma Physics*, Vol. 2 (M.A. Leontovich, Ed.), Consultants Bureau, New York (Translation of "Voprosy Teorii Plazmy", Atomizdat, Moscow, 1963).

[29] Bateman: 1978 'MHD Instabilities', The MIT Press, Cambridge (Mass.)

[30] Freidberg J P 1982 'Ideal Magnetohydrodynamic Theory of Magnetic Fusion Systems' *Rev. Mod. Phys.* **54** 801–902

[31] McCarthy P J 1999 *Phys. Plasmas* **6** 3554

[32] Shafranov V D 1958 Sov. Phys. JETP **6**, 545; 1957 Zh. Eksp. Teor. Fiz. **33**, 710.

[33] Grad H and Rubin H *Proceedings of the Second United Nations Conference on the Peaceful uses of Atomic Energy* (United Nations, Geneva, 1958), Vol. 21, p. 190.

[34] Foley M 2004 Ph.D. thesis, University College Cork

[35] Quigley E D *et al* 2004 *Nucl. Fusion* **44** 1189

[36] Joffrin E *et al* 2002 *Plasma Phys. Control. Fusion* **44** 1739

[37] Sakamoto Y *et al* 2001 *Nucl. Fusion* **41** 865

[38] Burrell K H *et al* 1998 *Plasma Phys. Control. Fusion* **40** 1585

[39] Doyle E J *et al* 2002 *Nucl. Fusion* **42** 333

[40] Greenfield C M *et al* 1999 *Nucl. Fusion* **39** 1723

[41] Koide Y *et al* 1994 *Phys. Rev. Lett.* **72** 3662

[42] Razumova K A *et al* 2003 *Plasma Phys. Control. Fusion* **45** 1247

[43] Gorini G *et al* 2000 *Plasma Phys. Control. Fusion* **42** A161

[44] Koide Y *et al* 1998 *Plasma Phys. Control. Fusion* **40** 97

[45] Rettig C L 1998 *Phys. Plasmas* **5** 5

[46] Baranov Yu F *et al* 1999 *Nucl. Fusion* **39** 1463

[47] Koide Y *et al* 1996 *Plasma Phys. Control. Fusion* **38** 1011

[48] Sips A C *et al* 2002 *Plasma Phys. Control. Fusion* **44** A391

[49] Gohil P *et al* 2003 *Nucl. Fusion* **43** 708

[50] Garbet X 2001 *Plasma Phys. Control. Fusion* **43** A251

[51] Connor J W and Wilson H R 1994 *Plasma Phys. Control. Fusion* **36** 719

[52] Yoshizawa A *et al* 2001 *Plasma Phys. Control. Fusion* **43** R1

[53] Ernst D R *et al* 2004 *Phys. Plasmas* **11** 2637

[54] Angioni C *et al* 2004 *Nucl. Fusion* **44** 827

[55] Burrell K H 1999 *Phys. Plasmas* **6** 4418

[56] Kotschenreuther M, Rewoldt G and Tang W M 1995 *Comp. Phys. Comm.* **88** 128

[57] Dorland W *et al* 2000 *Presented at the 18th lnt. Conf. on Fusion Energy 2000 (Proc. 18th Int. Conf. Sorrento,2000) (Vienna: IAEA) CD-ROM file TH2/5, http://www.iaea.org/programmes/ripc/physics/fec2000/html/node1.htm*

[58] Freidberg J P 1987 'Ideal Magnetohydrodynamics' Plenum Press New York and London

[59] Miller R L *et al* 1998 *Phys. Plasmas* **5** 973

[60] Coppi B, Ferreira A, Mark J W-K and Ramos J J, 1979 *Nucl. Fusion* **19** 715

[61] Connor J W, Hastie R J and Taylor J B, 1978 *Phys. Rev. Lett.* **40** 396

[62] Nilsson J and Weiland J, 1995 *Nucl. Fusion* **35** 497

[63] Pereverzev G and Yushmanov P, Max-Planck-Institut für Plasmaphysik Report, IPP 5/98 (Garching, Germany 2002)

[64] Waltz R E *et al* 1997 *Phys. Plasmas* **4** 2482

[65] Waltz R E *et al* 1992 *Phys. Fluids B* 1992 **4** 3138

[66] Polevoi A, Shirai H and Takizuka T, 1997 JAERI-Data/Code 97-014

[67] Tardini G *et al* 2004 *31st EPS Conf. Plasma Phys.* London **28G** 4.123

[68] Peeters A G, private communications

[69] Nishijima D *et al* 2005 *Plasma Phys. Control. Fusion* **47** 89

[70] Kim Y B, Diamond P H and Groebner R I 1991 *Phys. Fluids B* **3** 1991

[71] Testa D *et al* 2002 *Phys. Plasmas* **9** 243